High Resolution Vibrational Spectroscopy of Functional Organic Molecules at Surfaces

Im Fachbereich Physik
der
Freien Universität Berlin
eingereichte Dissertation
von

Stephan Stremlau

Berlin, Januar 2015

This thesis has been conducted in the group of Prof. Dr. Petra Tegeder between Oktober 2010 and June 2013 at the Department of Physics of the Freie Universität Berlin and between July 2013 and January 2015 at the Institute of Physical Chemistry of the Ruprecht-Karls-Universität Heidelberg.

Erstgutachter: Prof. Dr. Petra Tegeder
Zweitgutachter: Prof. Dr. Katharina J. Franke
Datum der Disputation: 6. Juli 2015

Eidesstattliche Versicherung

Hiermit versichere ich, daß ich alle verwendeten Hilfsmittel und Hilfen angegeben und die vorliegende Arbeit auf dieser Grundlage selbstständig verfasst habe. Diese Arbeit wurde nicht schon einmal in einem früheren Promotionsverfahren eingereicht.

Berlin, Januar 2015
Stephan Stremlau

Contents

Eidesstattliche Versicherung iii

List of Abbreviations xiv

Abstract 1

Deutsche Zusammenfassung 2

1 Introduction 5

2 Experimental details 9
- 2.1 High Resolution Electron Energy LossSpectroscopy 9
  - 2.1.1 Different Scattering Regimes 11
  - 2.1.2 Ultra-High-Vacuum Chamber 15
  - 2.1.3 Au(111), Bi(111) and Bi(114) Substrates 16
  - 2.1.4 Sample preparations 17
  - 2.1.5 Temperature Programmed Desorption Spectroscopy 18
  - 2.1.6 Density functional theory 19

3 Graphene nanoribbons on Au(111) 21
- 3.1 Graphene nanoribbon fabrication 23
  - 3.1.1 Pristine Graphene nanoribbon 25
  - 3.1.2 Singly Nitrogen Doped Graphene Nanoribbon 30
  - 3.1.3 Doubly Nitrogen Doped Graphene Nanoribbon 34
- 3.2 Electronic Properties 37
  - 3.2.1 Pristine Graphene nanoribbon 37
  - 3.2.2 Singly Nitrogen Doped Graphene Nanoribbon 41
  - 3.2.3 Doubly Nitrogen Doped Graphene Nanoribbon 43
- 3.3 Conclusions 44

4 Tetraazaperopyrene and its derivatives on Au(111) 47
4.1 Adsorption Geometry 49
4.1.1 TAPP 49
4.1.2 TAPP-(C_3F_7)$_2$ 54
4.1.3 TAPP-Cl_4-(C_3F_7)$_2$ 59
4.2 Electronic properties 63
4.2.1 TAPP 63
4.2.2 TAPP-(C_3F_7)$_2$ 67
4.2.3 TAPP-Cl_4-(C_3F_7)$_2$ 69
4.3 Conclusions 71
4.3.1 TAPP 71
4.3.2 TAPP-(C_3F_7)$_2$ 72
4.3.3 TAPP-Cl_4-(C_3F_7)$_2$ 74

5 Octithiophene on Au(111) 75
5.1 Adsorption Geometry 77
5.2 Conclusions 81

6 3,4,9,10-Perylene-tetracarboxylic-dianhydride on Au(111) 83
6.1 Adsorption Geometry 86
6.2 Binding Energy 89
6.3 Electronic Properties 93
6.4 Conclusions 96

7 Di-Meta-Cyano-Azobenzene on Bi(111) 97
7.1 Adsorption Geometry 99
7.2 Electronic Properties 103
7.3 Conclusions 106

8 Nitro-Spiropyran on Bi(114) 107
8.1 Adsorption Geometry of Nitro-Spiropyran on Bi(114) 111
8.2 Ring-Opening isomerization reactions 116
8.2.1 Vibrational changes upon isomerization 116
8.2.2 Thermally and Light induced isomerization 117
8.3 Conclusions 120

9 Summary 121

A GNR 125

B TAPP **127**

C DMC Bi(111) **129**

D Nitro-Spiro on Bi(114) **131**

List of Publications **159**

Acknowledgement **161**

Curriculum vitae **163**

List of Figures

2.1 HREELS spectrometer 10
2.2 Scattering geometries in HREELS 12
2.3 Surface selection rules in HREELS 13
2.4 Cross section for dipole scattered electrons 14
2.5 UHV Setup 15
2.6 TPD order 19

3.1 Schematic of GNR formation steps 23
3.2 STM images of GNR on Au(111) 24
3.3 pristine GNR precursor molecule 25
3.4 Multi-mass TPD spectra during 2N-GNR formation 26
3.5 Vibrational HREEL spectra of GNR formation 27
3.6 1N-GNR precursor molecule 30
3.7 Vibrational HREEL spectra of 1N-GNR formation 31
3.8 2N GNR precursor molecule 34
3.9 Vibrational HREEL spectra of 2N-GNR phase 35
3.10 Electronic HREEL spectrum and UVvis spectrum of GNR monomer . . 37
3.11 Electronic HREEL spectra of GNR formation 39
3.12 Electronic HREEL spectra of 1N-GNR formation 42
3.13 Electronic HREEL spectra of 2N-GNR phase 43
3.14 Result of UPS and electronic HREEL spectra of GNR 45
3.15 Electronic HREEL spectra of GNR, 1N-GNR and 2N-GNR nanoribbons 46

4.1 TAPP precursor molecule 49
4.2 TPD spectra for diff. TAPP coverages 49
4.3 TAPP polymerization via activated carbene species 50
4.4 HREEL spectra of 1ML TAPP 52
4.5 Structure of TAPP(C_3F_7)$_2$ 54
4.6 TPD spectra for diff. TAPP-(C_3F_7)$_2$ coverages 55

4.7 HREEL spectra of 1 ML TAPP(C_3F_7)$_2$ 56
4.8 Structure of TAPP-Cl$_4$-(C_3F_7)$_2$ 59
4.9 TPD spectra for diff. TAPP-Cl$_4$-(C_3F_7)$_2$ coverages 59
4.10 HREEL spectra of 1 ML TAPP-Cl$_4$(C_3F_7)$_2$ 60
4.11 Electronic HREEL spectra of 1ML TAPP 64
4.12 HREEL spectra of 1 ML TAPP(C_3F_7)$_2$ 67
4.13 Electronic HREEL spectra of 1ML TAPP-Cl$_4$(C_3F_7)$_2$ 69
4.14 Crystal structure of single TAPP-R$_4$-(C_3F_7)$_2$. 72
4.15 Crystal structure of bulk TAPP-R$_4$-(C_3F_7)$_2$. 73

5.1 Structure of 8T molecule 75
5.2 STM images of 8T on Au(111) as indicated 77
5.3 Vibrational HREEL spectra of a sub-ML α-8-T 78
5.4 Scheme of orientation of diff. α-8-T coverages 79
5.5 Comparison of HREEL spectra of sub-ML and 1ML α-8-T 81

6.1 Structure of PTCDA molecule 83
6.2 Vibr. HREEL spectra for 1,2 and 6ML coverage 87
6.3 TPD data as a function of coverage 89
6.4 PTCDA coverage (normalized) vs. temperature 90
6.5 Binding Energy of PTCDA vs. coverage 91
6.6 Electronic HREEL spectra for 1 and 6ML PTCDA 93
6.7 Close up of electronic HREEL spectra for 6ML coverage 94

7.1 Inversion and Rotation mechanism of azobenzene 97
7.2 TPD spectrum of 3 ML DMC 99
7.3 Vibrational HREEL spectra of 1 and 4 ML DMC 101
7.4 Electronic HREEL spectra of 1 and 4 ML DMC 103

8.1 Structure of nitrospiropyran and the merocyanine form 107
8.2 STM images of nitro-Spiropyran on Bi(110) 108
8.3 STM images of Bi(114) 109
8.4 TPD spectra of Nitro-spiropyran on Bi(114) 111
8.5 HREEL spectra of sub- and 3 Ml of SP 112
8.6 HREEL spectra of 3 Ml of MC 116
8.7 HREEL spectra SP to MC via heating 118

A.1 Ortep plot of the 2N-GNR precursor crystal structure 125
A.2 Electronic HREEL spectra of GNR formation on Au(111) 126

B.1 HREEL spectra after TPD to T=800K (TAPP) 127
B.2 HREEL spectra after TPD to T=900K (TAPP-(C_3F_7)$_2$) 128
B.3 HREEL spectra after TPD to T=900K (TAPP-Cl_4(C_3F_7)$_2$) 128

C.1 HREEL spectra of clean Bi(111) with $E_0 = 3.5eV$ 129
C.2 HREEL spectra of clean Bi(111) with $E_0 = 15.5eV$ 130

D.1 HREEL spectrum after TPD up to 420 K 131

List of Tables

2.1 Different preparation conditions 17

3.1 Assign. of vibr. modes of GNR formation 29
3.2 Assign. of vibr. modes of 1N-GNR formation 32
3.3 Assign. of vibr. modes of 2N-GNR phase 35
3.4 Electronic transitions of GNR formation 38
3.5 Electronic transitions of 1N-GNR formation 41

4.1 Assign. of vibr. modes of TAPP on Au(111) 51
4.2 Assign. of vibr. modes of TAPP-$(C_3F_7)_2$ on Au(111) 57
4.3 Assign. of vibr. modes of TAPP-$Cl_4(C_3F_7)_2$ on Au(111) 62
4.4 Electronic transitions of TAPP on Au(111) 65
4.5 Electronic transitions of TAPP$(C_3F_7)_2$ on Au(111) 68
4.6 Electronic transitions of TAPP-$Cl_4(C_3F_7)_2$ on Au(111) 70

5.1 Assign. of vibr. modes of α-8T on Au(111) 79

6.1 Assignment of vibr. modes of diff. PTCDA coverages, IR and calc. Data 86
6.2 Electronic transitions for 1 and 6 ML PTCDA 94

7.1 Assign. of vibr. modes of DMC on Bi(111) 100
7.2 Electronic transitions of DMC on Bi(111) 104

8.1 Assign. of vibr. modes of Nitro-Spiropyran on i(114) 113

List of Abbreviations

α-8T	α-Octithiophene
B3LYP	Becke 3-Parameter (Exchange), Lee, Yang and Parr (correlation)
cm^{-1}	Wavenumber
DFT	Density Functional Theory
DMC	Di Meta Cyano Azobenzene
DOS	Density of States
(E_F)	Fermi Level
FET	Field Effect Transistor
FWHM	Full Width at Half Maxmimum (measured at the elatic peak)
GNR	Graphene Nanoribbon
GNR	6,11-dibromo-1,2,3,4-tetraphenyl-triphenylene
1N-GNR	4-(6,11-Dibromo-1,3,4-triphenyltriphenylen-2-yl)pyridine
2N-GNR	4,4-(6,11-Dibromo-1,4-diphenyltriphenylene-2,3-diyl)dipyridine
GXID	Grazing Incidence X-Ray Diffraction
HOMO	Highest Occupied Molecular Orbital
HREELS	High Resolution Energy Loss Spectroscopy
IGP	Ion Getter Pump
LUMO	Lowest unoccupied Molecular Orbital
MC	Merocyanine
ML	Monolayer
NEXAFS	Near Edge X-Ray Absorption Fine Structure
NIXSW	Normal Incident X-Ray Standing Wave
OFETs	Organic Field Effect Transistors
OLEDs	Organic Light-Emitting Diodes
OPVC	Organic Photovoltaic Cells

PAH	polycyclic aromatic hydrocarbon
PTCDA	3,4,9,10-Perylene-tetracarboxylic-dianhydride
QMS	Quadrupol Mass Spectrometer
RHEED	Reflection High-Energy Electron Diffraction
SP	Spiropyran
SPA LEED	Spot Profile Analysis-Low-Energy Electron Diffraction
STM	Scanning Tunneling Microscopy
TAPP	1,3,8,10-tetraazaperopyren
TAPP-$(C_3F_7)_2$	2,9-bisperfluoropropyl-1,3,8,10-tetraazaperopyren
TAPP-Cl_4-$(C_3F_7)_2$	2,9-bisperfluoropropyl-4,7,11,14-tetrachloro-1,3,8,10-tetraazaperopyren
TDS	Thermal Desorption Spectroscopy
THF	Tetrahydrofuran
TFT	Thin Film Transistor
UHV	Ultra High Vacuum
UPS	Ultraviolet Photoemission Spectroscopy
X-rays	Röntgen radiation

Abstract

In this thesis, vibrational and electronic high resolution electron energy loss spectroscopy (HREELS) in addition with temperature programmed desorption spectroscopy (TPD) were employed in order to investigate the adsorption and electronic properties of different functional organic molecules on metal and semi-metal surfaces. The goal of this work is to extend the knowledge of the important initial adsorption criteria of those molecules since they define the properties for further applications. Graphene, lacking the desired band gap, can be converted by lateral constriction into a charge carrier, quasi-one-dimensional, nanometer width, graphene nanoribbon (GNR). Using a bottom up technique, employing a thermally activated reaction on the substrate, these GNR can be precisely generated from halogen activated precursor monomers. Upon GNR formation a polymer phase and finally the planar, aromatic GNR is obtained accompanied by drastic changes in the vibrational and electronic HREEL spectra. HREELS is the ideal tool to follow such reactions and is capable to directly measure the band gap of the GNR. Furthermore we investigated the influence of N-doping incipient with the precursors and found that the band gap aligns with respect to the Fermi level of the gold substrate leaving the width of the band gap untouched. Tetraazaperopyrene show promising properties for organic electronics. We investigated 3 derivatives adsorbed on Au(111) and gained insights in their adsorption geometries and found evidence for the formation of gold-adatom molecule complex formation. The α-Octithiophene (8T) molecule, a promising candidate for organic electronics was adsorbed on Au(111) to elucidate its behavior upon increasing coverage within a monolayer. We demonstrated that the 8T molecules undergo a structural reorientation from a planar to a tilted geometry upon increasing molecular density on the surface which is in contrast to other thiophene derivatives, e.g. different number of thiophene rings. Binding energy determination can be challenging or even unfeasible. For 3,4,9,10-Perylene-tetracarboxylic-dianhydride (PTCDA) adsorbed on Au(111) we successfully determined the binding energy via a TPD approach employing the complete analysis method and endorse the physisorptive nature of the adsorbate substrate bond. Molecular switches based on azobenzene undergoing a trans to cis isomerization is of great interest. Azobenzenes reversible trans to cis isomerization can be induced in solution via illumination with ultraviolet (UV) light and by applying heat or visible light. This reaction is most often quenched on metal substrates. The isomerization of the derivative di-meta-cyano-azobenzene remains feasible on the Bi(111) surface. We investigated the adsorption propterties for different coverages and shine light on the electronic structure beyond the limit of ultravioletvisible spectroscopy (UV/vis). Furthermore we investigated the molecular switch nitro-spiropyran on the Bi(114) surface. While the ring-opening reaction is quenched in the sub-monolayer regime, which we attribute to the particular surface topology, we successfully demonstrate the switching in the multilayer regime either thermally induced or triggered via illumination with UV light.

Deutsche Zusammenfassung

In dieser Arbeit wurde die Hochauflösende Elektronen Energieverlust Spektroskopie (HREELS) zusammen mit der Temperatur programmierten Desorptionsspektroskopie (TPD) eingesetzt, um die Adsorptions- und Elektronischen Eigenschaften von verschiedenen, funktionellen organischen Molekülen auf Metall- und Halbmetalloberflächen zu untersuchen. Das Ziel dieser Arbeit ist es, das Wissen über die wichtigen, ersten Adsorptionskriterien der Moleküle zu erweitern, da sie die Eigenschaften für weitere Anwendungen vorgeben können. Graphen, welches keine Bandlücke aufweist, kann durch laterale Begrenzung in einen Ladungsträger umgewandelt werden, und man erhält ein wenige Nanometer breites Graphennanoband (GNR). Mit Hilfe der Bottom-up-Technik, unter Verwendung einer thermisch aktivierten Reaktion auf dem Substrat, können diese GNR aus Halogen-aktivierten Vorstufenmolekülen erzeugt werden. Die Bildung eines GNR wird begleitet von drastischen Veränderungen in den Schwingungs- und Elektronischen HREEL-Spektren. HREELS ist das ideale Werkzeug, um diese Änderungen zu verfolgen, weiterhin kann direkt die Bandlücke gemessen werden. Wir untersuchten zudem den Einfluss von N-Dotierung und fanden heraus, dass sich die Bandlücke in Bezug auf das Fermi-Niveau des Goldsubstrates ausrichtet ohne jedoch die Bandlücke zu verändern. Tetraazaperopyrene zeigen vielversprechende Eigenschaften für Organo-Elektronik-Anwendungen. Wir untersuchten drei Derivate adsorbiert auf Au(111) und fanden Hinweise auf eine Gold-Adatom Molekül Komplexbildung. Das α-Octithiophene (8T) Molekül, ein vielversprechender Kandidat für Organo-Elektronik wurde auf Au(111) adsorbiert. Rastertunnelmikroskopische Untersuchungen legten nahe, dass die 8T-Moleküle eine strukturelle Umorientierung von einer planaren zu einer geneigten Geometrie bei zunehmender Moleküldichte auf der Oberfläche zeigen, im Gegensatz zu anderen Thiophen-Derivaten. Wir konnten diese strukturelle Veränderung mittels HREELS verfolgen und belegen. Die Bindungsenergiebestimmung kann eine Herausforderung oder sogar unmöglich sein. Für 3,4,9,10-Perylentetracarbonsäuredianhydrid (PTCDA) adsorbiert auf Au(111) haben wir erfolgreich die Bindungsenergie bestimmt und die physisorptive Art der Adsorbat/Substrat-Bindung nachgewiesen. Molekulare Schalter basierend auf Azobenzol (trans-cis-Isomerisierung) sind von großem Interesse und wurden vielfältig untersucht. Die reversible trans-cis-Isomerisierung kann in Lösung durch Beleuchtung mit ultraviolettem Licht (UV) oder durch Wärmezufuhr, beziehungsweise sichtbarem Licht, induziert werden. Diese Reaktion wird meist auf Metallsubstraten unterdrückt. Das Derivat Di-Meta-Cyano-Azobenzol auf Bi(111) behält seine Isomerisierbarkeit. Wir untersuchten die Adsorptionseigenschaften für verschiedene Bedeckungen und zeigen die elektronische Struktur jenseits der Grenze der UV-VIS-Spektroskopie (UV/vis). Weiterhin untersuchten wir den molekularen Schalter Nitro-Spiropyran auf der Bi(114) Oberfläche. Während die Ringöffnungsreaktion bei niedrigen Bedeckungen unterdrückt wird (dieses Verhalten führen wir auf die besondere Oberflächentopologie zurück) konnten wir für höhere Bedeckungen die entweder thermisch Induzierte oder durch Bestrahlung mit UV-Licht ausgelöste Ringöffnungsreaktion demonstrieren.

Chapter 1

Introduction

When thinking of technical applications of functional, organic molecules in electronic devices one has to consider many parameters of which the interaction with the underlying substrate (electrodes providing electric contact; photovoltaic cell junctions) plays the crucial role [1–21]. In the past decades invention and development of electronic devices gained more and more attention. Increasing computing power and improved mobility grew a strong demand for the ability to down scale integrated circuits and related components [22, 23]. When the atomic scale is reached, the need for new materials and methods is the key since with common techniques and materials a certain threshold of minimization could not be overcome. In the context of organic electronics which are already in daily use like in photovoltaic cells, light-emitting diodes, thin-film transistors the normally employed π-conjugated aromatic carbon based semiconducting molecules and their interaction with metal substrates play the crucial role. These semiconductors can be divided into n-and p-type called semiconductors. Whereas n-type (from the negative charge of the excess electron) denotes semiconductors that possess a larger electron concentration than hole concentration and that electrons are the majority carriers. The p-type (from positive charge of the hole) semiconductors have a larger hole concentration than electron concentration thus making the holes the majority carriers [16, 24–28]. The tuning of the properties of the employed molecules to meet the desired specifications like good air stability, charge-carrier capabilities and electron injection capability remains a challenge.

Furthermore, molecular switches are of great interest for applications concerning data storage and other molecular driven devices like sensor systems [29, 30]. Most of the molecular switches are investigated in solution where the molecular reorientations are not quenched by the environment. Switching means a controllable, change within the molecule including trans/cis isomerizations or ring-opening ring-closing reactions that are induced via an external stimuli like photons or applying heat to the sample [31]. The switching reaction is usually accompanied by immense structural changes of the molecule altering its vibrational and electronic properties. The ability for switching in solutions is not necessary indicative for the behavior of the adsorbed molecule on a metal substrate. It is most often found that the isomerization is suppressed when the molecular switch is in contact to a metal substrate [32–42]. This finding is attributed to the fact that numerous decay channels for the excited states are present and of course due to steric hinderance. These problems are addresses in many studies and solutions to overcome them are found in a less strong coupling substrate, steric demanding side groups leading to a decoupling or via inserting substituents altering the electronic structure of the molecule and thus lowering the isomerisation barrier [41, 43–47].

Within this thesis we employed vibrational and electronic high resolution electron energy loss spectroscopy and temperature programmed desorption spectroscopy in order to shine light on the adsorption and electronic properties of different functional organic molecules for varying coverages on the Au(111), Bi(111) and Bi(114) substrate. The initial adsorption orientation of molecules with respect to the underlying substrate is of great importance since their electronic properties strongly depend on the molecular substrate interaction. Geometrical changes of the molecules upon increasing coverage or during isomerization reactions lead to pronounced changes in the vibrational and electronic fingerprints of the corresponding molecule. HREELS has proven to be the ideal tool to investigate such vibrational changes and is furthermore capable to directly measure the optical gap and further electronic transition beyond the limits of UV/vis spectroscopy.

In Chapter 3 we investigated the bottom-up fabrication process of different GNRs by means of HREELS and TPD an a Au(111) surface. The precursor molecules, a halogen-activated triphenylene derivative yields a precise nanometer wide graphene nanoribbon during a surface catalyzed synthesis induced by heating of the sample. Prior to the planar, aromatic GNR obtained via cyclodehydrogenation a polymer phase is observed in HREELS. Accompanied by vast structural changes upon GNR formation thus leading to characteristic fingerprints in the vibrational spectra the electronic structure is altered as well. Furthermore to the pristine GNR we investigated the influence of N-doping on the GNR formation process and the electronic structure. We find that the bottom up approach is valid for N-doped derivatives as well. The band gap remains untouched while the electronic structures aligns with the underlying substrate with respect to its Fermi level. The novel group of Tetraazaperopyrenes as promising candidates for organic electronics is presented in 4. We investigated the pristine Tetraazaperopyren among with 2 differently substituted derivatives. We find that the molecules adsorb planar with respect to the surface. A slight tilting along the short axis upon increasing coverage is observed for the fluoroalkyl substituted derivatives and the trans orientation of the mentoined side chains is the favoured motif which is attributed to steric hinderance. The electronic HREEL spectra reveal the formation of gold adatom complexes on the surface which is consistent to findings on a Cu(111) surface.

Another interesting candidate for applications in organic electronics, Octithiophene, is discussed in chapter 5. A geometrical change upon increasing coverage was suggested by STM studies but no conclusive statement was possible. In this work we studied the adsorption geometry as a function of coverage of Octithiophen on a Au(111) substrate. A planar adsorption geometry with respect to the surface was observed for a sub-monolayer (ML) coverage. Upon increasing coverage a geometrical change can be observed and we conclude that the α-Octithiophene molecules adapt a tilted orientation along its long molecular axis with respect to the surface when the monolayer regime is reached. Stabilization of the 2 phases can be explained either by the molecule/substrate interaction (sub-ML regime), the molecular π-system overlaps with the density of states (dos) of the metal or by intermolecular interaction, establishing a π-π stacking between the octithiophenes leading to another energetically favoured structural motif on the surface.

The binding energy of molecules on surfaces is a good probe for the interaction strength of a system. One suitable way to gain such information is the evaluation of TPD data, certain criteria have to be fulfilled for this to be feasible. Most important, the molecules under investigation have to desorb intact from the surface. In chapter 6 we successfully determine the binding energy of PTCDA on the gold substrate in the limit of a single molecule by means of a complete analysis approach for TPD data evaluation which can be used as a benchmark for theoretical calculations. And we receive a binding energy of 1.93($\pm$0.04) eV. Moreover we found a planer adsorption geometry that persists for higher coverages and the electronic HREEL spectra reveal a HOMO LUMO transition with vibrational progression among further high loss energy electronic transitions.

Besides the already presented systems we studies two types of molecular switches. Chapter 7 investigates the adsorption and electronic properties of the azobenzene derivative di-meta-Cyano azobenzene (DMC) adsorbed on a Bi(111) substrate. A photoinduced trans to cis isomerization is reported in literature for different coverages. We were interested in the initial adsorption geometry and growth beyond the first monolayer and to gain more insights in the electronic structure of the molecule. The structural orientation of the molecules with respect to the substrate can play a key role for further studies and profound knowledge is needed. A planar adsorption in the trans configuration was observed even for coverages up to 4 ML. The second molecular switch, namely Nitro-Spiropyran, is presented in chapter 8. Here a Bi(114) surface, showing metallic character on a semimetallic bulk, was chosen. The conversion from the 3-dimensional, ring-closed Spiropyran (SP) form to the planar, zwitterionic Merocyanine (MC) form is achieved via the cleavage of the central OCN bond which as well functioned as a marker in our conducted vibrational spectra. The ring-closed form is the energetically more stable conformation on the substrate in a sub-ML coverage and no isomerization reaction could be induced. We were able to successfully demonstrate a thermally induced ring-opening reaction in a multilayer regime and upon illumination with UV laser light we observed a photostationary state. The ring-opened, merocyanine form was found to be the more stable one which is attributed to the formation of dimers among the zwitterionic molecules. Our obtained results clearly depict that the adsorbate/substrate interaction represents a fine balance that needed to be found in order to prevail functionalization for adsorbed molecular switches.

Chapter 2

Experimental details

The details of the experimental setup and the to the measurements related phenomena are described in detail elsewhere [48]. In the following sections a brief description of the experimental setup and its underlying mechanisms will be given.

2.1 High Resolution Electron Energy Loss Spectroscopy

Among other vibrational spectroscopy methods the High Resolution Electron Energy Loss Spectroscopy (HREELS) is a powerful tool to gain insights into absorption properties and to investigate geometries of adsorbates on surfaces. Furthermore it gives access to directly measure electronic transitions in monolayers and multilayers of organic molecules on a wide variety of different substrates. In contrast to other vibrational techniques like infrared reflection absorption spectroscopy (IRAS) or helium atom scattering (HAS), HREELS employs a monochromatic electron beam for excitation which is scattered at a surface and then detected. By using electrons this technique shows great advantages which is the achievable high sensitivity (due to the low penetration depth of slow electrons), the accessibility of very low frequency vibrational modes and excitation of electronic transitions. Employing HREELS, Ibach proofed that the low coverage limit for detection lies at astonishing 1/100 of a monolayer of CO adsorbed on a Pt(111) surface [49]. In order to obtain more informations on the type and strength of the interactions of molecules adsorbed on a surface we compare the received spectra with published vibrational data obtained from the gas phase or from condensed phase. Among all the positive aspects concerning HREELS one disadvantages has to mentioned and that is the achievable resolution. The typically resolutions are in the order of above 16 cm^{-1} for molecule covered surfaces. In contrast IRAS and atom scattering techniques easily reach resolutions below 0.8 cm^{-1} [50]. Figure 2.1 a) shows an actual image of the used Delta 0.5 instrument provided by SPECS and 2.1 b) a schematic sketch of the spectrometer. The spectrometer consists of a fixed, double stage monochromator and a rotatable, single stage analyzer part. The two parts are joined via the central scattering chamber in which the sample is lowered down during measurements. The spectrometer is capable of generating primary electron energies of up to 250 eV and the scan range reaches 50 eV loss energy. The primary electrons are generated in a LaB_6 cathode and then were focused by a set of lenses into the monochromator section (pre- and monochromator are both in a 127 ° cylindrical sector analyzer design). The now monochramatic electron beam is then focused onto the sample in the scattering chamber and the reflected electrons reach the entry slit of the analyzer part (127 ° cylindrical sector analyzer) and finally hit the electron multiplier which is in our case a channeltron and leads to an observable signal. The channeltron is operated at 2.3 keV which is in the plateau region for the specific type (no signal increase with increasing high voltage). The whole analyzer part, containing the channeltron as well, is rotatable around the scattering chamber and thus allows for angular dependent measurements. For the investigations of the adsorbate vibrations, primary electron energies of 3.5 eV to 5 eV were chosen and we analyzed the energy losses up to 3500 cm^{-1}. For the electronic transitions an energy of 15.5 eV was employed, which is sufficiently high enough to excite electronic transitions within the molecules, and the measured energy loss range was increased up to 8 eV. The achievable resolution for our vibrational studies was in the range of about 2 meV (16 cm^{-1}) and up to 4 meV (32 cm^{-1}), respectively. The resolution is measured as the full width at half maximum (FWHM) in the direct beam (elastically scattered electrons). For a more detailed description to this well-known spectroscopic technique we encourage the reader of this thesis to also look up the articles of Thiry and

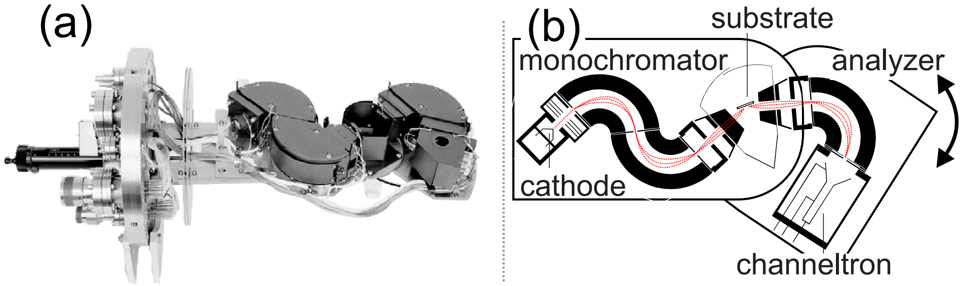

Figure 2.1: HREEL spectrometer, a) actual image of the used Delta o.5 spectrometer taken from [51], b) sketch of the spectrometer parts as indicated.

Rocca [52, 53] and of course the book with the title "Electron energy loss spectroscopy and surface vibrations" by Ibach and Mils published in 1982 [49].

2.1.1 Different Scattering Regimes

In HREEL spectroscopy three types of inelastic interactions of the incoming electrons with the adsorbed molecules have to be taken into consideration [49, 52]. First the long ranging, dipolar scattering regime (Coulomb interaction) in which the inelastic scattered electrons in are concentrated in a narrow angle close to the specular measurement geometry. Dipolar scattering , found in HREEL spectra of adsorbates in specular geometry, follow IR-metal surface selection rules. Second comes the short range impact scattering. The inelastically scattered electrons are distributed over a broad scattering angle. The surface selection rule does not apply for the impact scattering regime referred to off-specular measuring geometry. And last the negative ion resonances (NIR) mechanism which is strongly dependent of the primary electron energy. When the primary, incident electron e_i^- having an initial energy of E_i interacts with a molecule covered surface (see Figure 2.2) a vibrational quantum $\hbar\omega$ resulting in the energy of the inelastic scattered electron E_s can be excited.

$$E_s = E_i\hbar\omega \tag{2.1}$$

Measuring the energy loss of the scattered electrons in the loss energy region results in spectra showing discrete vibrational energies of the corresponding excited vibrational modes of the adsorbed molecules. The eigenfrequency of the harmonic oscillator $\omega=\sqrt{\frac{k}{m}}$ with k the force constant and m the oscillating mass describes the vibrational quantum of a single surface bound atom. For multiple atom systems the reduced mass μ has to be taken into consideration. As a result of the translational symmetry parallel to the surface and momentum conservation the following expression is valid

$$\vec{k}_s^{\|} = \vec{k}_i^{\|} + \vec{Q} + n\vec{G} \tag{2.2}$$

with $\vec{k}_s^{\|}$ and $\vec{k}_i^{\|}$ the momenta of the incoming and scattered electron, $\vec{Q}$ the momentum of the excited vibration and $\vec{G}$ a reciprocal lattice vector of the two dimensional Bravais-lattice (integer n). We assume n to be n = 0, thus the difference in parallel momentum of the incoming electron and the scattered electron corresponds to the momentum of the excited vibrational mode.

Dipole Scattering

In the Dipole scattering regime vibrational modes are excited through a long range (100 $\mathring{A}$) Coulomb interaction between the incident electron and the metal surface. Due

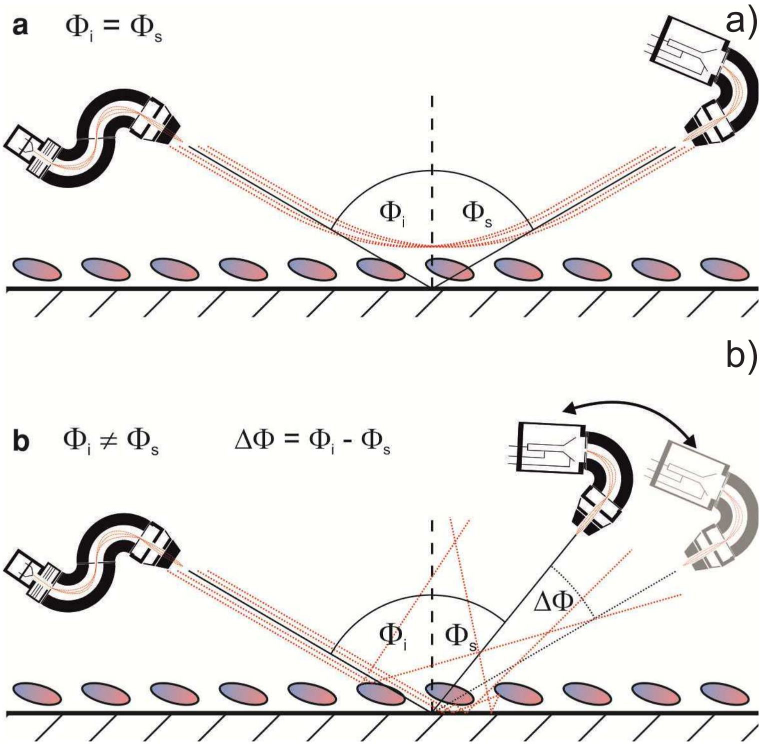

Figure 2.2: Schematic depiction of the HREELS scattering geometry for a) dipole and b) impact scattering. The incoming electron has the energy E_i and the impulse k_i. The angle of the incident electron beam Θ_i and of the scattered electrons Θ_s is 60° in specular measurement geometry. Image adopted from Reference [54]

to the electrons charge (and image potential inside the substrate) the incoming and scattered electron cause a time dependent long ranged electric field which field vectors lie perpendicular with respect to the surface. Vibrational modes perpendicular to the surface get amplified due to the image charge build up in the substrate in contrast to parallel oscillating dipoles that are quenched and not accessible in this scattering regime, in Figure 2.2 this observation is depicted. The resulting dipole moment sums up to 2 μ' for perpendicular orientated dipoles μ', since the image and the real dipole are orientated in the same direction. The result of these findings is a surface selection rule similar to infrared spectroscopy on metals.

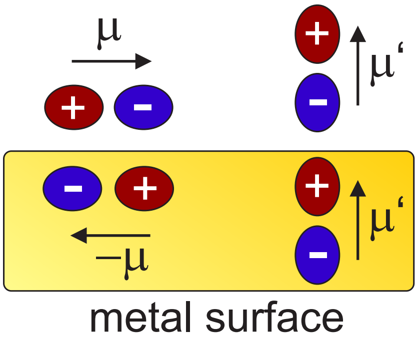

Figure 2.3: Schematic image of surface selection rules on a metal surface due to image charge build up. Dipoles orientated perpendicular on a metal surface μ' sum up to an overall twice as intense dipole moment $2\mu'$. Vibrational modes having a dipole moment parallel to the surface μ are quenched due to the inverse image dipole in the substrate.

The perpendicular component is conserved, whereas the difference in parallel momentum of the incident electron and scattered electron corresponds to the one of the excited vibrational mode. The momentum loss is therefore rather small. The intensity of the dipole scattered electrons exhibits a strong angular dependence. The specular geometry (dipole scattering regime) in HREELS is shown in Figure 2.2 a) having identical angles with respect to the the surface normal of the incident electrons and the scattered electrons ($\Theta_i = \Theta_s$). Derived from quantum-mechanical theory for inelastic scattering of low energy electrons by molecules adsorbed on metal surfaces as discussed in reference [Per77], the cross section $\frac{d\sigma}{d\Omega}$ can be described as a function of the scattering angle Θ_s

$$\frac{d\sigma}{d\Omega} = \left(\frac{m_e \mu e}{\pi \hbar^2}\right)^2 \frac{p_s}{p_i} \frac{1}{cos\Theta_s} \left(\frac{a_{\parallel}}{a^2}\right)^2 \tag{2.3}$$

with p_s and p_i the momenta of of the incoming and reflected electron, $a_{\parallel}$ and a components of the momenta involving the parallel and perpendicular parts of the momentum of the scattered and incident electrons, respectively. A pre factor composed of μ, and the electron mass m_e. Derived from Fermis Golden Rule the rate for the process in which the molecule is excited from the ground state $|A\rangle$ to a vibrational excited state $|B\rangle$ μ by an incident electron. This can be written as $\langle B|\mu_z|A\rangle$, in which μ_z is the component of the dipole moment operator of the perpendicular orientated molecule with respect to the surface. The calculated cross section of the dipole scattered electrons, plotted versus

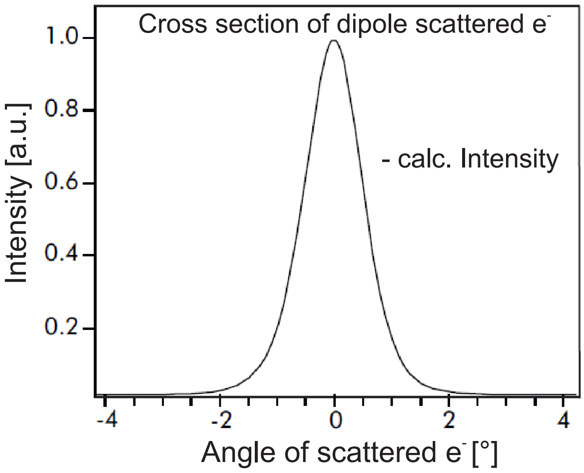

Figure 2.4: Cross section of dipole scattered electrons; Intensity versus scattering angle. In this image an angle of 0° corresponds to the specular geometry. Image adopted from Ref. [48]

the scattering angle is depicted in Figure 2.4 . The calculation according to formula 2.3 have been performed using an primary electron energy of $E_0 = 3\,\text{eV}$. The scattering angle is in reference to the specular angle which has been set to $\Theta_i = 60°$ in accordance to our experiments (In Figure 2.4 0° corresponds to specular geometry). The resulting graph shows that dipolar scattered electrons are found only in a very narrow angular window (calculated to ± 2°) around the specular direction. This so-called dipole lobe leads to the experimental discriminability of the different scattering mechanisms simply by rotation of the analyzer part of the spectrometer out of the specular geometry. For our experiments off-specular angles of 5° have been used.

Impact scattering

The impact scattering process is considered a short range interaction (in the order of $1\mathring{A}$) and is the result of a direct impact of the incoming electron with atomic core potentials on the sample. The theoretical description is far more complicated which is due to the fact that kinematical processes and multiple scattering events have to be considered [49] Since the angle of the scattered electrons is distributed over a wide range of angles the off-specular spectra are obtained by rotation of the analyzer part for more than 5° out of specular geometry, thus leaving the lobe of dipolar scattered electrons. The achievable intensities in this scattering regime are usually found to be decreased in intensity by two orders of magnitude compared to the specular geometry.

Negative Ion Resonance

The third scattering mechanism is the negative ion resonances. This mechanism was not investigated in this thesis and therefore only a brief overview will be given. The scattered electron is trapped in an unoccupied, molecular orbital and a negative charged ion is generated when the energy of an unoccupied, molecular state is equal to the kinetic energy of the incident electron (resonant). Usually, the lifetime of such an excited state is much shorter for molecules adsorbed on metal surfaces. This finding is attributed to the fact that additional decay channels into the metal substrate exist. Therefore it strongly depends on the strength of coupling of the unoccupied molecular orbitals to the electronic states in the substrate.

2.1.2 Ultra-High-Vacuum Chamber

In order to ensure that the observed vibrational losses only arise from the evaporated molecular species and that during the course of a measurement no noticeable contamination (adsorption of residual gas atoms/molecules) occurs on the metal single crystals in use the experiments are performed under ultra high vacuum conditions. The base pressure in the preparation and spectrometer chamber was better than $2x10^{-10}$ mbar. In Figure 2.5 a schematic image of the experimental setup is given. The two chambers are made out of stainless steel and are separated by a huge gate valve. The top part is equipped with all devices needed for sample preparation. That is the self-made molecule doser, a noble gas sputter gun, a Spectra Satellite LM61 (200 amu) quadrupole mass

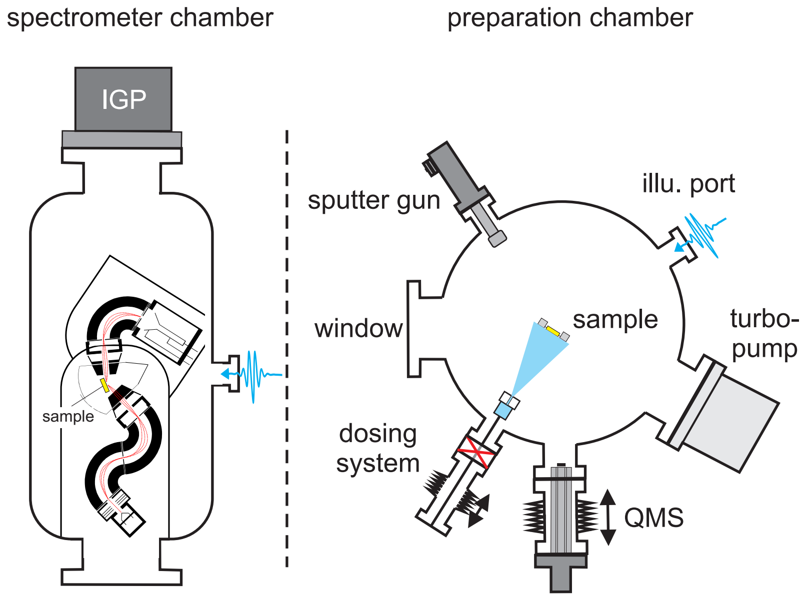

Figure 2.5: Sketch of both UHV chambers used in this work. Left side shows the bottom spectrometer chamber with the relative position of the attached components. Right side shows the upper preparation chamber and the connected equipment.

spectrometer a XYZ manipulator together with a cryostat (the cryostat is mounted via a 360° rotatable stage), a transfer system for changing the used sample without the need to vent the chamber and break the vacuum and a turbo molecular pump. The lower part accommodates the DELTA 0.5 spectrometer and a Varian Starcell 300 ion pump is attached to the chamber. The desired ultra high vacuum is achieved using a setup of three pumps for the preparation chamber, two turbo molecular pumps (Balzers TMU 261 P and a Pfeiffer TMU 071P) and a Pfeiffer MD4 membrane pump that provides the rough vacuum in order to operate the turbo pumps. The pressure reading of both chambers is done using Varian ion gauges. Both chambers are equipped with UV transmitting windows that allow illumination experiments to be carried out.

2.1.3 Au(111), Bi(111) and Bi(114) Substrates

Gold crystalize in the face centered cubic (fcc) structure. Cutting of the bulk in the desired plane exposes a trigonal surface symmetry along the (111) direction. The gained surface shows tightest packing and the Au(111) surface yields its characteristic herringbone reconstruction resulting in a $(22\sqrt{3})$ unit cell (due to a lattice mismatch). This leads to streaks having alternating domains with fcc and hexagonally closed packed (hcp) units. This is visible in STM as the famous zigzag pattern. In a previously published HREEL study of the bare Au(111), grown on a mica substrate, a surface plasmon, located at 2.49 eV loss energy was observed. The primary electron energies employed in this study were in the range of 25 eV to 40 eV (We employed 15.5 eV E_0 for our electronic HREEL investigations) [55, 56]. Surprisingly this feature, assigned to surface plasmon is not quenched upon adsorption of molecules. In contrast to this data we did not observe said surface plasmon in our experiments furthermore would the surface plasmon be quenched upon molecular adsorption even in the monolayer regime. The reactivity of the chosen substrates, concerning the type and strength of adsorbate bonding, differs. Gold is the most inert metal known, whereas bulk Bi ,a semiconductor, is more reactive and the element with the least thermal conductivity. Bismuth crystallizes in the rhombohedral structure. Depending on the cutting direction of bulk Bismuth one can receive surfaces with very different properties ranging from semi-metallic Bi(111) to metallic Bi(114) [57, 58]. The Bi(114) exhibits another interesting feature. In contrast to other orientations Bi(114) shows channel like rows along its surface with a periodicity of 3 nm. The channels dimension are wide enough to allow for molecule adsorption which we will show in Chapter 8.

The Au(111), Bi(111) and Bi(114) crystal are prepared in the upper UHV preparation chamber. The aim of the preparation is to produce well defined surfaces for adsorption studies. The single crystal substrates have been prepared using a standard inert gas sputter and thermally annealing technique. The inert gas sputter process employs Ar^+-ions are accelerated towards the sample via an ion gun with 0.9 - 1.2 keV. The incident angle is 45°. The partial pressure inside the preparation chamber was in the order of $2x10^{-6}$ mbar. The detectable ion current measured between the sample and ground was in the range of 3 - 5 μA. Afterwards the surface was annealed for 20 min at a sample temperatures of $T_{Au(111)} = 750$ K and $T_{Bi} = 420$ K, respectively. This procedure is a standard procedure and valid for many metal surfaces [59].

2.1.4 Sample preparations

In this thesis a Au(111), a Bi(111) and a Bi(114) single crystal (provided by MaTecK GmbH) have been used (crystal diameter is ø = 10 mm). The crystals were mounted with Ta-wires with a diameter of ø = 0.3 mm in the sampleholder. The Ta-wires serve for more purposes, despite for fixing the sample in position the resistive heating of the sample is achieved as well and temperatures up to 900 K can be reached. And furthermore it connects the crystal to the liquid nitrogen cooled cryostat that allows minimum temperatures of 90 K. The sample holder is designed as a left and a right side part that are each contacted to an electrical feed-through (resistive heating)and are the isolation between these two parts is realized by 0.5 mm thick sapphire plates that as well offer good enough thermal coupling. The temperature of the crystal can be measured with a type K thermocouple that is directly inserted into a small hole drilled in the crystal and connects to a Lakeshore 340 digital PID temperature controller for data processing. The investigated molecules, discussed in this work, are kept in a home-build evaporater (knudsen-cell type). This evaporator is connected to the UHV preparation

Table 2.1: Different parameters for the sample preparation of the investigated systems.

system		**Doser temp**	**Sample temp.**
Au(111)	GNR	420 K	90 K
Au(111)	GNR-1N	420 K	90 K
Au(111)	GNR-2N	420 K	90 K
Au(111)	TAPP	455 K	300 K
Au(111)	TAPP-$(C_3F_7)_2$	460 K	300 K
Au(111)	TAPP-Cl_4-$(C_3F_7)_2$	475 K	300 K
Au(111)	α-8T	510 K	300 K
Au(111)	PTCDA	540 K	300 K
Bi(111)	DMC	380 K	120 K
Bi(114)	Nitro-Spiropyran	360 K	120 K

chamber and is separated by a gate valve. The doser is pumped directly by a turbo molecular pump (Pfeiffer TMU 071P) together with another Pfeiffer MD4 membrane pump that provides the pre-vacuum conditions. The gate valve between the preparation chamber and the dosing unit allows for the exchange of the used molecules without the need for breaking the vacuum. To deposit the molecules (solid form) we thermally evaporated the solids from the knudsen-cell. The macor ceramic crucible is therefore wrapped with a heating wire and temperatures of 600 K and more are achievable and the doser temperature is monitored via a type K thermocouple. The molecules leave the crucible through a small 1 mm diameter hole and a conical molecular beam is generated. The beam can be blocked by a manually driven shutter that gives more control for exact dosing conditions. All molecules used in this theses were degassed inside the dosing unit for several hours well below the evaporation temperature (at ambient conditions) to ensure cleanliness and the absence of water traces. The amount of evaporated molecules is followed with the QMS at a representative mass of the molecule. Suitable fragments are derived either via published data or by performing a residual gas analysis during the evaporation in the preparation chamber. The deposition conditions like sample temperature and doser temperature are listed in Table 2.1 for each system investigated in this thesis. The mentioned condition apply unless otherwise stated in the corresponding chapter.

2.1.5 Temperature Programmed Desorption Spectroscopy

In order to quantify the adsorbed amount of molecules after evaporation and to gain insight into the adsorption behavior in sub-monolayer and multilayer coverages we employed temperature programmed desorption spectroscopy (TPD). The intensity of the QMS signal of a mass (or a fragment originating from the parent molecule) corresponding to the evaporated molecule is detected as a function of the substrate temperature. The attached Lakeshore temperature controller is able to produce very linear heating rates that are typically in the range of 1 Ks^{-1}. Under the assumption that all adsorbed molecules occupy energetically equal binding sites the desorption rate R can be described using the Polanyi-Wigner-equation as shown in (2.4) [60] and gives the relation of the rate of desorption $\frac{d\theta}{dt}$ with the desorption energy E$_{Des}(\theta)$. With $\nu(\theta_0)$ the pre-exponential factor, n the order of desorption, θ_0 the initial coverage, k the Boltzmann constant and the temperature T.

$$\frac{d\theta}{dt} = -\nu(\theta_0)\theta_0^n exp\left(\frac{E_{Des}\theta_0}{kT}\right) \tag{2.4}$$

The desorption energy $E_De s$ is for non activated chemisorption processes equal to the binding energy E_B. If we connect this expression to the desorption rate we find that

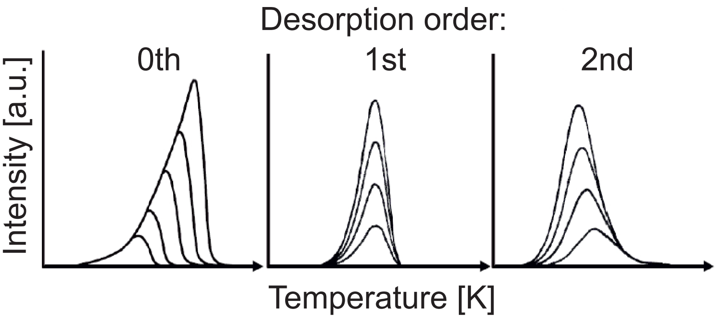

Figure 2.6: Thermal desorption spectra for a linear heating ramp for 0th, 1st and 2nd order desorption processes, adopted from reference [48]

the measured TPD spectra result in typical shapes (coverage dependent and defined by the corresponding desorption order n) which is depicted in Figure 2.6.

2.1.6 Density functional theory

The calculations were performed by Friedrich Maaß within his master thesis [54] employing the program ORCA 2.9.1 [61]. The density functional theory (DFT) is a versatile tool for quantum mechanical calculations yielding molecular properties like vibrational energies and electronic excitation energies [62]. It is based on the findings of Hohenberg and Kohn [63] that the ground-state energy of a system only depends on the electron density. Here the integral of the electron density relates to the number of electrons, the maxima the position of the corresponding atom cores and the height of the maxima the core charge [64]. The big advantage of this method is the fact that no matter how big the investigated system is one only has to consider 3 parameters. On the downside the functional describing the ground-state density as a function of the electron density can only be estimated. The functional can be divided into T(ρ), the kinetic energy of the electrons, E_{ne} the attractive interaction between the core and the electrons part and the electron-electron interaction E_{ee}. The last mentioned can be divided into the classical Coulomb term J(ρ) and the exchange term K(ρ). The interaction between the cores is considered constant based on the Born-Oppenheimer-Approximation [65].

$$E(\rho))T(\rho) + E_{ne}(\rho) + J(\rho) + K(\rho) \tag{2.5}$$

A remarkable increase in accuracy was achieved via the introduction of orbitals in form of one electron Schrödinger equations by Kohn and Sham [66]. This approach increases the number of parameters from 3 to 3N at high computional cost thus needing powerful computers that are nowadays easily accessible. Employing the Kohn-Sham-equations an exact value for the kinetic energy of non interacting electrons is accessible.

$$(-\frac{1}{2}\nabla^2 + \nu_{eff}(\vec{r}) - \epsilon_j)\varphi_i(\vec{r}) = 0 \tag{2.6}$$

The difference between the calculated value for the non-interacting electrons and the real electrons is known as the exchange term and is condensed in the correlation term. This term can not be calculated exactly but there exist functionals to approximate this term. In this work the functional B3LYP by Becke, Perdew, Lee, Yang and Parr were used.

Chapter 3

Graphene nanoribbons on Au(111)

In the past decades invention and development of electronic devices gained more and more attention. Increasing computing power and improved mobility grew a strong demand for the ability to down scale integrated circuits and related components. This bare necessity in nanotechnology, when the atomic scale is reached, will rise the need for new materials and methods in achieving these goals since with common techniques and materials a certain threshold of minimization could not be overcome [22, 23].

One very promising candidate, believed to revolutionize the world of electronics, was the two dimensional, carbon based graphene that gained worldwide attention since it first preparation back in 2004 [67]. Graphene should be the substitute for doped silicon field-effect transistors (FETs) with its unique properties showing a high charge carrier mobility and of course its unmatched one atom thinness [68–70]. The application of transistors being mainly comprised of graphene show remarkable properties [69, 71, 72] but soon revealed a major draw-back. Large-area-graphene based transistors cannot be switched "off" due to the lack of a band gap [22, 73, 74].

To overcome this problem and generate a band gap in a controllable and reliable fashion remains a challenge thereafter. Possible routes to alter the properties of graphene to match the high expectations and open a band gap are for example biasing stacked layers of graphene sheets [75, 76] or applying strain to graphene honeycomb sheets [77, 78]. The most promising approach with regard to the properties and producibility is by far the a method using a lateral constriction in so-called "quasi one-dimensional graphene nanoribbons which leads to a band gap that furthermore is tunable by the edge shape and width of the nanoribbon [79–81]. It was found that FETs and metal-oxide-semiconductor field-effect transistors (MOSFETs) built from those narrow graphene nanoribbons exhibit high "on/off" ratios which is the crucial parameter when thinking of applications in computational devices [35, 71]. Another way of band gap engineering is the method of heteroatom doping but employing nowadays techniques for heteroatom doping exhibit a delicate problem namely unevenly allocation of the dopant. Thus leading to different band gap shifts since the relocation of the gap strongly depends on the chemical surrounding of the dopant atom [82]. After successful implementation of the essential band gap another difficulty has to be challenged. With regard to the manufacturing of such transistors another important parameter has to be taken into account. That is the interaction of the nanoribbon with the underlying metal electrode material on which it is adsorbed. The effect of metal substrates on organic molecules leading to a significant level alignment of the molecular band structure [83,84] with respect to the Fermi level of the used electrode material was found for graphene [85, 86], for the pure carbon based graphene nanoribbons [87] as well as for hetero atom (like nitrogen) doped sheets [88]. Nowadays commonly used techniques for the GNR building process are lithography [81,89–92] and the unzipping of carbon nanotubes (GNTs) [93–98] usually leading to an undefined edge structure and quite wide graphene nanoribbons (GNR) with band gaps impractical for application.

One very promising solution so far to overcome the fabrication problems mentioned above was found in the so called "bottom up" fabrication process by Cai *et al.* in 2010 [99]. Obtaining a GNR via a surface catalyzed cyclodehydrogenation of a halogen activated precursor molecules (schematically shown in Figure 3.1). These precursor molecules can easily be evaporated and in situ form the desired GNRs in a controllable fashion upon applying heat to the substrate [100].

3.1 Graphene nanoribbon fabrication

Figure 3.1 shows a schematic of the involved GNR fabrication steps that are induced via heating of the substrate. The aromatic center contains the star shaped triphenylene core made up by four condensed benzene rings. The 6 and 11 position are substituted with bromine atoms. The carbon bromine bonds are easily cleaved homolytical upon heating of the sample to 540 K thus leading to the activation of the remaining carbon atoms in 6 and 11 position that leads to the coupling of monomer units and results in the polymer phase. The benzene rings in 1,2,3 and 4 position are clearly twisted out of the molecular plane which was found by single crystal X-ray diffraction [101]. The result of such measurements is shown for the double nitrogen doped 2N-GNR in Appendix A, Figure A.2 and is indicated in Figure 3.1. This propeller like shape remains in the polymer phase even though due to contact to the underlying metal substrate a smaller angel of deflection is expected. These geometrical changes during the GNR formation will be significant with regard to the characterization of the different phases observed via vibrational HREELS shown in section 3.1.1. When the sample is heated further up to 710 K hydrogen atoms are released and the cyclodehydrogenation reaction finally leads to the planar, fully aromatic GNR phase. The lateral and longitudinal expansion of the aromatic system should have a tremendous effect on the electronic structures of

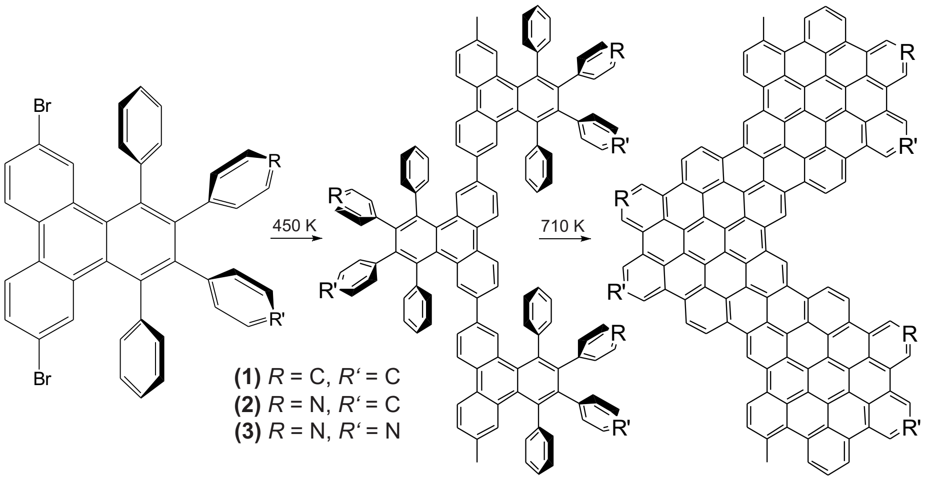

Figure 3.1: Schematic of GNR formation steps from the monomer to the graphene nanoribbon phase upon heating to 540 K and 710 K, respectively. **(1)** pristine GNR, **(2)** singly nitrogen doped 1N-GNR and **(3)** doubly nitrogen doped 2N-GNR

the related species.

This bottom up fabrication method yielding a nanometer wide graphene nanoribbon with very precise edges was introduced recently by Cai et al. in 2010 [99]. Figure 3.2 a) shows a STM image of the on surface synthesis of the prior discussed GNR on a Au(111) substrate adapted from Reference [99]. The average length distribution is shown in the inset of Figure 3.2(b) and was found to be at around 20 nm length.

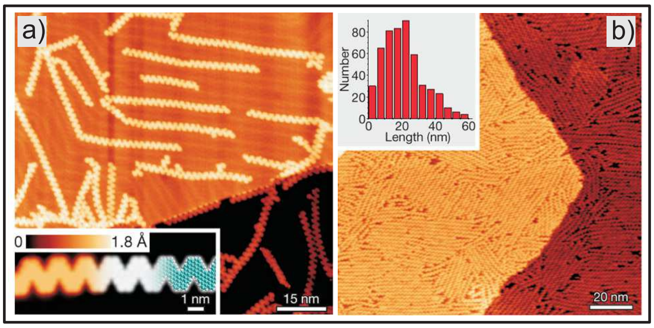

Figure 3.2: STM images of GNR on Au(111) adapted from Reference [99]. a) general appearance of GNR chains; inset depicts actual image with molecular structure overlay, b) densely packed GNR phase; inset shows average length distribution

In this chapter we will show and discuss the bottom up fabrication process and the electronic properties of the pristine chevron graphene nanoribbon precursor 6,11-dibromo-1,2,3,4-tetraphenyltriphenylene (GNR) and its two nitrogen doped derivates 4-(6,11-Dibromo-1,3,4-triphenyltriphenylen-2-yl)pyridine (1N-GNR) and 4,4-(6,11-Dibromo-1,4-diphenyltriphenylene-2,3-diyl)dipyridine (2N-GNR) as well as the influence of the nitrogen doping on the band gap of the nanoribbon phase derived from vibrational and electronic HREELS measurements.

3.1.1 Pristine Graphene nanoribbon

The molecular structure of the pristine GNR precursor **(1)**, is shown in Figure 3.3. The four benzene rings attached to the triphenylene core show a considerable propeller like deflection angle with respect to the molecular plane which is due to their sterical hinderance among each other which is nicely seen in the single crystal structure of the 2N-GNR molecule [102]. During the GNR fabrication the orientation of the benzene rings will drastically change in the cyclodehydrogenation step when an overall planar orientation with an extended aromatic system is established. This change in orientation will therefore lead to a prominent alteration of the vibrational spectra measured with HREELS among remarkable changes in the electronic properties as well. In order to gain conclusive informations about the geometrical changes upon GNR build up an its adsorption properties we performed angle dependent HREELS measurement.

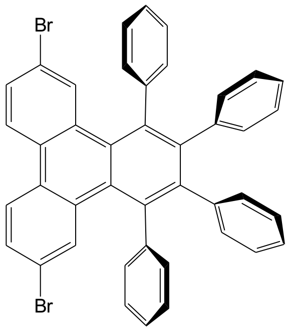

Figure 3.3: Structure of the pristine GNR precursor molecule **(1)**.

As a first step in order to gain more insights in the ongoing process of GNR formation, TPD spectra were measured after evaporation of the precursor molecules on the Au(111) substrate. The heating rate during these experiments was $\beta = 1Ks^{-1}$ and the molecular fragments are detected using a quadrupole mass spectrometer (QMS). The TPD spectra depicted in Figure 3.4 stands exemplary for the GNR build up. As depicted the observed masses m = 82 z/e, m = 97 z/e and m = 111 z/e are assigned to $[H^{81}Br]^+$, $[C_7H_{13}]^+$ and to the doubly charged $[C_{18}H_6]^{2+}$ fragment respectively. The feature with the lowest desorption temperature at around 352 K (α_1) is assigned to desorption of the multilayer. The feature at 436 K desorption temperature ist assigned to the second layer (α_2). Both traces belonging to $[H^{81}Br]^+$ with mass 82 and $[C_7H_{13}]^+$ with mass 97 remain visible in the spectrum and show a final peak at 573 K followed by a significant drop in intensity meaning that no bromine is longer present for the HBr formation.

The fact that the hydrogen bromine species is observed at such low temperatures can only be explained by its formation inside of the QMS itself among cleaved fragments of the desorbed second layer since the cyclodehydrogenation offering free hydrogen for this recombination reaction takes place at much higher temperatures. During the first heating step to 540 K, yielding the polymer phase, the carbon bromine bond in the monolayer coverage is cleaved and bromine radicals recombine with hydrogen and are detected in the QMS. Upon further annealing up to 710 K cyclodehydrogenation takes place and the graphene nanoribbon is achieved. Once the nanoribbon phase is formed it can not be desorbed from the gold substrate and the sample needs to be cleaned by repeated Ar$^+$ sputtering and annealing cycles prior to following measurements to ensure a clean surface.

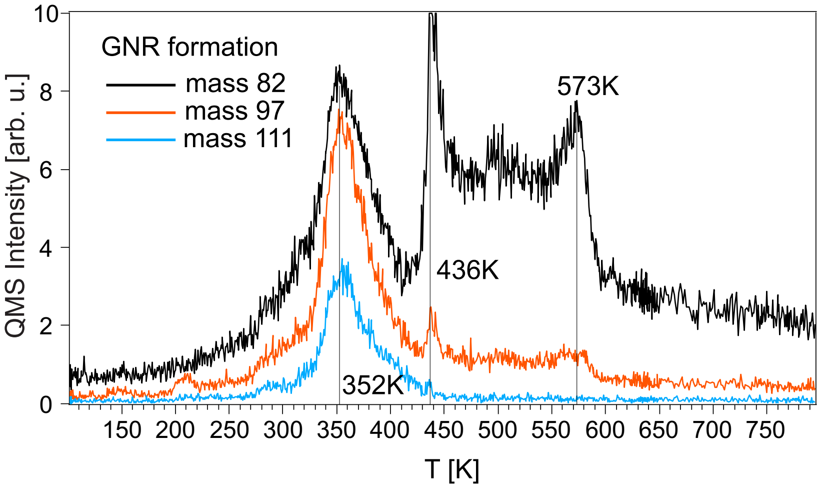

Figure 3.4: Mass spectra for different observed molecular masses taken during a TPD experiment ranging from 100 k up to 800 K. The observed mass m = 82 z/e is assigned to the $[HBr]^+$ fragment (black line), mass m = 97 z/e arises from $[C_7H_{13}]^+$ (red line) and the mass m = 111 z/e to the twice charged $[C_{18}H_6]^{2+}$ fragment (blue line). The heating rate employed was $\beta = 1Ks^{-1}$.

The precursor molecules were evaporated on a Au(111) sample kept at 100K. The initial coverage chosen was well in the multilayer regime to ensure a high coverage monolayer. The preparation is valid for the latter two derivatives as well. The monomer HREEL spectra represents the multilayer coverage. Due to the relative low countrates for the vibrational losses in HREEL spectra a higher primary electron energy was chosen namely E$_0$ = 5.0 eV for the monomer spectra unless otherwise stated. For the polymer and the nanoribbon phase the primary electron energy was set to E$_0$ = 3.5 eV. The achieved

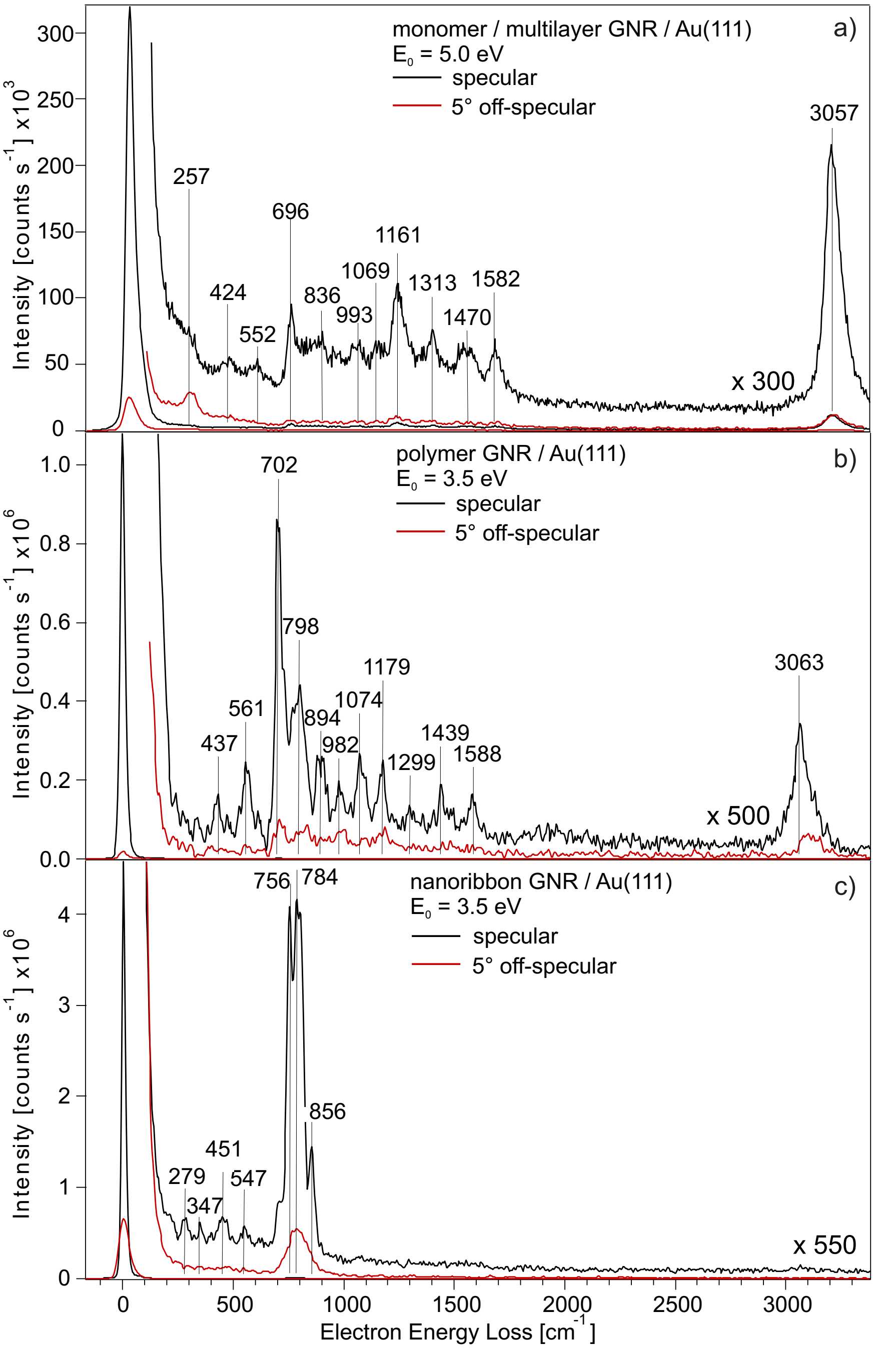

Figure 3.5: Vibrational HREEL spectra measured with a primary electron energy of E_0 = 5 eV (monomer) and 3.5 eV (polymer and nanoribbon) in specular (solid black line) and in 5°-off-specular geometry (solid red line), respectively of the GNR formation of the precursor 6,11-dibromo-1,2,3,4-tetraphenyl-triphenylene **(1)** on Au(111) upon heating.

overall resolutions measured as the full width at half maximum (FWHM) were in the range from 25 cm^{-1} (3.1 meV) for specular geometry and up to 40 cm^{-1} (5 meV) for off-specular geometry. The two heating steps involved in the GNR fabrication were maintained for 15 minutes each unless otherwise stated.

Figure 3.5 shows the in specular and in 5°-off-specular geometry measured HREEL spectra of the precursor molecule in a), followed by the polymer phase in b) and finally the chevron GNR phase in c). See Table 3.1 for a detailed assignment of the observed losses. The rather complex monomer spectrum of the pristine GNR is shown in Figure 3.5 a). The loss feature observed at 257 cm^{-1} is assigned to the $\delta_(C-Br)$ bending mode, this feature vanishes upon heating and is not observable in the polymer 3.5 b) nor in the nanoribbon phase in 3.5 c). The out-of-plane bending mode of the carbon skeleton δ_{C-C-C} is located at 424 cm^{-1} in the monomer and shifts to 437 cm^{-1} in the polymer and up to 451 cm^{-1} in the nanoribbon phase. An additional out-of-plane mode, namely δ_{C-C-C}, is found at 552 cm^{-1} for the monomer (a), at 561 cm^{-1} for the polymer (b) and at 547 cm^{-1} for the GNR phase respectively. The phenyl ring torsion mode τ_{C-C} with some contribution of δ_{C-H} appears at 696 cm^{-1} (a), at 702 cm^{-1} (b) and in the GNR phase (c) at 756 cm^{-1} with an enormous increase in its dipole activity in the latter two due to the vast geometrical changes in the nanoribbon case (complete planar with respect to the surface). Many of the observed features arise from out-of-plane bending vibrations of the terminal hydrogen atoms δ_{C-H}. In the monomer spectrum they can be found at 836 cm^{-1} and 993 cm^{-1} alternatively. For the polymer these features arise at 798 cm^{-1} and 982 cm^{-1}. And in the nanoribbon phase at 784 cm^{-1} and 856 cm^{-1} respectively. At 1069 cm^{-1} (a) and 1074 cm^{-1} (b) dipole active, in-plane bending modes from δ_{C-H} are observed. More in-plane modes arising from bending δ_{C-C} and stretching vibrations $\nu_{C=C}$ can be found in the monomer at 1161 cm^{-1}, 1313 cm^{-1}, 1470 cm^{-1} and 1582cm^{-1} respectively. And in the polymer spectrum at 1179 cm^{-1}, 1299 cm^{-1}, 1439 cm^{-1} and 1588 cm^{-1} as well. The hydrogen stretching vibration ν_{C-H}, which exhibits a very strong dipole activity, shows up at 3057 cm^{-1} in (a) and at 3063 cm^{-1} in (b). In the GNR spectrum (c) this mode is completely absent.

The change in appearance and most of all their pronounced dipole activity in spectrum (c) (strong increase towards the GNR phase) clearly depicts the underlying geometrical transformation in the GNR fabrication process. The monomer phase consists of rather randomly oriented molecules and the propeller like deflected benzene rings dominate the resulting vibrational spectrum (in-plane ν_{C-H},$\nu_{C=C}$). When heating to 540 K the transition to the polymer occurs, leaving a well defined structural motif on the surface. The tilted orientation of the four benzene ring remains but is less pronounced due to steric effects of the substrate (in-plane ν_{C-H}, dipole active) and the with respect to the surface planar triphenylene core contributes more clearly with its out-of-plane τ_{C-C},

Table 3.1: Assignment of vibrational modes for different 6,11-dibromo-1,2,3,4-tetraphenyl-triphenylene phases on Au(111) as indicated. All vibrational frequencies are given in cm^{-1}. IR/Raman data for triphenylene adapted from Ref. [103–105][a]. IR/Raman data for benzene adapted from Ref. [105][b]. IR data for bromobenzene adapted from Ref. [106, 107][c]. ν, indicates stretch; δ, bending; τ, torsion; oop, out-of-plane; ip, in-plane. w, indicates weak; m, medium; s, strong; vs, very strong. A strong dipole activity is indicated by (da).

vibrational mode		**monomer**	**polymer**	**nanoribbon**	**IR data**
δ_{C-Br}	oop	257w	–	–	240[c]
δ_{C-C-C}	oop	–	–	279w	279/282[a]
δ_{C-C-C}	oop	–	–	347w	380[c]
δ_{C-C-C}	oop	424w	437w	451w	420/422[a]
δ_{C-C-C}	oop	552w	561m	547w	544/550[a]
δ_{C-H},τ_{C-C}	oop	696m	702vs(da)	756vs(da)	688[b],699/772[a]
δ_{C-H}	oop	–	798s(da)	784vs(da)	777/780[a]
δ_{C-H}	oop	836w	–	856m(da)	850/851[a]
δ_{C-C}	ip	–	894m	–	869[a]
δ_{C-H}	oop	993w	982w	–	994[a,b]
δ_{C-H}	ip	1069w	1074m	–	1040[b],1052/1062[a]
δ_{C-C}	ip	1161s(da)	1179m(da)	–	1179[b],1162[a]
$\nu_{C=C}$	ip	1313m	1299w	–	1298/1318[a]
$\nu_{C=C}$	ip	1470m	1439m	–	1434[a],1480[b]
$\nu_{C=C}$	ip	1582m	1588m	–	1580[a],1587[b]
ν_{C-H}	ip	3057vs(da)	3063s(da)	–	3058[a],3088[b]

dipole active modes. In the last step, the planar GNR is obtained and the observed vibrational modes originating from out-of-plane modes δ_{C-H} and τ_{C-C}, possessing a very strong dipole activity, remain in the spectrum.

3.1.2 Singly Nitrogen Doped Graphene Nanoribbon

The structure of the singly nitrogen doped 1N-GNR precursor molecule (**2**) is shown in Figure 3.6. The overall molecular orientation of the molecule is not changed upon nitrogen doping and the propeller like shape of the three benzene and one pyridine ring persists while the dibromo substituted triphenylene core remains in its planar orientation.

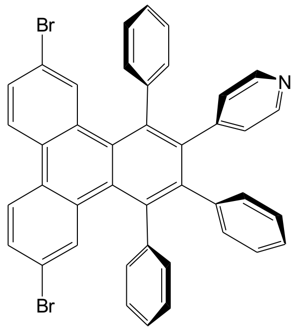

Figure 3.6: Structure of the singly nitrogen doped 1N-GNR precursor molecule (**2**).

The GNR formation was followed with vibrational HREEL spectra in specular and 5-7°-off-specular geometry as shown in Figure 3.7. See Table 3.2 for a detailed list of all observed vibrational modes and their assignment. The monomer multilayer spectrum in Figure 3.7 a) shows relative broad signals which is due to the comparable high primary electron energy in this measurements. The carbon bromo bending mode δ_{C-Br} is therefore not visible and masked by the right side of the elastic peak. The first distinct mode at 339 cm^{-1} arises from out-of-plane bending modes δ_{C-C-C} of the pyridine ring. Out-of-plane modes δ_{C-C-C} originating from the triphenylene core are found in all three phases of the GNR fabrication process, namely at 557 cm^{-1}, at 562 cm^{-1} and in the nanoribbon at 565 cm^{-1} respectively. The intense out-of-plane bending modes of δ_{C-H} can be found in all phases as well. In the monomer at 701 cm^{-1} and 797 cm^{-1}, in the polymer at 695 cm^{-1} and at 767 cm^{-1} and in the GNR phase at 749 cm^{-1} and at 793 cm^{-1} respectively. Further out-of-plane vibrations from δ_{C-H} are observed in 3.7 a) at 982 cm^{-1} and in 3.7 b) at 963 cm^{-1} alternatively but absent in the nanoribbon phase in 3.7 c), indicating that these observed C-H groups are probably the ones that dissociate during the cyclodehydrogenation process in the GNR build up at 710 K substrate temperature. In-plane bending modes arising from δ_{C-H} and δ_{C-C} are observed for the monomer phase at 1070 cm^{-1} and 1162 cm^{-1}. For the polymer phase these vibrations are found at 1063 cm^{-1} and 1156 cm^{-1}, respectively. The in-plane stretching modes of

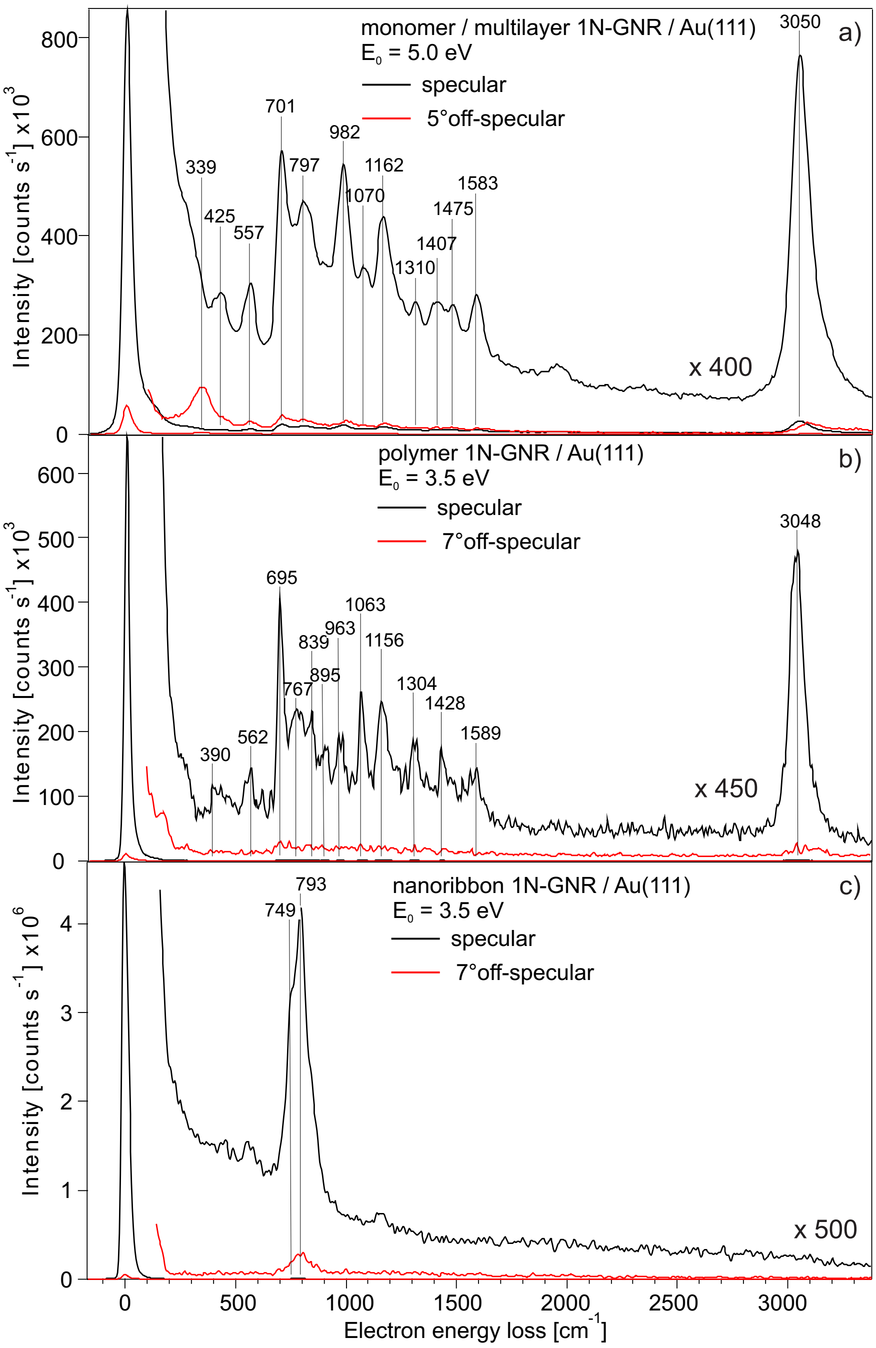

Figure 3.7: Vibrational HREEL spectra measured with a primary electron energy of E_0=3.5 eV (E_0=5 eV for monomer) in specular (solid black line) and in 5-7°-off-specular geometry (solid red line), respectively of the 1N-GNR formation of the 4-(6,11-Dibromo-1,3,4-triphenyltriphenylen-2-yl)pyridine precursor **(2)** on Au(111) upon heating.

the carbon skeleton $\nu_{C=C}$ make up a large portion of the monomer and polymer HREEL spectra, while are not observable in the nanoribbon phase. In a) they can be found at 1310 cm^{-1}, 1407 cm^{-1}, 1475 and at 1583 cm^{-1} and for the polymer shown in Figure 3.7 b) at 1304 cm^{-1}, at 1428 cm^{-1} and at 1589 cm^{-1}, respectively. At 3050 cm^{-1} in the monomer case and at 3048 cm^{-1} in the polymer, respectively, the very intense, dipole active, and spectra dominating C-H stretching vibration assigned to ν_{C-H} appears.

Their origin is obviously found in the propeller like twisted benzene/pyridine rings and thus their stretching exhibits a large dipole moment change perpendicular with respect to the underlying Au(111) substrate. After the final annealing step resulting in the GNR phase, these twisted rings are embedded in the planar nanoribbon after the cyclodehydrogenation took place and no ν_{C-H} stretching modes are observable anymore. In comparison with the pristine GNR no significant differences could be

Table 3.2: Assignment of vibrational modes for different 4-(6,11-Dibromo-1,3,4-triphenyltriphenylen-2-yl)pyridine phases on Au(111) as indicated. All vibrational frequencies are given in cm^{-1}. IR/Raman data for triphenylene adapted from Ref. [103–105][a]. IR/Raman data for benzene adapted from Ref. [105][b]. IR data for bromobenzene adapted from Ref. [106,107][c]. IR data for pyridine adapted from Ref. [108][d]. ν, indicates stretch; δ, bending; τ, torsion; oop, out-of-plane; ip, in-plane. w, indicates weak; m, medium; s, strong; vs, very strong. A strong dipole activity is indicated by (da).

vibrational mode		**monomer** a)	**polymer** b)	**nanoribbon** c)	**IR data**
δ_{C-C-C}	oop	339m	–	–	370[d]
δ_{C-C-C}	oop	–	390w	–	380[c]
δ_{C-C-C}	oop	425m	–	–	420/422[a]
δ_{C-C-C}	oop	557m	562w	565w	544/550[a]
δ_{C-H},τ_{C-C}	oop	701s(da)	695s(da)	749vs(da)	688[b],699/772[a]
δ_{C-H}	oop	797s(da)	767m	793vs(da)	777/780[a]
δ_{C-H}	oop	–	839m	–	850/851[a]
δ_{C-C}	ip	–	895w	–	869[a]
δ_{C-H}	oop	982s(da)	963w	–	994[a,b], 995[d]
δ_{C-H}	ip	1070w	1063m(da)	–	1040[b],1052/1062[a]
δ_{C-C}	ip	1162s(da)	1156m(da)	–	1179[b],1162[a], 1160[d]
$\nu_{C=C}$	ip	1310w	1304m	–	1298/1318[a]
$\nu_{C=C}$	ip	1407w	1428w	–	1434[a],1480[b]
$\nu_{C=C}$	ip	1475w	–	–	1496[a],1480[b], 1460[d]
$\nu_{C=C}$	ip	1583m(da)	1589w	–	1580[a],1587[b], 1590[d]
ν_{C-H}	ip	3050vs(da)	3048vs(da)	–	3058[a],3088[b],3080[d]

observed. When advancing from the monomer to the polymer phase the most prominent changes in the appearance of the HREEL spectra is the increased intensity of the bending and torsion modes assigned to δ_{C-H},τ_{C-C} located at around 700 *cm*$^{-1}$ while the other modes remain less pronounced, this finding is true for both systems (GNR and 1N-GNR). As mentioned in section 3.1 the major indicator for the GNR formation is the vanishing of the ν_{C-H} mode due to the alignment of the benzene/pyridine rings to the triphenylene core. In both investigated system the nanoribbon phase spectrum is dominated by out-of-plane modes ranging from 750 *cm*$^{-1}$ to 800 *cm*$^{-1}$. The fabrication process was very effective and the HREEL spectra reveal the perfect planar orientation of the nanoribbon.

3.1.3 Doubly Nitrogen Doped Graphene Nanoribbon

The molecular structure of the doubly nitrogen doped 2N-GNR precursor molecule is shown in Figure 3.8.

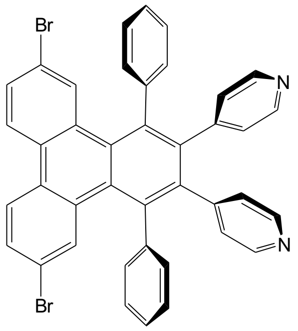

Figure 3.8: Structure of the 2N-GNR precursor molecule **(3)**.

The molecular geometry is not changed in comparison to the first two GNR precursor molecules. Since the feasibility of the bottom up GNR fabrication process was very successful proven for the pristine carbon precursor and the singly nitrogen doped analog, the focus for the investigation of the 2N-GNR precursor molecule was the final graphene nanoribbon phase. Figure 3.9 shows the in specular (black line) and in 5°-off-specular (red line) geometry measured vibrational HREEL spectra of the 2N-GNR phase **(3)**. The primary electron energy was $E_0 = 3.5eV$. For a complete list of the vibrational modes and the corresponding assignments see Table 3.3. Out-of-plane vibrations of the carbon skeleton δ_{C-C-C} are observed at 274 cm^{-1}, at 392 cm^{-1} and at 539 cm^{-1} respectively. Weak vibrational modes arising from in-plane bending of δ_{C-H} and δ_{C-C} are found in the spectrum as well. Three very pronounced losses are located at 760 cm^{-1}, 809 cm^{-1} and at 860 cm^{-1} respectively. The first feature is assigned to the out-of-plane torsion mode τ_{C-C} of the carbon skeleton. The latter two arise from out-of-plane bending modes δ_{C-H} of the hydrogen located at the molecular edges of the nanoribbon. All three intense vibrational modes exhibit a strong dipole activity. At 1033 cm^{-1}, 1069 cm^{-1} and 1261 cm^{-1} respectively weak in-plane modes originating from δ_{C-H}, δ_{C-C} and $\nu_{C=C}$ are observed. These findings lead to the conclusion that the nanoribbon phase adsorbs in a most planar geometry with respect to the Au(111) substrate underneath but with some imperfection.

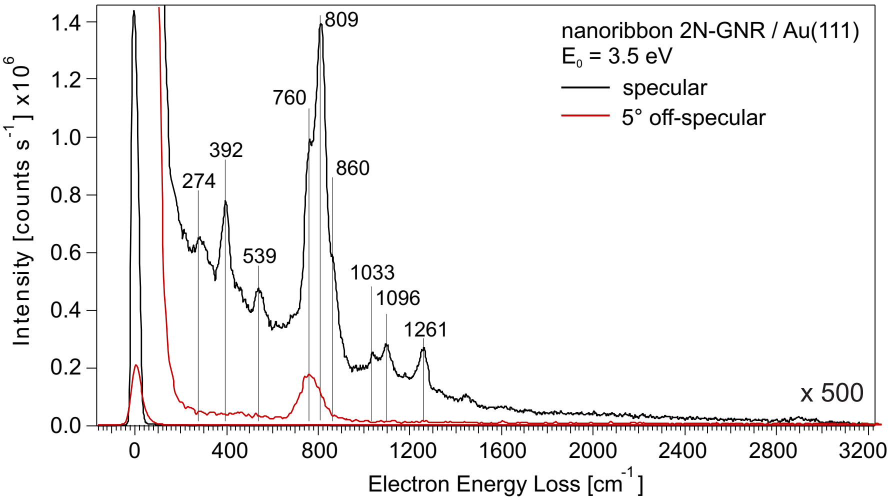

Figure 3.9: Vibrational HREEL spectra measured with a primary electron energy of E_0=3.5 eV in specular (black line) and in 5°-off-specular geometry (red line), respectively of the doubly nitrogen doped precursor 4-4'-(6,11-Dibromo-1,3,4-triphenyltriphenylen-2-yl)pyridine 2N-GNR phase **(3)**on Au(111).

Table 3.3: Assignment of vibrational modes for 4-4'-(6,11-Dibromo-1,3,4-triphenyltriphenylen-2-yl)pyridine GNR phase **(3)** as indicated. All vibrational frequencies are listed in cm^{-1}. IR/Raman data for triphenylene adapted from Ref. [103–105]^{a}. IR/Raman data for benzene adapted from Ref. [105]^{b}. IR data for bromobenzene adapted from Ref. [106, 107]^{c}. IR data for pyridine adapted from Ref. [108]^{d}. ν, indicates stretch; δ, bending; τ, torsion; oop, out-of-plane; ip, in-plane. w, indicates weak; m, medium; s, strong; vs, very strong. A strong dipole activity is indicated by (da).

vibrational mode		**nanoribbon**	**IR data**
δ_{C-C-C}	oop	274w	279/282^{a}
δ_{C-C-C}	oop	392s(da)	380^{c},370^{d}
δ_{C-C-C}	oop	539w	544/550^{a}
δ_{C-H},τ_{C-C}	oop	760vs(da)	688^{b},699/772^{a}
δ_{C-H}	oop	809vs(da)	777/780^{a}
δ_{C-H}	oop	860m(da)	850/851^{a}
δ_{C-H}	ip	1033w	1040^{b},1052/1062^{a},1160^{d}
δ_{C-C}	ip	1096w	1179^{b},1162^{a}
$\nu_{C=C}$	ip	1261w	1298/1318^{a}

In contrast to the pristine GNR and the singly nitrogen doped GNR the HREEL spectrum of the nanoribbon phase shows not only the very intense out-of-plane modes arising from torsion and bending modes from the carbon skeleton but more medium intense losses for example at 392 cm^{-1} originating from out-of-plane modes δ_{C-C-C}. The most striking difference is the occurrence of in-plane, slightly dipole active modes above 1000 cm^{-1} revealing a not perfect planar alignment of the formed nanoribbon phase. Apparently the GNR fabrication process of the double nitrogen doped GNR precursor results in a less qualitative nanoribbon as compared to the pristine GNR and 1N-GNR.

3.2 Electronic Properties

3.2.1 Pristine Graphene nanoribbon

To gain further knowledge of the graphene nanoribbon fabrication process of the precursor GNR and the influence on the electronic structure of the involved phases electronic HREEL spectra were measured in specular geometry with a primary electron energy of $E_0 = 15.5eV$.

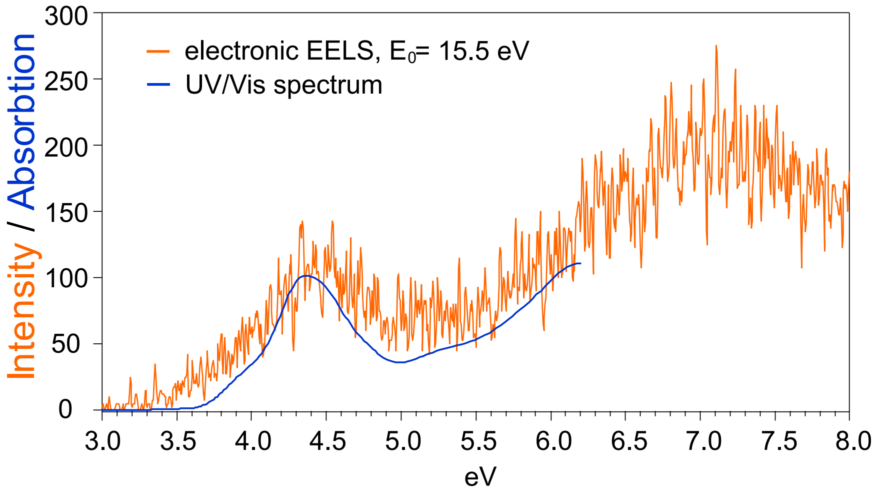

Figure 3.10: Electronic HREEL multilayer spectrum and UV/vis spectrum of the pristine GNR monomer precursor molecule. As previously reported, electronic HREEL measurements with a sufficient high enough primary electron energy (usually $E_0 = 15.5$ eV) are capable of direct electron excitation in molecules thus making HREEL able to examine HOMO-LUMO transitions [102]. The HOMO-LUMO gap derived via UV/vis spectroscopy was found to be 4.41 eV and the electronic transition observed in the HREEL spectrum is located at almost the same position, namely 4.4e eV. It is noteworthy that even for the higher loss energies up to 6.0 eV the UV/vis data perfectly describes and follows the leading edge of the loss spectrum. [101]

The ability to directly probe the optical band gap with the employed HREEL spectrometer was successfully proven earlier [102] for a different type of graphene nanoribbons. Figure 3.10 shows the electronic HREEL spectrum of a multilayer GNR precursor molecules on the Au(111) surface (orange line) and for comparison the UV/vis spectrum of the same compound (blue line) [109]. The UV/vis trace almost perfectly describes the HREEL trace featuring the transition located at 4.4 eV and even for energies above

6 eV the conformity persists. Proving the capability of the experimental setup to very accurate measure electronic transitions as well. The overall resolution measured as the fwhm was better than 9 meV unless otherwise stated this is also true for the singly and doubly nitrogen doped GNR molecules as well.
Figure 3.11 depicts the three different phases namely the precursor monomer in 3.11 a), the polymer, obtained after annealing of the substrate at 540 K in 3.11 b) and the all planar, aromatic nanoribbon received after a heating step at 710 K in 3.11 c). The employed Gaussian fits and their resulting envelopes (solid red lines) are included in the measurement data. The vibrational part of the spectra ranging from the elastic peak up to 1.0 eV is omitted for the sake of clarity since no electronic features are included herein. A list of the observed electronic transitions is shown in Table 3.4. The electronic HREEL spectrum of a multilayer coverage of the monomer in 3.11 a) exhibits two strong electronic transitions located at 4.42 eV and at 7.14 eV, respectively. The feature at 4.42 eV is assigned to the HOMO-LUMO transition of the GNR precursor molecule and fits nicely to UV/vis data revealing a gap of 4.41 eV [109]. The high energy transition found at 7.14 eV originates from an electronic transition from lower lying HOMO to higher lying LUMO. The spectrum of the polymer phase shown in 3.11 b) contains two features located at 2.55 eV and at 7.01 eV. The feature at 2.55 eV is assigned to the HOMO-LUMO transition of the polymer phase. The broad electronic feature located at 7.01 eV originates from an electronic transition from a lower lying HOMO to higher lying LUMO. In the spectrum of the polymer the electronic transitions found for the monomer are often still visible, although shifted in position. This finding was reported earlier for a linear graphene nanoribbon precursor as well [102] and is found even more pronounced for the singly nitrogen doped derivative as well. The found electronic transitions for the monomer and the polymer agree well with previously published UV-vis spectra done in solution. Different 6,11-dibromo-1,4-triphenyl-triphenylene based monomers and polymers having different substituents (aryl and aryl bound higher membered alkane rings) in 2 and 3 position reveal optical band gaps in the range of 4.29 eV (289 nm) up to 4.38 eV (283 nm) for the monomer precursors and for the polymers around 2.9 eV (calculated via the onsets of UV-vis

Table 3.4: Electronic transitions for all fabrication steps of GNR **(1)**. Peak positions are determined via the peak maximum of the employed Gaussian fit.

GNR phase	**electronic transition [eV]**
monomer	4.42 and 7.14
polymer	2.55 and 7.01
nanoribbon	2.80

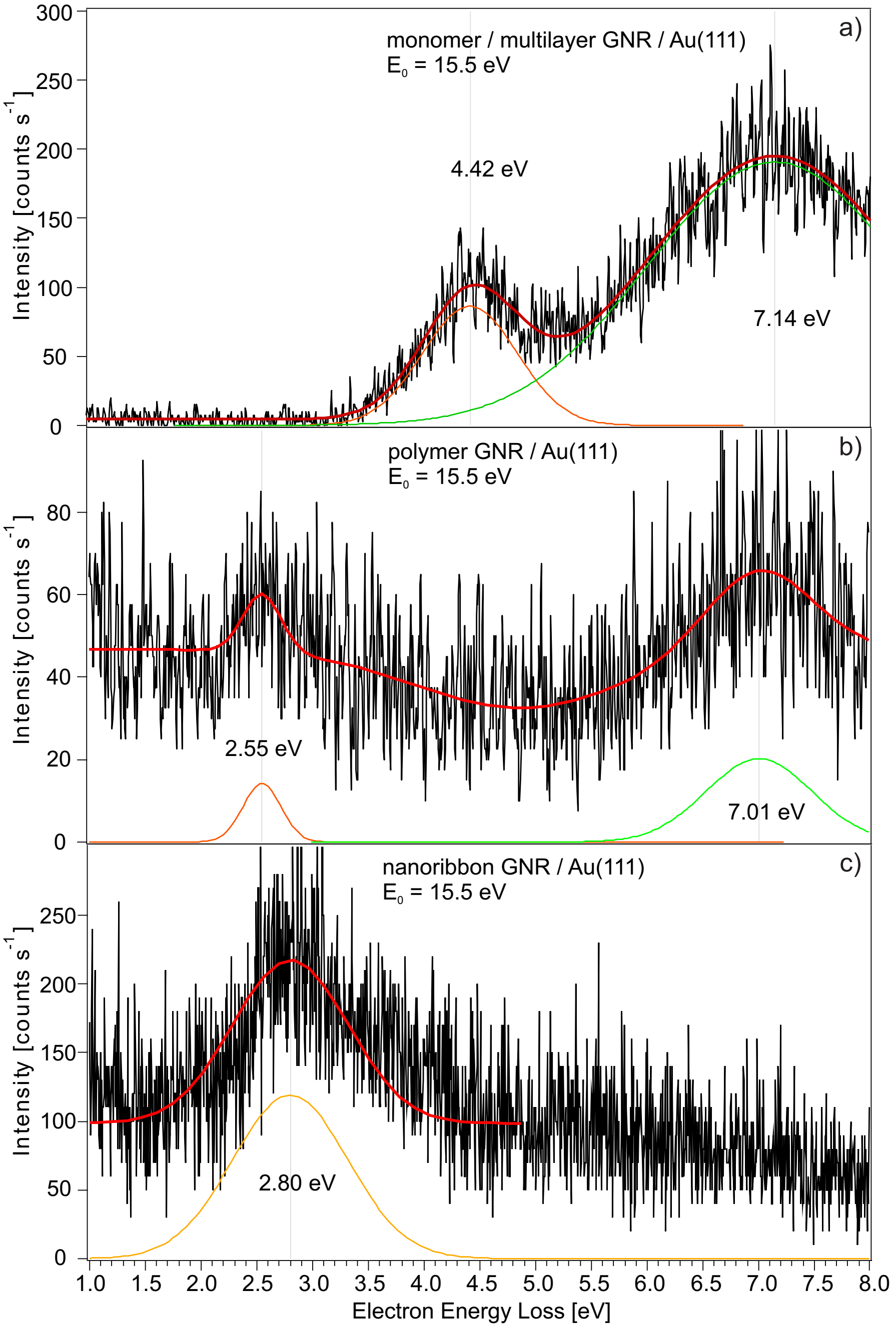

Figure 3.11: Electronic HREEL spectra measured with a primary electron energy of E_0=15.5 eV in specular (solid black line) geometry of the nanoribbon formation steps of the GNR **(1)** precursor upon heating on Au(111). a) precursor monomer, b) polymer phase c) GNR phase **(1)**. The employed Gaussian fits and their resulting envelope (solid red line) is shown as well. The low loss side ranging from the elastic peak at 0 eV up to 1.0 eV (containing vibrational features but no electronic transitions) is left out for clarity.

spectra), respectively [110]. The spectrum of the graphene nanoribbon phase **(1)** depicted in 3.11 c) shows only one electronic transition found at 2.80 eV which is assigned to the HOMO-LUMO excitation.

3.2.2 Singly Nitrogen Doped Graphene Nanoribbon

The electronic HREEL spectra of the bottum up graphene nanoribbon fabrication steps of the 1N-GNR **(2)** precursor molecule are shown in Figure 3.12, namely the multilayer, monomer phase in 3.12 a), the polymer phase annealed at 540 K in 3.12 b) and the graphen nanoribbon phase obtained by annealing at 710 K in 3.12 c). As explained in section 3.2.1 the shown electronic HREEL spectra display only the loss part containing electronic excitation features. All observed electronic transition are summarized in Table 3.5.

The monomer spectrum shown in Figure 3.12 a) exhibits two intense excitation features located at 4.61 eV and at 6.29 eV. The transition at lower loss energies, located at 4.61 eV, is assigned to the HOMO-LUMO transition of the 1N-GNR precursor molecule. The electronic transition at 6.29 eV originates from excitation of lower lying HOMO to higher lying LUMO. In comparison to the pristine GNR the HOMO-LUMO transition of the singly nitrogen doped derivative is shifted by 0,19 eV towards larger gap size. The second electronic feature located at 6.29 eV energies is now found at 0.85 eV lower energy as compared to the pristine GNR. The one nitrogen atom per monomer unit has a drastic influence on the electronic structure of the molecule.

The polymer phase shown in 3.12 b) reveals three features. The first is located at 2.51 eV and is assigned to the HOMO-LUMO transition of the polymer phase. At 4.33 eV and at 6.95 eV weak features apparently originating from the monomer phase are still observed which seems to be common finding for the investigated nanoribbons as well as the previously reported linear GNR [102]. Interestingly, the electronic transitions in the polymer phase match the found transitions of the pristine GNR quite well and deviations of only 0.05 eV are found. In the graphene nanoribbon phase **(2)** shown in 3.12 c), these two features vanish completely and the prior observed HOMO-LUMO transition of the polymer shifts by 300 meV and is now located at 2.81 eV. In comparison to the pristine carbon GNR, the influence of one nitrogen atom per monomer unit has no noticeable effect on the size of the observable HOMO-LUMO band gap.

Table 3.5: Electronic transitions for all synthesis steps of 1N-GNR **(2)**. Peak positions are determined via the peak maximum of the employed Gaussian fit.

1N-GNR phase	**electronic transition [eV]**
monomer	4.61 and 6.29
polymer	2.51, 4.33 and 6.95
nanoribbon	2.81

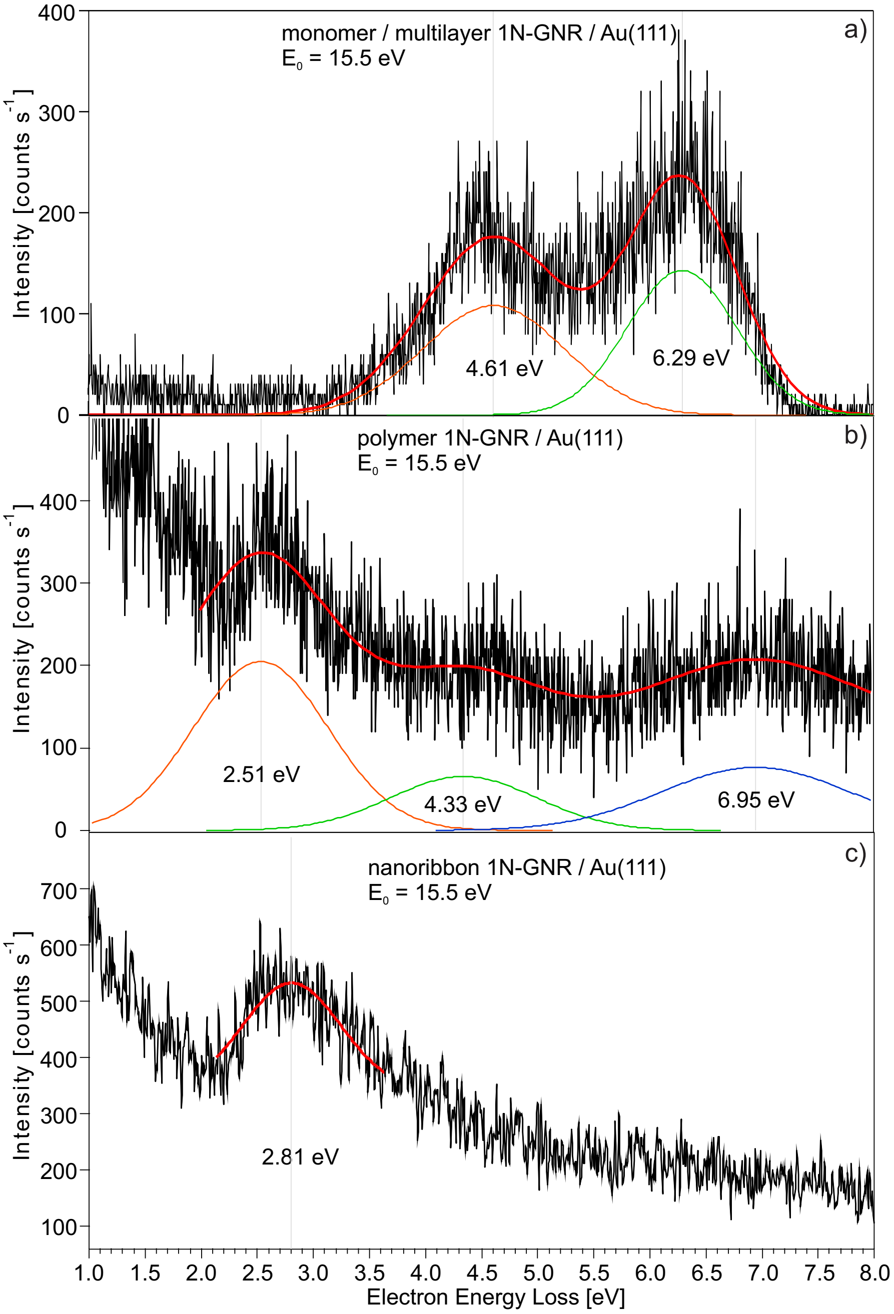

Figure 3.12: Electronic HREEL spectra measured with a primary electron energy of E_0=15.5 eV in specular (solid black line) geometry of the graphene nanoribbon formation steps of the 1N-GNR **(2)** precursor upon heating on Au(111). a) precursor monomer (multilayer), b) polymer phase c) 1N-GNR phase **(2)**. The employed Gaussian fits and their resulting envelope (solid red line) is included as well.

3.2.3 Doubly Nitrogen Doped Graphene Nanoribbon

The electronic HREEL spectrum of the 2N-GNR nanoribbon **(3)** is shown in Figure 3.13. The spectrum was measured with the same parameters (primary electron energy, geometry) and the HREEL spectrum is displayed in the same fashion as in the case of the pristine GNR and the 1N-GNR precursor.

The spectrum exhibits one transition located at 2.70 eV which is assigned to the HOMO-LUMO excitation of **(3)**. The doping of the parent precursor molecule with two nitrogen atoms per monomer unit now exhibits a small shift of 100 meV in the HOMO-LUMO gap size of the resulting graphene nanoribbon phase towards smaller gap size as compared to the pristine carbon based GNR.

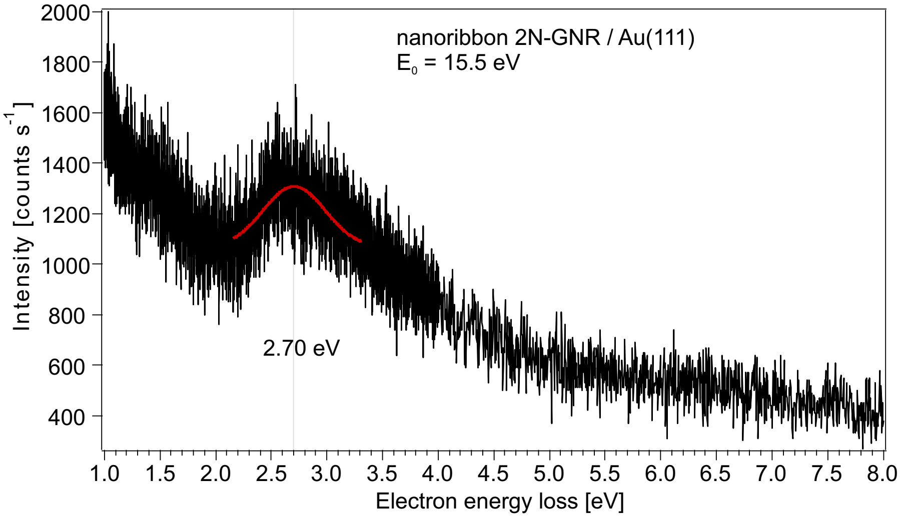

Figure 3.13: Electronic HREEL spectrum measured with a primary electron energy of E_0=15.5 eV in specular (solid black line) geometry of the 2N-GNR nanoribbon **(3)** originating from the 4,4'-(6,11-Dibromo-1,4-diphenyltriphenylene-2,3-diyl)dipyridine precursor on Au(111). The employed Gaussian fit (solid red line) is shown as well. The low loss side ranging from the elastic peak at 0 eV up to 1.0 eV (containing vibrational features but no electronic transitions) is left out for clarity. The spectral resolution (FWHM) for the specular geometry was 7.6 meV.

3.3 Conclusions

The bottom up fabrication processes of graphen nanoribbons starting from the pristine carbon precursor molecule 6,11-dibromo-1,2,3,4-tetraphenyl-triphenylene, the singly nitrogen doped 4-(6,11-Dibromo-1,3,4-triphenyltriphenylen-2-yl)pyridine and the doubly nitrogen doped 4,4'-(6,11-Dibromo-1,4-diphenyltriphenylene-2,3-diyl)dipyridine were investigated by means of TPD, vibrational and electronic HREEL spectroscopy.
Evaporation of a multilayer of each of the precursor molecules on a Au(111) sample followed by annealing steps (desorbing excess molecules) to 540 K and to 710 K lead to the formation of polymer chains and the graphen nanoribbon phase, respectively. The angular-dependent vibrational HREEL spectra of the monomer phase reveal a planar adsorption geometry of the triphenylene core of the molecules while the attached four aromatic six membered rings (benzene or benzene and pyridine in combination) show a strong deviation from the molecular plane due to steric hinderance. A finding that is nicely depicted in the single crystal structure of the monomer 4,4'-(6,11-Dibromo-1,4-diphenyltriphenylene-2,3-diyl)dipyridine determined by X-ray diffraction as shown in Figure A.2 in Appendix A [101]. In the polymer phase this structural motif persists while the deflection angle of the aromatic rings becomes smaller due to the contact with the underlying substrate. The former, rather crowded vibrational spectra gets much less complex after the final annealing step to 710 K when cyclodehydrogenation occurs and only out-of-plane bending modes from C-H and C-C-C remain in the spectra depicting the now overall planar configuration of the achieved graphen nanoribbon phase.
The in specular geometry measured electronic HREEL spectra of the monomers exhibit features originating from the HOMO-LUMO transitions, found in the range from 4.4 to 4.6 eV, and at higher energies ranging from 6.20 eV to 7.14 eV arising from transitions from lower lying HOMO to higher lying LUMO. In the polymer phases these features become less intense and new transitions in the loss energy region of 2.5 eV appear which we assign to the HOMO-LUMO transition of the polymer underlining the successful coupling of the radical species.
The electronic HREEL spectra of each of the different GNR phases **(1)**, **(2)** and **(3)** finally show just one transition, assigned to the HOMO-LUMO excitation. The doping effect on the gap size in the singly nitrogen doped GNR **(2)** is negligible and only in the doubly nitrogen doped GNR **(3)** a shift of the gap of 100 meV towards a smaller gap size is observed. These findings are summarized in Figure 3.15. In addition to the HREELs measurements ultra-violett photoelectron spectroscopy (UPS) experiments were performed by Christopher Bronner in order to elucidate the alignment of the band gap with respect to the electronic structure of the underlying substrate [101]. The result of the UPS and HREELs measurements is summarized in Figure 3.14. The band gap is

shifted relative to the electronic structure of the gold substrate but its size is retained, a finding that is not unexpected for nitrogen atoms located at the edges of armchair graphene nanoribbons [88]. The found positions of the valence and conductance bands and therefore the width of the band gap agrees very well with other data for the pristine GNR [111].

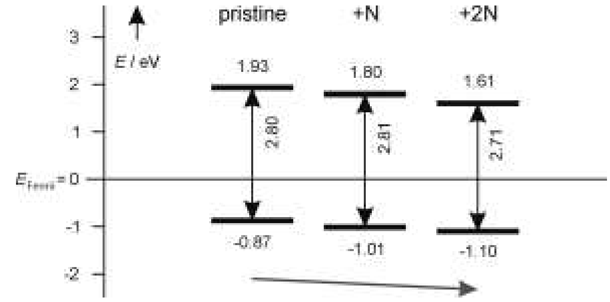

Figure 3.14: Summary of the band gap size and the alignment relative to the Fermi level of the Au(111) substrate derived by UPS and electronic HREEL spectra of the pristine GNR **(1)**, the 1N-GNR **(2)** and the 2N-GNR nanoribbon **(3)** adapted from Reference [101]. Although the size of the band gap remains nearly unaffected, the complete band structure shifts towards lower energies.

An overview of the electronic HREEL spectra of the involved molecular phases during the GNR build up, combined in one figure for clarity, is shown in Figure A.3 in Appendix A.

In conclusion it can be stated that the bottom up fabrication process for graphene nanoribbons is feasible with the chosen precursor molecules and yields precise GNR. HREEL spectroscopy is an ideal tool to observe changes in adsorption and electronic properties of molecules on surfaces and is in particular able to directly measure the HOMO-LUMO band gap of organic molecules evaporated on metal substrates. The direct doping of the molecular precursors used for the bottom up fabrication process furthermore offers a defined site selection of the in this case nitrogen atoms yielding defect free GNRs. The results of this chapter are published in Angew. Chem. Int. Ed. **2013**, 52, 44224425.

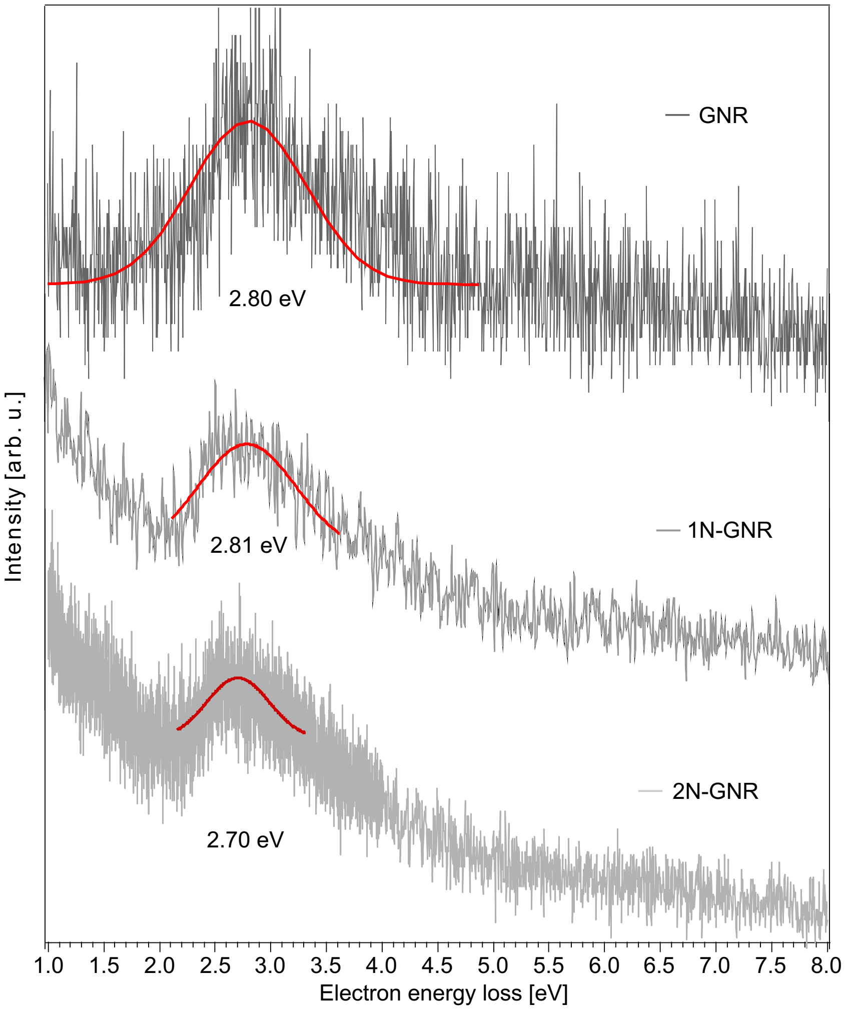

Figure 3.15: Overview of all measured GNR phases. Electronic HREEL spectra measured with a primary electron energy of E_0=15.5 eV in specular geometry of the pristine GNR **(1)** (solid dark grey line), the 1N-GNR **(2)** (solid grey line) and the 2N-GNR nanoribbon **(3)** (light grey line). The employed fits (solid red lines) are shown as well. The low loss side ranging from the elastic peak at 0 eV up to 1.0 eV (containing vibrational features but no electronic transitions) is not shown for clarity reasons.

Chapter 4

Tetraazaperopyrene and its derivatives on Au(111)

In the context of organic electronics which are already in daily use like in photovoltaic cells, light-emitting diodes, thin-film transistors the normally employed π-conjugated aromatic carbon based semiconducting molecules and their interaction with metal substrates play the crucial role [1–18, 112–115]. These semiconductors can be divided into n-and p-type called semiconductors. Whereas n-type (from the negative charge of the excess electron) denotes semiconductors that possess a larger electron concentration than hole concentration and that electrons are the majority carriers. N-type semiconductors are created by adding group V (like phosphorous) elements to a group IV semiconductor (carbon based). The p-type (from positive charge of the hole) semiconductors have a larger hole concentration than electron concentration thus making the holes the majority carriers. P-type semiconductors are generated via doping of a group IV semiconductor with group III elements like boron. The known amount of usable p-type molecular semiconductors so far are still considerably larger than for the n-type ones [16, 24–28]. Nonetheless the need for new n-type materials, matching the immense requirements, still persists when the planned application involves mixed p/n-type junctions [1–18, 112–117]. The adjustment of the properties of the used molecules to meet the desired specifications like good air stability, charge-carrier capabilities and electron injection capability remains a challenge. These goals can be achieved via the introduction of electron withdrawing (fluorinated side chains, halogens in core positions) groups leading to a lowering of the energy of the LUMO and by subsequent substitution of carbon with heteroatoms like nitrogen [17, 18, 114, 118–129].

A very promising candidate in this field of interest is the molecular class of the chromophor 1,3,8,10-Tetraazaperopyrenes, see Figure 4.1. Possessing a mainly carbon based, aromatic system containing of condensed benzene and pyrimidine. During synthesis, different electron withdrawing groups to alter the molecules properties can readily be introduced either at the pyrimidine carbon atom (neighbored by two nitrogen atoms) or at the benzene core of the TAPP respectively, see Ref. [130] for more details. The unsubstituted TAPP molecule and the two other derivatives discussed in this work were synthesized by Prof. Gade et al. at the University Heidelberg which we gratefully acknowledge.

The assignment of the observed vibrational modes derived from HREELS measurement presented in section 4.1 were done employing DFT calculations using B3LYP with basis set 6-31G. For further details see section 2.1.4 in the Experimental Details. DFT calculations were performed by Friedrich Maaß using ORCA 2.9.1 [61]. For details concerning the sample preparations and dosage parameters for each of the discussed TAPP derivatives see section 2.1.3 in the Experimental Details.

In this chapter we will show and discuss the findings of the vibrational and electronic HREELS measurements with regard to adsorption behavior and the electronic properties of 1,3,8,10-Tetraazaperopyren (TAPP) and its derivates 2,9-bisperfluoropropyl-1,3,8,10-tetraazapero- pyren (TAPP-$(C_3F_7)_2$) and the halogenated species 2,9-bisperfluoropropyl-4,7,11,14-tetra-chloro-1,3,8,10-tetraazaperopyren (TAPP-Cl_4-$(C_3F_7)_2$).

Note added: After release of this thesis it was found out that the electronic EEL measurements were influenced by a spectrometer error and that the obtained electronic transitions presented here should be interpreted carefully with this knowledge.

4.1 Adsorption Geometry

4.1.1 TAPP

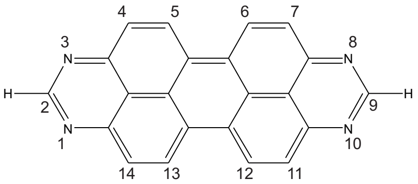

Figure 4.1: Unsubstituted TAPP molecule.

The pristine 1,3,8,10-Tetraazaperopyrene molecule, structure shown in Figure 4.1, is the basis of a wide variety of differently substituted TAPPs. At the positions 2 and 9 side chains containing just alkanes or fluorinated alkanes can easily be introduced, just slightly altering the electronic structure of the molecule. The 4, 7, 11 and 14 positions can be exchanged by different substituents; e.g. halogens. Substitution at the mentioned positions

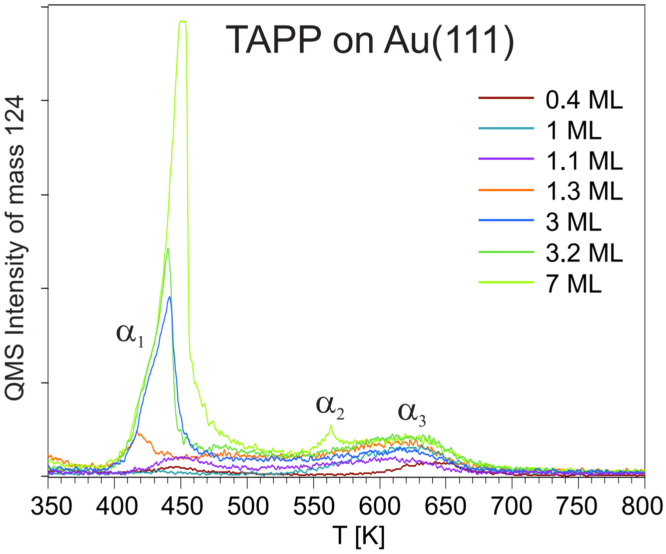

Figure 4.2: TPD spectra for different TAPP coverages as indicated. The observed mass fragment m = 124 is assigned to $[C_{10}H_4]^+$, the heating rate was β = 1K s^{-1}. α_1 depicts the multilayer, α_2 a compressed phase and α_3 the monolayer.

have a drastic influence on the molecule electronic structure e.g. changing the HOMO-LUMO gap size [131]. To gain insights in the adsorption behavior of TAPP on Au(111) and to be able to determine initial coverages, TPD measurements ranging from the sub-monolayer up to the multilayer regime were measured as shown in Figure 4.2. The observed mass of 124 amu was assigned to the $[C_{10}H_4]^+$ fragment. The spectrum contains 3 peaks. The fact that the intensity of peak α_1 rises infinite with increasing coverage and that the maximum desorption temperature shifts to higher temperatures is typically for a zero-order desorption process. This feature is therefore assigned to the TAPP multilayer. Peak α_2 is part of the monolayer and represents a compressed phase. The feature labeled α_3 is assigned to the monolayer of TAPP. It is noteworthy, that no full saturation of the monolayer peak is observed as would be expected. This can be explained by the fact, that the TPD does not show the full desorption of an intact molecule. In such cases coverage determination via the integration of TPD curves is not feasible and a different method is chosen. The parameters, influencing the growth rate can be precisely controlled (such as evaporation temperature and dosage time, partial pressure of the evaporated sample inside of the preparation chamber, substrate temperature and the distance between the evaporator and the substrate). In order to define a full monolayer a consecutive series of TPD spectra were recorded starting from different initial coverages. The complete monolayer regime is reached (peak around 600 K) when further molecules are adsorbed and the multilayer peak (around 450 K) evolves. The needed dosage time for 1 full monolayer (1 ML/dosage time) makes further coverage determination feasible when the dosage parameter mentioned above are kept constant and under the assumption that layer growth follows a linear dependency.

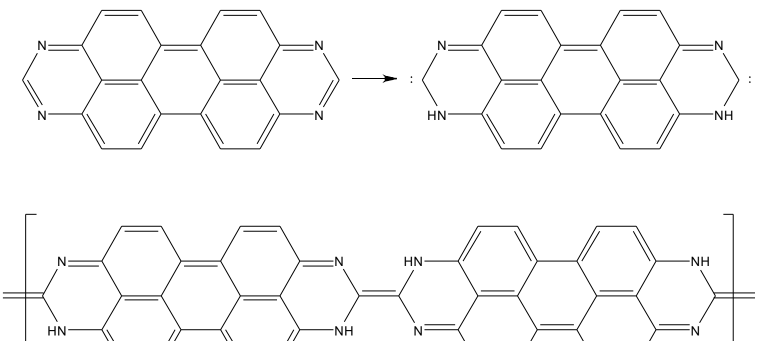

Figure 4.3: Structure model of TAPP molecules showing the polymerization via activated carbene species.

A HREEL spectrum taken after a TPD measurement reaching 800 K proves that molecular fragments are still found at the surface (see Appendix B, Figure B.1). For a better understanding of the adsorption properties of TAPP on Au(111) we performed angular dependent HREELS measurements with a primary electron energy of $E_0 = 3.5$ eV. Figure 4.4 shows the in specular and 8°-off-specular measured spectra of a 1 ML a), a 1 ML annealed (550 K) b) and a 3 ML c) coverage TAPP on Au(111). The 1 ML spectrum seen in Figure 4.4 a) is dominated by 4 intense vibrational losses at 449cm^{-1}, 488cm^{-1}, 778cm^{-1} and 827cm^{-1} respectively. In case of the first two peaks arising from strong out-of-plane bending of δ_{C-C-C}, $\delta_{C-C=C}$ and torsion mode of τ_{CCC}. The latter two arising from out-of-plane bending modes of δ_{C-H} and δ_{CCC}. Close to the elastic peak, the buckling modes along the short and long molecular axis appear at 178cm^{-1} and 229cm^{-1}. The observed modes show a strong dipole activity, suggesting a planar adsorption geometry of the molecules with respect to the Au(111) substrate. For a more detailed assignment of the observed vibrational losses see Table 4.1. From literature it is known that on Cu(111) pristine TAPP molecules are capable to form polymers due to activated carbene species via tautomerization at the N=CH-N, see Figure 4.3 for details. This was successfully utilized on Cu(111) by Gade et al. via heating of the substrate [132]. Stabilized via copper atoms the polymers are clearly visible in scanning

Table 4.1: Assignment of vibrational modes for 1 ML, 1 ML annealed to 550 K and 3 ML 1,3,8,10-Tetraazaperopyren on Au(111). All vibrational frequencies are given in cm^{-1}. Calculation employed B3LYP with basis set 6-31G using ORCA 2.9.1 [61]. ν, indicates stretch; δ, bending; τ, torsion; oop, out-of-plane; ip, in-plane. w, indicates weak; m, medium; s, strong; vs, very strong. A strong dipole activity is indicated by (da).

vibrational mode		**1 ML**	**1 ML 550 K**	**3 ML**	**calc. data**
buckling, long axis	oop	178w	178w	179m	176
buckling, short axis	oop	229w	229w	241m	239
δ_{C-C-C}, $\delta_{C-C=C}$	oop	449s(da)	459s(da)	–	–
τ_{CCC}	oop	488s(da)	507vs(da)	505vs(da)	504
$\delta_{C=C-C}$, δ_{C-C-C}	oop	–	–	664w	–
δ_{C-H}	oop	778s(da)	801vs(da)	796vs(da)	814
δ_{C-H}, δ_{CCC}	oop	827vs(da)	843vs(da)	851vs(da)	880
δ_{C-H}	oop	927m	946m	–	–
ν_{C-H}	ip	–	–	3056w	3156

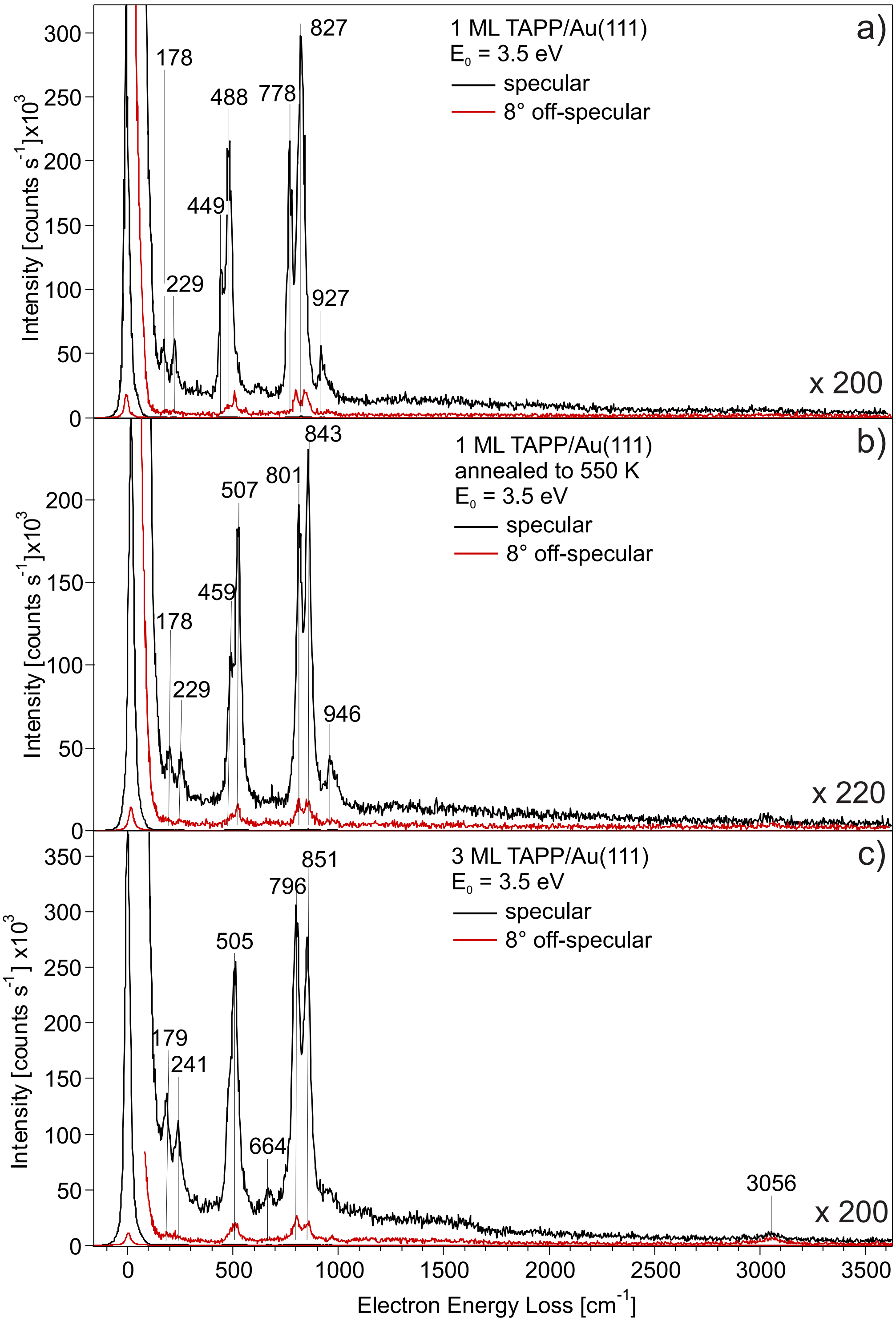

Figure 4.4: Vibrational HREEL spectra measured with a primary electron energy of E_0=3.5 eV in specular (solid black line) and in 8°-off-specular geometry (solid red line) respectively of 1 ML a) 1 ML annealed to 550 K b) and 3 ML c) coverage of TAPP on Au(111). The resolution (FWHM) for the specular geometry was 25 *cm*$^{-1}$ (3 meV) and for the off-specular 30 *cm*$^{-1}$ (3.5 meV).

tunneling microscopy (STM). Although the copper atoms can not be seen in STM, density functional theory (DFT studies strongly emphasise their existence. Keeping these findings in mind we investigated the behavior of an to 550 K annealed monolayer TAPP to see if any evidence can be found for the polymerization process. Figure 4.4 b) shows the specular and 8°-off-specular measured spectra of a monolayer coverage TAPP annealed to 550 K. In this temperature region desorption can be neglected since monolayer desorption starts at around 570 K as seen in Figure 4.2, and polymerization should occur. In comparison to Figure 4.4 a) it is obviously that no new vibrational features appear in the spectrum at first sight. But there is a noticeable difference. Nearly all of the observed losses are shifted by around $20 cm^{-1}$ towards higher wavenumbers. The fact that a blue shift (higher wavenumber or higher energy) of the observed modes occur can not exclusively be explained be the formation of a polymeric chain especially since the buckling modes of the whole molecule along its short and long axis exhibit no shift at all. Furthermore in the polymeric chains as depicted in Figure 4.3 due to the rearrangement the nitrogen atoms are partially bond to hydrogen and one would expect to see a nitrogen hydrogen wagging out-of-plane vibration in the spectral region around 730 cm^{-1}, typically for secondary amines, which is not the case. Instead it seems more likely that the observed shift originates from an gold adatom complex species, probably partly charged (e.g. due to deprotonation or electron attachment or charge separation upon complexation). Considering the fact, that on a Cu(111) surface the copper atoms tend to stabilize the molecular frameworks on the surface by complex formation via the N atoms of TAPP, a similar effect on Au(111) can not be ruled out [132]. This finding will be more detailed addressed in the electronic properties section of TAPP. The higher coverage regime HREEL spectra for 3 ML TAPP is shown in Figure 4.4 c). The spectrum still consists of the out-of-plane modes one can already observe in the one ML phase. Nevertheless minor changes in the molecular orientation with respect to the surface can be seen. The region for in-plane modes (above $1000 cm^{-1}$) is more pronounced and the in-plane, symmetric stretch vibration ν_{C-H} shows up at $3056 cm^{-1}$. All this points to a slightly increased roughness of the molecular layer to layer growth for higher coverages.

4.1.2 2,9-Bisperfluoro-Propyl-1,3,8,10-Tetraazaperopyren

The structure of the TAPP derivative with fluorinated propylene side chains in 2 and 9 position is shown in Figure 4.5. Substitution in these places has only a minor effect on the overall electronic structure of the molecule [131]. The planar backbone of the molecule still persists although a more complex adsorption behavior due to the bulky fluorinated side chains can be expected. For a better understanding of the adsorption behavior of TAPP(C_3F_7)$_2$ on Au(111) different amounts of molecules were evaporated on the substrate followed by TPD measurements. Figure 4.6 shows the result, a coverage dependent TPD series monitoring the mass 69 amu which is assigned to the $[CF_3]^+$ fragment. The spectrum contains three peaks (α_1, α_2 and α_3. The intensity of peak α_1 rises infinite with increasing coverage and the maximum desorption temperature shifts to higher temperature. This is typically for a zero order desorption process, we assign this peak to arise from the multilayer. When increasing the coverage one peak (α_1) at higher desorption temperatures (ranging from 600 K to 750 K) evolves. At a certain point it saturates and its intensity no longer increases with increasing coverage and we assign this feature to the monolayer since the observed behavior is typically for monolayer desorption. Close to the saturation a second peak (α_2) at the low temperature shoulder of α_1 is observed. It still belongs to the monolayer but represents so called compressed phase aggregates or special binding sites of molecules on the surfaces [133, 134]. The chosen fragment for the TPD measurements (CF_3^+) originates from bond breakage inside of the fluorinated, propylene side chains. When observing such fragments one should keep in mind that the TPD does not necessarily represent the full desorption of an intact molecule. The multilayer desorbs intact due to not sufficiently high enough temperatures for carbon-carbon bond dissipation which are usually in the range from 400-550°C in contrast to the monolayer with contact to the substrate [135, 136]. A vibrational HREEL spectrum taken after a TPD measurement reaching 800 K proves that molecular fragments are still found at the surface. (see Appendix B, Figure B.2).

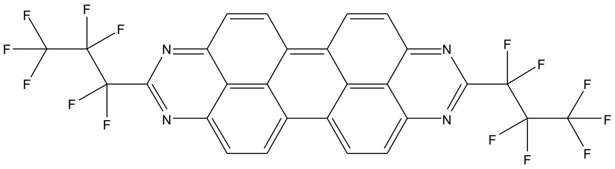

Figure 4.5: Structure of TAPP(C_3F_7)$_2$.

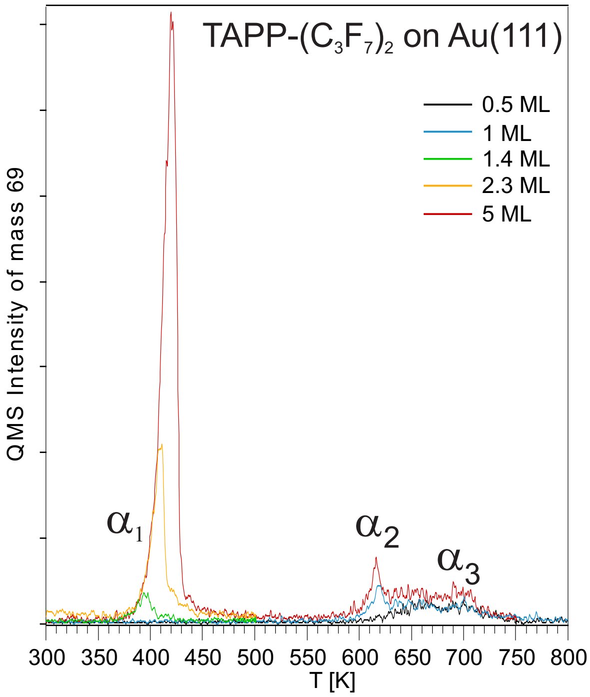

Figure 4.6: TPD spectra for different TAPP-$(C_3F_7)_2$ coverages as indicated. Observed mass fragment m = 69 is assigned to $[CF_3]^+$, the heating rate was $\beta = 1\mathrm{K}\ s^{-1}$. α_3 depicts the multilayer, α_2 a compressed phase of the monolayer regime and α_3 the monolayer.

In Figure 4.7 HREEL spectra of a one ML a) and a 6 ML b) coverage of TAPP-$(C_3F_7)_2$ is shown, measured in specular and 8°-off-specular geometry, respectively. As expected the spectrum is more complex than the one of the pristine TAPP molecule. In the 1 ML spectra seen in Figure 4.7 a) the buckling modes in which the whole molecule bends along its long and short axis respectively are found at $190cm^{-1}$, $255cm^{-1}$ and $396cm^{-1}$. The fluorinated propylene side chains make up a large part in the observed spectrum, namely δ_{F-C-F} at $461cm^{-1}$ and $523cm^{-1}$. It should be mentioned that δ_{C-C-C} bending contributes as well in this region of the loss spectrum. The intense, dipole active mode at $734cm^{-1}$ is assigned to the bending mode $\delta_{F_3C-CF_2-CF_2}$. Intense, out-of-plane vibrations of the CH bending can be found at $851cm^{-1}$ and $976cm^{-1}$, these modes exhibit a strong dipole activity. More characteristic vibrational features of the fluorinated species are found at $1222cm^{-1}$, $1265cm^{-1}$ and $1354cm^{-1}$ which are assigned to dipole active, stretching modes of $\nu_{F_2C-CF_2}$, $\nu_{F_2C-CF_2}$ and $\nu_{N_2C-CF_2asym}$ respectively. The appearance of dipole active out-of-plane modes leads to the conclusion, that the

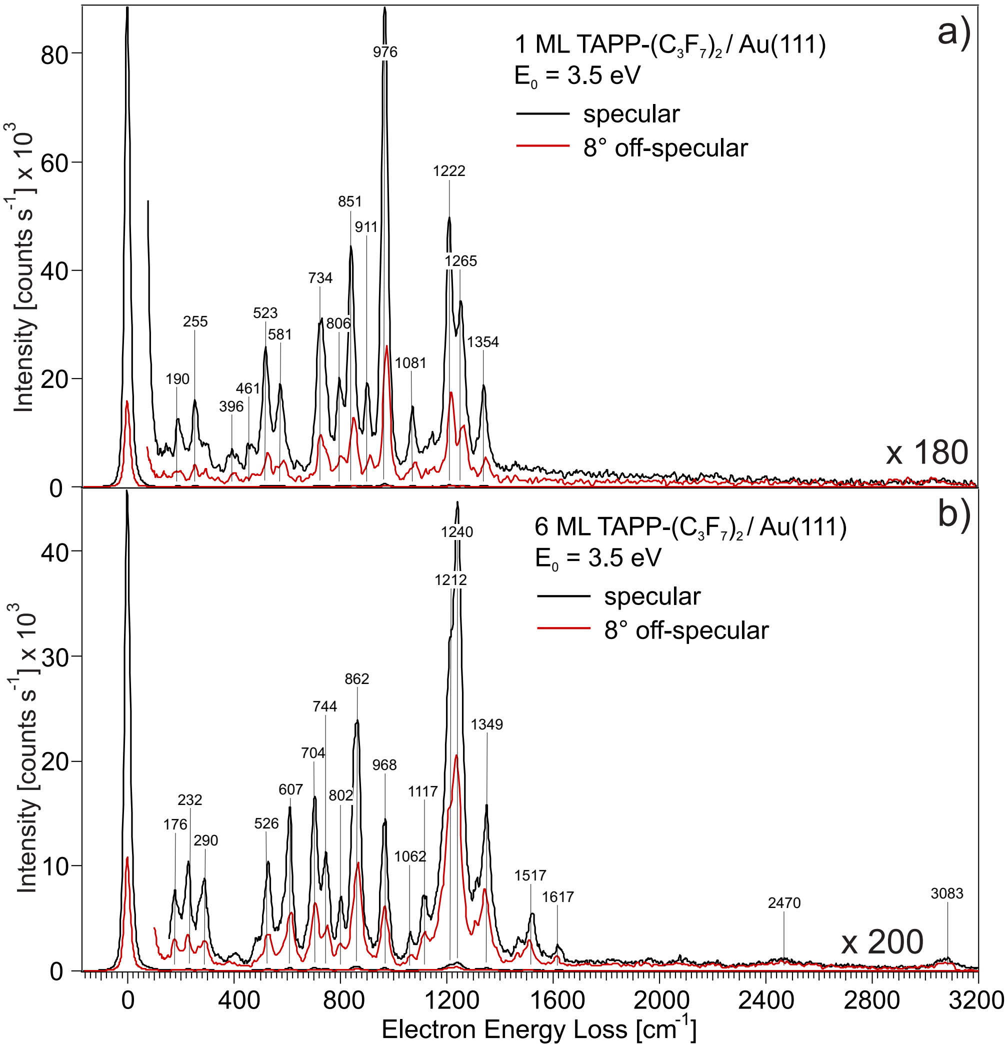

Figure 4.7: Vibrational HREEL spectra of a 1 ML a) and a 6 ML b) coverage of TAPP-(C_3F_7)$_2$ on Au(111). The spectral resolution (FWHM) for the specular geometry was 22 cm^{-1} (2.8 meV) and for the off-specular 30 cm^{-1} (3.2 meV).

molecules adsorb in a predominantly planar fashion with respect to the substrate. The propyl side chains seem to be in a cis like orientation on the surface, pointing upwards, in contrast to the crystal structure where a trans like geometry is favoured [131]. This finding can easily be explained by the steric hinderance on the Au(111) surface that hinders alternatively orientations. For a more detailed assignment of the observed vibrational losses see Table 4.2.

Figure 4.7 b) shows the in specular and 8°-off-specular measured HREEL spectra of a 6 ML coverage. The overall appearance of the spectrum has changed compared to the monolayer spectrum as expected. The dipole active, out-of-plane modes originating from the fluorinated propyl side chains at 1212cm^{-1}, 1240cm^{-1} and 1349cm^{-1} assigned to $\nu_{F_2C-CF_2}$, $\nu_{F_2C-CF_2}$ and $\nu_{N_2C-CF_2asym}$ respectively now dominate the spectrum. Whereas the out-of-plane bending modes originating from δ_{C-H} at 802cm^{-1}, 862cm^{-1} and 968cm^{-1} appear less intense in the spectrum. At 1517cm^{-1} and 1617cm^{-1} in-plane bending modes of δ_{C-C-H} show up in the spectrum. At 3083cm^{-1} the stretching modes of ν_{C-H} appear containing no noticeable dipole activity. These findings strongly

Table 4.2: Assignment of vibrational modes for 1 ML and 6 ML 2,9-bisperfluoro-propyl-1,3,8,10-tetraazaperopyren on Au(111). All vibrational frequencies are given in cm^{-1}. Calculation employed B3LYP with basis set 6-31G using ORCA 2.9.1 [61]. ν, indicates stretch; τ, torsion; δ, bending; oop, out-of-plane; ip, in-plane. w, indicates weak; m, medium; s, strong; vs, very strong. A strong dipole activity is indicated by (da).

vibrational mode		**1 ML**	**6 ML**	**calc. data**
buckling long axis	oop	190m	176m	187
buckling short axis	oop	255m	232m	271 - 286
buckling short axis	oop	–	290m	271 - 286
buckling short axis	oop	396w	–	384
$\delta_{C-C-Csym}$, δ_{F-C-F}	ip	461w	–	493
$\delta_{C-C-Casym}$, δ_{F-C-F}	ip	523m(da)	526m(da)	516
τ_{C-C-C}	oop	581m(da)	607m(da)	607
$\delta_{F_3C-CF_2-CF_2}$	ip	–	704s(da)	–
$\delta_{F_3C-CF_2-CF_2}$	ip	734m(da)	744m	689
δ_{C-H}	oop	806w	802w	–
$\delta_{C-Hasym}$	oop	851s(da)	862s(da)	864
δ_{C-Hsym}	oop	911m	–	881
δ_{C-H}	oop	976vs(da)	968m(da)	1019
δ_{C-H}	oop	1081m	1062w	1033
$\delta_{F_3C-CF_2-CF_2}$	ip	1120w	1117w	1107
$\nu_{F_2C-CF_2}$	oop	1222s(da)	1212vs(da)	1219
$\nu_{F_2C-CF_2}$	oop	1265s(da)	1240vs(da)	1250
$\nu_{N_2C-CF_2asym}$	oop	1354m(da)	1349s	1313
δ_{C-C-H}	ip	–	1517w	1561
δ_{C-C-H}	ip	–	1617w	1674
H-bridge	ip	–	2470w	–
ν_{C-H}	ip	–	3083w	3254

suggest a slightly tilted adsorption geometry along the short axis of the molecules for higher coverages e.g. the adaption of the trans configuration which is also found in the bulk crystal structure [131]. A tilt along the long axis would result in the appearance of dipole active intense modes in particularly arising from ν_{C-H} among other in-plane modes. The appearance of not dipole active in-plane modes can be explained by the fact that in the 6 ML coverage regime the molecular vibrational modes are less influenced by the image potential forming in the underlying substrate thus the surface selection rule begins to break down. Similar findings employing HREEL experiments are found by Tautz et al. even for smaller coverages and underpin this explanation [137].

4.1.3 2,9-Bisperfluoro-Propyl-4,7,11,14-Tetrachloro-1,3,8,10-Tetraazaperopyren

The structure of the TAPP derivate containing fluorinated propylene side chains in 2 and 9 position and 4 chloro substituents in the 4,7,11,14 position is shown in Figure 4.8. The substitution in the core position of the molecule now results in a noticeable change in the electronic properties of the molecule [131]. The TAPP backbone remains planar but as already seen for the TAPP-$(C_3F_7)_2$ derivative a more complex adsorption behavior at least for higher coverages can be expected.

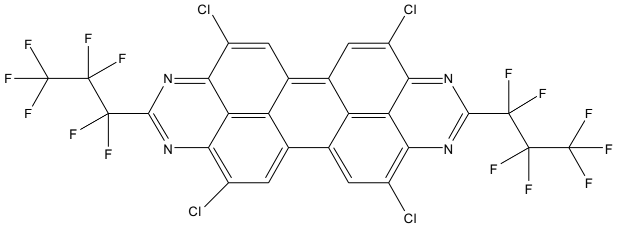

Figure 4.8: Structure of TAPP-Cl_4-$(C_3F_7)_2$.

Figure 4.9 shows a TPD series for different initial coverages of TAPP-Cl_4-$(C_3F_7)_2$ on

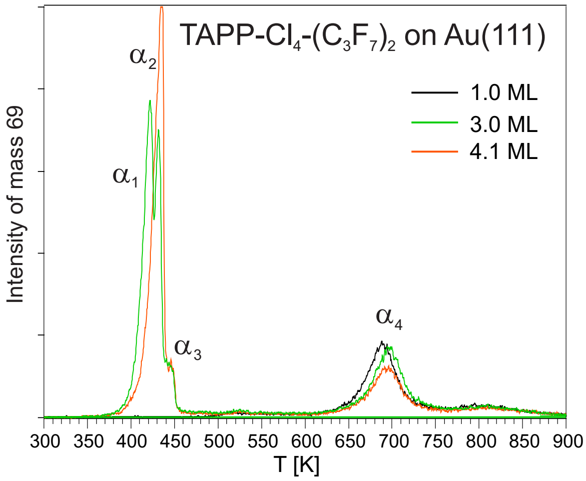

Figure 4.9: TPD spectra for different TAPP-Cl_4-$(C_3F_7)_2$ coverages as indicated. Observed mass fragment m = 69 is assigned to $[CF_3]^+$, the heating rate was $\beta = 1K\ s^{-1}$. α_1 and α_2 depict the multilayer, α_3 the second layer and α_4 the monolayer.

the Au(111) substrate. The observed mass is assigned to the $[CF_3]^+$ fragment. The spectrum shows four distinct peaks. At low desorption temperatures (around 400 K), the peak α_2 is assigned to the multilayer since its intensity grows infinitely with increasing coverage. It can be seen, that the multilayer trace for the 3 ML coverage does

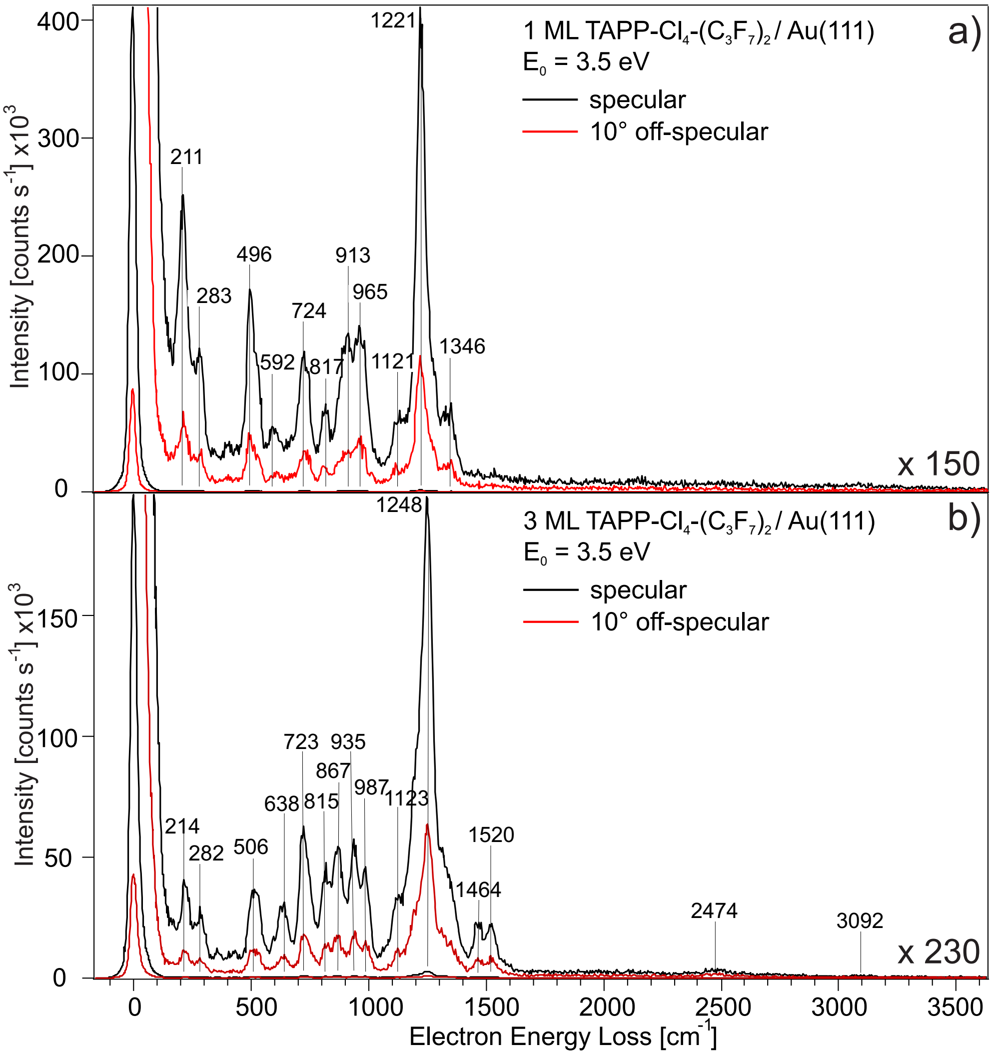

Figure 4.10: Vibrational HREEL spectra of 1 ML a) and 3 ML b) TAPP-Cl$_4$-(C$_3$F$_7$)$_2$ on Au(111). The resolution (FWHM) for the specular geometry was 23 cm^{-1} (2.9 meV) and for the off-specular 26 cm^{-1} (3.4 meV).

not only exhibit one peak, but a second one denoted α_1. Multilayer TPD traces showing more than one distinct peak can be explained by a tower like growing mode. The two-peak shape of the 3.0 ML coverage TPD spectrum was hardly reproducible. The peak α_3 originates from the second layer on-top of the first monolayer, its area is less than one complete layer. The intensity of peak α_4 saturates upon increasing dosage and is therefore assigned to the monolayer coverage. The rather weak and broad signal ranging from 750 K to almost 900 K originates from sample holder surfaces which contribute to desorption signal at this elevated temperatures. It is noteworthy that the molecule in the monolayer regime does not desorb intact from the surface upon heating. A vibrational HREEL spectrum taken after a TPD measurement reaching 900 K proves that molecule fragments from the aromatic core are still found at the surface. (see Appendix B, Figure B.3).

In Figure 4.10 the in specular and 10°-off-specular geometry measured HREEL spectra of 1 ML a) and 3 ML b) TAPP-Cl_4-$(C_3F_7)_2$ are shown. In the 1 ML coverage regime the most intense, dipole active mode at $1221 cm^{-1}$ arises from the fluorinated propyl chains namely $\nu_{F_3C-CF_2}$. The former very intense out-of-plane modes originating from δ_{C-H} bending now only play a minor role in the spectrum which is due to their comparable low occurrence in the tetrachlorinated species. The strong out-of-plane buckling mode of the molecular backbone shows up at $211 cm^{-1}$. The strong feature at $496 cm^{-1}$ is assigned to bending modes of δ_{F-C-F}. At $592 cm^{-1}$ and $724 cm^{-1}$ out-of-plane bending modes assigned to δ_{C-C-C} appear. At $913 cm^{-1}$ and $965 cm^{-1}$ the dipole active bending modes assigned to $\delta_{FC-FC-CN}$ appear. These results confirm the mostly planar adsorption of the molecule with respect to the surface. In the monolayer regime the fluorinated propyl chains are orientated in a cis like fashion (like it was already found for the not chlorinated TAPP$(C_3F_7)_2$ species) as compared to the bulk structure since due to steric hinderance the trans orientation is not feasible. For a detailed assignment of the observed vibrational losses see Table 4.3. The HREEL spectra of the 3 ML TAPP-Cl_4-$(C_3F_7)_2$ coverage is shown in Figure 4.10 b). The strongest, observed mode at $1248 cm^{-1}$ is assigned to out-of-plane stretching of $\nu_{F_3C-CF_2}$ and exhibits a strong dipole activity. The backbone buckling mode can be found at $214 cm^{-1}$. At $282 cm^{-1}$ a bending mode assigned to δ_{F-C-C} shows up. The feature at $638 cm^{-1}$ originates from the in-plane bending mode of δ_{C-C-C}. Out-of-plane bending modes arising from δ_{C-C-C} appear at $723 cm^{-1}$ and at $815 cm^{-1}$ the torsion mode assigned to τ_{C-C-C} appear. The features at $867 cm^{-1}$, $935 cm^{-1}$ and $987 cm^{-1}$ are assigned to δ_{C-H}, $\delta_{FC-FC-CN}$ and $\delta_{FC-FC-CN}$ respectively. New vibrational modes, as compared to the 1 ML TAPP-Cl_4-$(C_3F_7)_2$ coverage, found at $1464 cm^{-1}$ and $1520 cm^{-1}$ are assigned to the in plane modes $\nu_{CN-Casym}$ and $\nu_{Cl-C-Casym}$ respectively. At $3092 cm^{-1}$ a very weak feature originating from in plane ν_{C-H} can be seen. In conclusion it can be stated, that in the higher

Table 4.3: Assignment of vibrational modes for 1 ML and 3 ML 2,9-bisperfluoropropyl-4,7,11,14-tetrachloro-1,3,8,10-tetraazaperopyren on Au(111). All vibrational frequencies are given in cm^{-1}. Calculation employed B3LYP with basis set 6-31G using ORCA 2.9.1 [61]. ν, indicates stretch; τ, torsion; δ, bending; oop, out-of-plane; ip, in-plane. w, indicates weak; m, medium; s, strong; vs, very strong. A strong dipole activity is indicated by (da).

vibrational mode		**1 ML**	**3 ML**	**calc. data**
$\tau_{F_2C-C}buckling$	oop	211s(da)	214m(da)	213
δ_{F-C-C}	oop	283m(da)	282m(da)	265
δ_{F-C-F}	ip	496s(da)	506m(da)	466
δ_{C-C-C}	oop	592w	–	607
δ_{C-C-C}	ip	–	638m	609
δ_{C-C-C}	oop	724m(da)	723s(da)	720
τ_{C-C-C}	oop	817w	815m	823
δ_{C-H}	oop	–	867s(da)	874
$\delta_{FC-FC-CN}$	oop	913m(da)	–	901
$\delta_{FC-FC-CN}$	ip	–	935s(da)	934
$\delta_{FC-FC-CN}$	ip	965m(da)	987m(da)	944
ν_{F-C}	ip	1121w	1223m	1107
$\nu_{F_3C-CF_2}$	oop	1221vs(da)	1248vs(da)	1235
$\nu_{F_2C-CN_2}$	oop	1346m	–	1325
$\nu_{CN-Casym}$	ip	–	1464m(da)	1482
$\nu_{Cl-C-Casym}$	ip	–	1520m(da)	1545
H-bridge	ip	–	2474w	–
ν_{C-H}	ip	–	3092w	3155

coverage regime, the molecules tend to adapt a slight tilted geometry with respect to the underlying Au(111) surface (along its short axis) like it is found in the molecule trans configuration crystal structure [131].

4.2 Electronic properties

4.2.1 1,3,8,10-Tetraazaperopyren

In order to gain more insights in the electronic properties of the different TAPP derivatives, electronic HREEL spectra were measured in specular geometry with a primary electron energy of $E_0 = 15.5$ eV. Figure 4.11 shows the electronic HREELS spectrum of 1 ML a), 1 ML annealed to 550 K b) and a 3 ML c) coverage of TAPP on Au(111) in the loss energy range from 1.0 to 4.0 eV. The corresponding, employed Gaussian fits to each of the observed features and their resulting envelope (red line) is shown as well. The low energy side of the spectrum containing the elastic peak and vibrational losses is omitted for clarity. Measured with a primary electron energy of 15.5 eV, electronic transitions in the adsorbate molecules can be excited. The 1 ML spectrum in Figure 4.11 a) shows three electronic transitions. The strongest feature is found at 2.86 eV which is assigned to the HOMO-LUMO transition of the pristine TAPP molecule which fits nicely to the published value for HOMO-LUMO gap of TAPP-$(C_3F_7)_2$ with 2.84 eV ($\lambda = 436$ nm) obtained via UV/vis spectroscopy in THF solutions [131], see Table 4.4 for a detailed list of all observed electronic transitions for different TAPP coverages. The origin of the less prominent features located at 1.21 eV and 1.69 eV is more ambiguously.

Two possibilities explaining these findings well be discussed in detail. The first would be the generation of a negatively charged species induced by the incoming electrons of the electron beam. Second is the formation of metal organic frameworks (metal-organic complexes) on the gold surface in which the gold atoms from the substrate bond to the TAPP molecules via the nitrogen atoms. In such complexes a charge separation between the metal atom and the ligand molecule would be expected giving the metal atom a positive and the organic ligand a negative charge.

The generation of a negatively charged species induced by the electrons on a metal surface that shows a long enough lifetime in order to be visible during the HREELS measurements can be ruled out. Excess charge would easily decay into the underlying metal substrate.

A possible explanation for a stabile, probably negative charged species can be found in the context of organometallic complex formation. It is known, that TAPP molecules on the Cu(111) surface incorporate copper atoms to form stabile metal organic complex like structures on the surface [132]. For other systems complex formation was found as well and results in the altering of the electronic structure of the metal-organic complex. For example for the well studied system PTCDA on Ag(110 and Ag(111) it is known

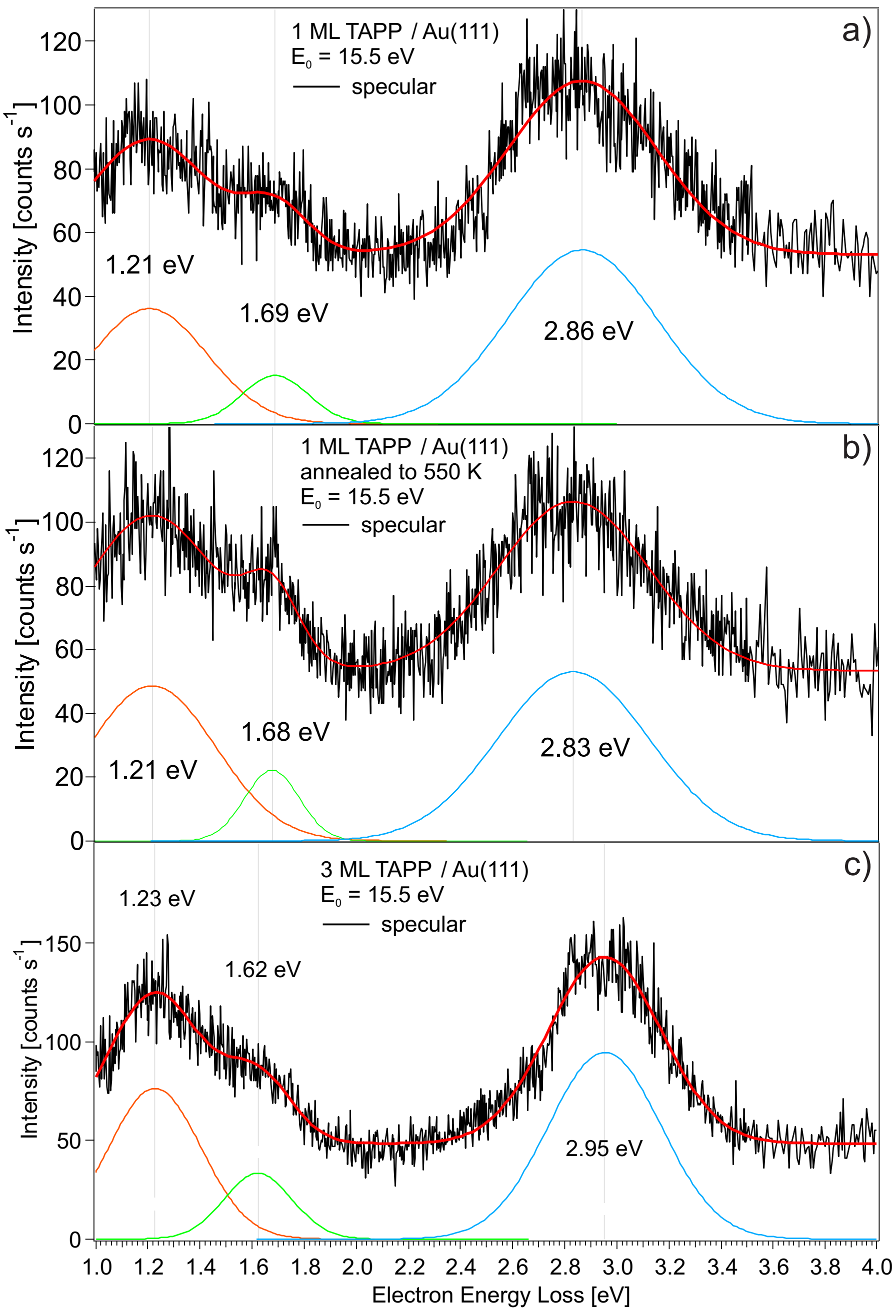

Figure 4.11: Electronic HREEL spectra measured in specular (solid black line) geometry of 1 ML a), 1 ML annealed to 550 K b) and 3 ML c) TAPP on Au(111). The employed Gaussian fits and their resulting envelope (solid red line) is shown. The low loss side ranging from the elastic peak at 0 eV up to 1 eV (containing vibrational features but no electronic transitions) is omitted for clarity. The resolution (FWHM) for the specular geometry was was better than 8 meV.

that the molecules form chemisorptiv bonds to the metal substrate. Electronic HREEL experiments (employing primary electron energies of $E_0 = 20$ eV) reveal the build up of new electronic features in the low energy range while the HOMO-LUMO transition remains observable [138]. In another HREEL study doping of a multilayer of PTCDA on Ag(110) with potassium atoms show the same effect and new electronic features arising from metal-organic adatom complexes appear [139].

A similar behavior might be the explanation for the Au(111) TAPP system as well. Coordination of gold atoms at the different nitrogen atoms, that offer potential binding sites, might lead to the formation of stable gold TAPP organo-metallic complexes.

Table 4.4: Electronic transitions for different coverages of TAPP as indicated. Peak positions are determined via the peak maximum of the employed Gaussian fit.

coverage	**electronic transition [eV]**
1 ML	1.21, 1.69 and 2.86
1 ML(550K)	1.21, 1.68 and 2.83
3 ML	1.23, 1.62 and 2.95

From in situ UV-vis spectra obtained during the oxidation/reduction of a TAPP molecule with alkan substituents in 2 and 9 position in a spectroelectrochemical cell (cyclic voltammetry), the absorption spectrum of the anionic species in THF is accessible [130]. The absorption spectra continually measured during the reduction to the monoanionic species shows the vanishing of the former HOMO-LUMO transition located at around 2.83 eV (411nm - 437 nm) and the build up of a new, intense absorption feature ranging from 2.25 eV (550 nm) to 1.65 eV (750 nm) with its maximum absorbance at 1.94 eV (640 nm) [130]. The reduction to the monoanionic form is accompanied by a colour change of the solution to deep blue.

Derived from UV-vis absorption spectra of organic dye molecules it was found that upon reduction a red shift of the observed electronic transitions occurs in the order of 1 eV and even higher magnitudes, this behavior is well known for a lot of comparable systems as well [140–142].

These findings let us conclude that the observed low energy, electronic transitions arise from a gold adatom species. The fact that the observed HOMO-LUMO transition of the pristine TAPP molecule (in agreement to UV/vis) is still observable can only be explained by the fact that not all of the TAPP molecules form adatom complexes on the surface. Figure 4.11 b) shows the electronic HREEL spectrum of the to 550 K annealed 1 ML phase of TAPP. Three electronic transitions are observed at 2.83 eV assigned to the HOMO-LUMO gap, 1.68 eV and 1.21 eV arising from the HOMO-LUMO transitions of the gold adatom species. Compared to the initial spectrum, Figure 4.11

a), before heating, no significant shift is observed that would point to a drastic change in the electronic structure of the TAPP molecules.

The electronic HREEL spectrum of a 3 ML TAPP coverage is shown in Figure 4.11 c). The spectrum exhibits three features centered at 1.23 eV, 1.62 eV and 2.95 eV. The transition at 2.95 eV is assigned to the HOMO-LUMO transition. Compared to the monolayer spectrum (Figure 4.11 a)) an enlargement of the gap by 0.09 eV is observed. The broadening of the gap can be explained by the fact that the influence of the metal substrate on the adsorbate, e.g. lowering of the molecules HOMO and LUMO, diminishes with increasing coverage. The increasing distance of the top most molecular layer will therefore lead to the effect that its properties converge towards those of the free molecule. The electronic transitions found at 1.23 eV and 1.62 eV originating from the gold adatom TAPP complexes are still observable.

4.2.2 2,9-Bisperfluoropropyl-1,3,8,10-Tetraazaperopyren

Figure 4.12 shows the electronic HREEL spectra of 1 ML a) and 6 ML b) TAPP(C_3F_7)$_2$ on Au(111), measured in specular geometry. The employed Gaussian fits describing the observed features are included as well. The spectra are shown in the energy loss range from 1.0 to 4.0 eV. The 1ML spectrum in Figure 4.12 a) contains two electronic transitions located at 1.19 eV and at 2.75 eV. The feature at 2.75 eV is assigned to the

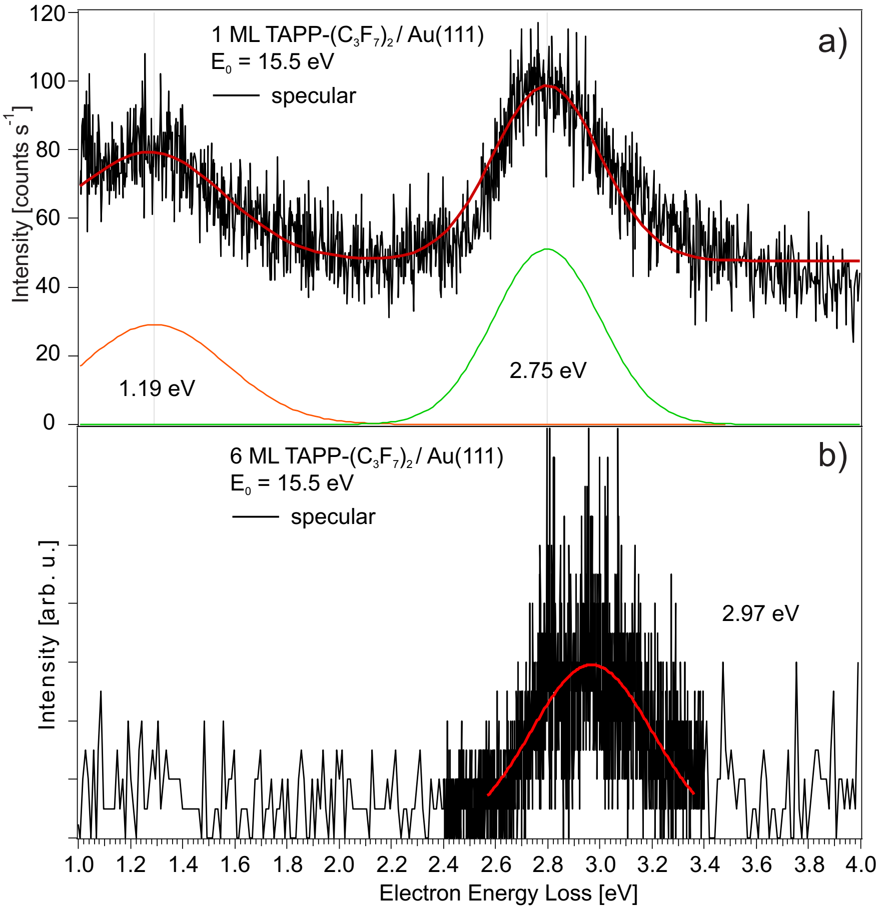

Figure 4.12: Electronic HREEL spectra of 1 ML a) and 6 ML b) TAPP(C_3F_7)$_2$ on Au(111). The employed Gaussian fits and their resulting envelope (solid red line) are shown as well. The resolution (FWHM) for both spectra was around 10 meV (80 cm^{-1}).

HOMO-LUMO transition and is shifted by 0.09 eV to smaller energy as compared to the previously published value of 2.84 eV ($\lambda = 436$ nm) obtained by UV/vis absorption spectroscopy in THF solution [131]. And can be explained by the HOMO-LUMO level alignment of the molecular orbitals with the density of states of the substrate. See Table 4.5 for a list of all observed electronic transitions. The electronic transition at 1.19 eV is assigned to an electronic transition of the adatom, complex species as explained in the previous section. The fact, that only one feature is resolved might be explained by the relatively low overall intensity of the electronic loss spectrum. The electronic HREEL spectrum of 6 ML 2,9-bisperfluoro-propyl-1,3,8,10-tetraaza- peropyren coverage is shown in Figure 4.12 b). One electronic transition, located at 2.97 eV is observed and is assigned to the HOMO-LUMO transition of the molecule. It should be noted, that in contrast to the electronic HREEL spectrum of 3 ML TAPP (Figure 4.11 c)) no further low energy transitions are observed for this high coverage phase. It seem most likely that due to the poor signal to noise ratio less intense features could not be resolved. For the 6 ML coverage another explanation has to be taken into consideration, the gold TAPP adatom complexes that can only be generated in the monolayer, were the molecules have contact to the substrate, can no longer be probed by the incoming electron beam (too low penetration depth) and therefore do not contribute to the measured spectrum.

Table 4.5: Electronic transitions for 1 ML and 6 ML 2,9-bisperfluoro-propyl-1,3,8,10-tetraazaperopyren on Au(111). Peak positions are determined via the peak maximum of the employed Gaussian fit.

coverage	**electronic transition [eV]**
1 ML	1.19 and 2.75
6 ML	2.97

4.2.3 2,9-Bisperfluoropropyl-4,7,11,14-Tetrachloro-1,3,8,10-Tetraazaperopyren

In Figure 4.13 the electronic HREEL spectra of a 1 ML a) and 3 ML b) coverage of TAPP-$Cl_4(C_3F_7)_2$ on Au(111) is shown. The employed fit (solid red line) is shown as well. The 1 ML spectrum, seen in Figure 4.13 a) contains one electronic transition located at 2.62 eV. This feature is assigned to the HOMO-LUMO transition and is in excellent agreement to UV/vis data revealing a gap of 2.64 eV (λ = 469 nm) [131].

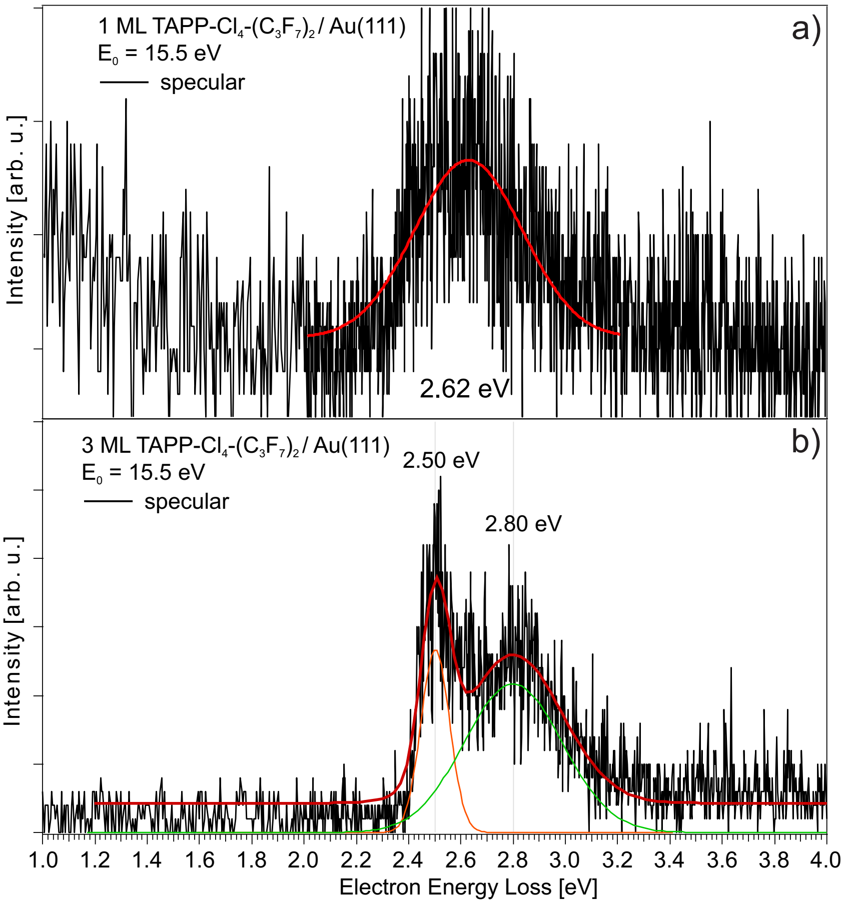

Figure 4.13: Electronic HREEL spectra of a 1 ML a) and a 3 ML b) coverage of TAPP-$Cl_4(C_3F_7)_2$ on Au(111). The employed Gaussian fits (solid red line) is shown as well. The resolution (FWHM) for both spectra was better than 11 meV (88 cm^{-1}).

Apparently, the effect of HOMO-LUMO level alignment with the density of states of the gold substrate is negligible for the chlorinated species or both, HOMO and LUMO are shifted by the same amount thus leaving the gap size unaffected. See Table 4.6 for a list of all observed electronic transitions. In contrast to the previously discussed pristine TAPP and its derivative TAPP(C_3F_7)$_2$, see section 4.2.1 and 4.2.2, respectively, no further electronic transitions in the low energy range are observed.
The really low intensity of the spectrum might lead to a loss of information and thus resolving of less pronounced features is not feasible anymore. An other explanation might be found in the presence of the strong electron withdrawing chloro atoms in 4,7,11,14 position altering the molecules properties in a way that the formation of TAPP gold adatom complexes is not feasible anymore. The higher coverage HREEL spectrum for 3 ML TAPP-Cl$_4$(C_3F_7)$_2$ on Au(111) is shown in Figure 4.13 b). Two electronic transitions are found for this coverage, located at 2.50 eV and at 2.80 eV respectively. The finding of two features in this energy range is rather surprising and its assignment not easily understandable. With increasing coverage, the observed HOMO-LUMO gap shifts to higher loss energies due to less influence of the underlying metal substrate (level alignment as stated in the previous section) as seen before for the pristine TAPP and the fluorinated derivative. Therefore the electronic feature located at 2.80 eV is assigned to the HOMO-LUMO transition. The feature, 300 meV at lower loss energies, centered at 2.50 eV can not unambiguously be assigned and further investigation seem to be necessary.

Table 4.6: Electronic transitions for 1 ML and 3 ML 2,9-bisperfluoropropyl-4,7,11,14-tetrachloro-1,3,8,10-tetraazaperopyren on Au(111). Peak positions are determined via the peak maximum of the employed Gaussian fit.

coverage	**electronic transition [eV]**
1 ML	2.62
3 ML	2.50 and 2.80

4.3 Conclusions

Employing HREEL- and TPD spectroscopy we investigated the adsorption behavior and electronic properties of 1,3,8,10-Tetraazaperopyren and its derivates 2,9-bisperfluoropropyl-1,3,8,10-tetraazaperopyren and the halogenated species 2,9-bisperfluoropropyl-4,7,11,14-tetrachloro-1,3,8,10-tetraazaperopyren on a Au(111) substrate starting from monolayer coverage up to several layers.

4.3.1 1,3,8,10-Tetraazaperopyren

It is found that the flat TAPP adsorbs in a planar orientation with respect to underlying gold substrate, this behavior persists during further adsorption and only a slightly roughening of the surface can be observed for higher coverages. Out-of-plane modes originating from the carbon skeleton and modes arising from oop hydrogen deformations dominate the HREEL spectra. Using TPD spectroscopy to determine initial coverages is rather ambiguous due to the fact that the molecules in contact with the surface (monolayer) decompose during the process which is proven by a HREEL spectrum taken afterwards (see Appendix B Figure B.1).

When using sufficiently high enough primary electron energies in HREEL, electronic transitions can be excited as well. The electronic HREEL spectrum of TAPP shows three electronic transitions located at 1.21 eV, 1.69 eV and 2.86 eV respectively. The feature at 2.86 eV is assigned to the HOMO-LUMO gap and fits very good to UV/vis data measured in THF solutions for the substituted tetraazaperopyrenes yielding 2.84 eV [131]. The assignment of the first two transitions is not that straight forward. When combining cyclovoltammetry with in situ UV/vis spectroscopy the changes in the absorbance spectrum (electronic transitions) during reduction are accessible. The monoanionic species formed now shows that the former HOMO-LUMO gap, located around 2.6 to 2.8 eV vanishes and new features in the range from 2.25 eV (550 nm) to 1.65 eV (750 nm) build up [131]. Although the existence of a charged species, exhibiting a long enough lifetime to be observed in the experiment is very unlikely it is known that adatoms from the substrate can bind with the adsorbed molecules and thus stabilize the probably charged species by complex formation [132, 138, 139]. Keeping these findings in mind, the in HREELS observed electronic transitions in the low loss energy region at 1.21 eV, 1.69 eV can be assigned to an adatom complex in which gold atoms mediated by the substrate bond to the TAPP molecules.

4.3.2 2,9-bisperfluoro-propyl-1,3,8,10-tetraazaperopyren

The fluorinated molecule TAPP(C_3F_7)$_2$ is more sterically demanding due to its fluorinated propyl side chains. The orientation of these groups in the crystal structure is shown in Figure 4.14 and reveals a trans configuration of the fluorinated chains with respect to each other while the tetraazaperopyrene core remains in a planar geometry [131]. Vibrational HREEL spectra of a monolayer coverage is dominated by the out-of-plane modes of the carbon skeleton and stretching modes of the propylene substituents, thus revealing a flat lying molecule with respect to the gold surface, with the fluorinated propyl side chains in a cis orientation pointing upwards. The cis configuration will lead to an increased overlap of the extended π system of the molecule with the density of states of the gold substrate and thus to a stronger physisorptive bonding situation. When increasing the coverage the stretching modes of the fluorinated side chains are more pronounced in the vibrational HREEL spectrum while out-of-plane modes originating from C-H bending become less intense. A geometrical change must have taken place. For higher coverages when the influence of the underlying substrate decreases the molecules tend to relax into their energetically favoured trans state, with small deviations along the short molecular axis as found in the bulk crystal structure shown in Figure 4.15 [131]. The intermolecular stacking distance lies in the range from 3.37 - 3.51 $\mathring{A}$ with smaller values for the halogenated species.

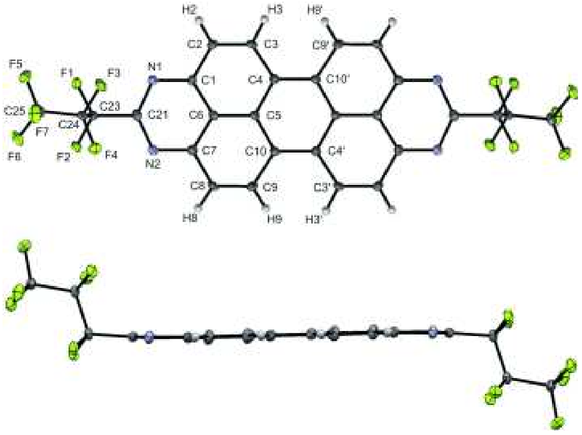

Figure 4.14: Crystal structure of TAPP-R_4-(C_3F_7)$_2$, image adapted from Ref. [131].

The electronic HREEL spectra of 2,9-bisperfluoro-propyl-1,3,8,10-tetraazaperopyren reveals two transitions at 1.19 eV and at 2.75 eV respectively. The latter is assigned to the HOMO-LUMO transition and fits nicely to UV/vis data with a value of 2.64 eV for the HOMO-LUMO transition [131]. The broad feature at 1.19 eV is assigned to an adatom complex species (an organo-metallic gold complex as explained in the previous subsection 4.3.1). For higher coverages, in this case 6 ML, only one transition can be observed. Located at 2.97 eV this feature is assigned to the HOMO-LUMO transition of the molecule. No further excitations are observed. The adatom species formed in the monolayer regime does obviously not contribute to the spectrum anymore, a fact accounted to the low penetration depth of the employed low primary energy electrons. The substitution in 2 and 9 position can be used to induce structural changes when thicker layers are demanded in the desired application, the effect on the electronic structure on the other hand is negligible. This finding can be explained be the fact that the frontier orbitals show a nodal plane going along the long molecular axis and thus cutting through the carbon atoms in 2 and 9 position [130, 143].

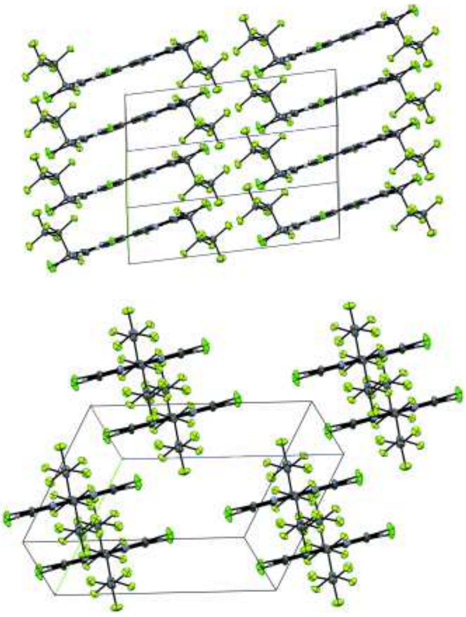

Figure 4.15: Crystal structure of molecular stacking in bulk TAPP-R_4-$(C_3F_7)_2$, image adapted from Ref. [131].

4.3.3 2,9-Bisperfluoropropyl-4,7,11,14-Tetrachloro-1,3,8,10-Tetraazaperopyren

As seen in the previous subsection, the vibrational HREEL spectra in the monolyer regime of TAPP-$Cl_4(C_3F_7)_2$ is mainly dominated by stretching modes arising from the fluorinated propyl side chains and out-of-plane bending/buckling modes originating from the tettraazaperopyrene core. Out-of-plane modes arising from C-H bending are almost negligible which is due to their low occurrence in the tetra-halogenated species. These findings lead to the conclusion that the tetra halogenated derivate adsorbs in planar geometry with respect to the Au(111) surface with its side chains pointing upwards (cis like). When increasing to coverage up to 3 ML the stretching vibrations of the side chains becomes even more pronounced. In-plane stretching vibrations arising from the C-N-C of the tetraazacore appear and show some dipole activity. A slight tilt along the short molecular axis is accounted for these findings, moreover the multilayer regime again represents the energetically favoured trans configuration.

The electronic HREEEL measurements in this case harbor a major difficulty which has to be mentioned; the control unit of the spectrometer broke down during these experiments. It can not be ruled out that the relatively low intensities in the electronic spectra and the surprising double peak feature in the 3 ML regime emerges from this fact and repetition of these measurements should be considered. Never the less the monolayer regime reveals a width of the HOMO-LUMO gap of 2.62 eV which is in perfect agreement with UV/vis data showing a gap of 2.64 eV (λ = 469 nm) [131]. Evidently, level alignment of the molecular orbitals with the electronic structure of the substrate is either negligible or both the HOMO and the LUMO shift by the same value leaving the size of the gap unchanged. Increasing the coverage to three ML two transitions located at 2.50 eV and at 2.80 eV respectively are observed. Expecting a shift for the HOMO-LUMO transition towards higher loss energies upon increasing coverage the feature at 2.80 eV is assigned to the HOMO-LUMO gap.

In conclusion it can be stated that in the monolayer regime a planar adsorption geometry with respect to the substrate is favoured. For higher coverages the substituents in 2 and 9 position govern the further molecular orientation. When no substituents are present the planar motif persists. With the fluorinated propyl chains attached the molecular orientation approaches the trans configuration as seen in the bulk crystal structure. Furthermore it was found that the core substitution of the tetraazaperopyrenes with halogens (electron withdrawing groups) alters its electronic properties and a decrease of the HOMO-LUMO gap size results.

Chapter 5

Octithiophene on Au(111)

Oligothiophenes show a high potential for applications in organic field effect transistors (OFETs) [19–21], optoelectronic devices like organic light-emitting diodes (OLEDs) [19, 144] and in photovoltaic cells comprised from organic molecules (OPVC) [144, 145]. Which is due to their semiconducting properties and most importantly attributed to the fact that the optical and electronic properties can easily be altered by variation of the chain length of the employed π-conjugated oligothiophene molecule [146–150]. A HREELS study revealed that the size of the HOMO-LUMO band gap strongly depends on the length of the oligothiophenes e.g. of the number of comprised thiophene rings within the molecular chain [151]. The structure of the α-octithiophene (α-8T is shown in Figure 5.1. The sulphur atoms of the thiophene rings alternately point upwards and downwards respectively.

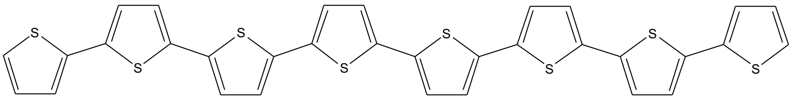

Figure 5.1: Structure of 8T molecule.

When thinking of technical applications of organic molecules in electronic devices one has to consider many parameters of which the interaction with the underlying substrate (electrodes providing electric contact; photovoltaic cell junctions) e.g. metal altering the properties of such an interfaces plays a crucial role. In the case of oligothiophenes it was found that the orientation of the molecules with respect to the surface (planar or upwards tilted along the long molecular axis) plays an important role for the light emission and absorption as well as the charge transport properties [152]. In such interfaces the finally received adsorption geometry is the result of the competing effects in

the vicinity of the adsorbed molecule like molecule/substrate and intermolecular interactions in which the energetically favoured orientation prevailed.
Investigations of the two thiophene rings shorter analog α-sexithiophene (6T) revealed a well-ordered film growth on gold with planar orientated molecule chains. When changing the substrate to Ag and Cu respectively the molecules adsorb in a tilted fashion with angles up to 70° with respect to the substrate [153]. The absorption behavior of 6T on various metal substrates was intensively studied in the past years [154–161]. In contrast to 6T only a few recent studies employing STM were carried out to gain more insights in the adsorption properties of the longest unsubstituted α-oligothiophene that has been synthesized so far, the α-octithiophene, on Au(111) [162] and on Cu(111) [163] substrates respectively. This 8T molecule comprised of 8 thiophene rings possesses the highest carrier mobility of all unsubstituted oligothiophenes up to now [164, 165] offering great potential in further applications. Thus making the knowledge of the initial adsorption stages urgently required. For the 8T/Au(111) system they found a predominantly planar adsorption in the low coverage regime and a structural change upon reaching a dense monolayer which was interpreted as a tilting along the long molecular axis of 8T but no unambiguous evidence could be elucidated in the performed STM experiments so far [162].
For details about the sample preparation and molecule dosage see section 2.1.3 in the Experimental Details. In this chapter we show and discuss the findings of the performed HREEL measurements of the α-octithiophene molecule evaporated on the Au(111) substrate ranging from the sub-monolayer to a densely packed ML coverage and answer the question if the α-8T molecules change their adsorption geometry when the monolayer coverage is reached.

5.1 Adsorption Geometry

From previously performed STM measurements adapted from Reference [162], shown in Figure 5.2 the orientation of the single molecule an a gold substrate was found to be planar (a). Eight bright spots (black) are clearly seen in the image arising from the eight thiophene rings. Image b) shows the perfectly ordered films of a one ML and a two ML coverage respectively. In c) a STM image of a densely packed ML coverage is shown. The former eight bright spots are now less pronounced, in fact only 4-5 intense spots (black) can be observed for this coverage regime suggesting a structural change when going from sub-ML to ML coverage. Although the STM images clearly reveal a major, structural difference for the sub-ML and the ML phase, a conclusive statement of the molecular orientation could not be made and further investigations remain necessary.

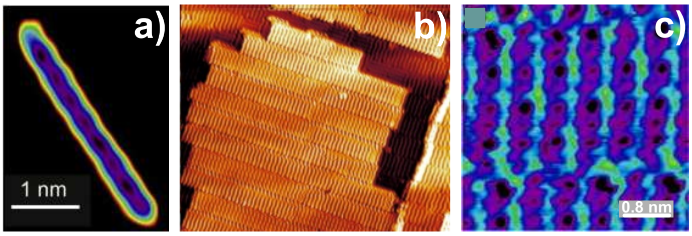

Figure 5.2: STM images of 8T on Au(111) adapted and rearranged for clarity from Reference [162]. a) Sub-molecular resolution STM image of a single molecule exhibiting eight features corresponding to the 8 thiophene rings, b) STM image of a mono-and bilayer on Au(111) (Vs = 0.6 V (bias voltage), It = 50 pA (tunneling current)) showing perfectly aligned 8T rows, c) High resolution STM image of densely packed monolayer 8T (Vs = 2 V, It = 200 pA) showing less bright features which arises from a tilted absorption geometry.

To gain insights into the adsorption geometry of the α-octithiophene molecules on the Au(111) surface we performed angular-dependent HREELS measurements .The HREEL spectra shown in Figure 5.3 were recorded in specular and in 7°-off-specular geometry, respectively. For a complete assignment of the observed vibrational modes see Table 5.1.

The specular spectrum of a sub-ML coverage (shown in Figure 5.3 a)) is dominated by three very strong, dipole active features, which can be assigned to an out-of-plane ring deformation located at 441 cm^{-1} and to the C-H out-of-plane bending modes arising at 674 cm^{-1} and at 774 cm^{-1} respectively. In the off-specular measurement, these features become very weak which indicates that their intensities are predominantly originating from dipole-scattering. The comparison between the sub-ML HREELS and IR data, shows that the in-plane modes are not observed at all in the HREELS measurement, whereas the out-of-plane modes are very strong. These findings lead to the conclusion that in the low coverage regime the octithiophene molecules adsorb in a planar geometry with respect to the underlying Au(111) substrate.

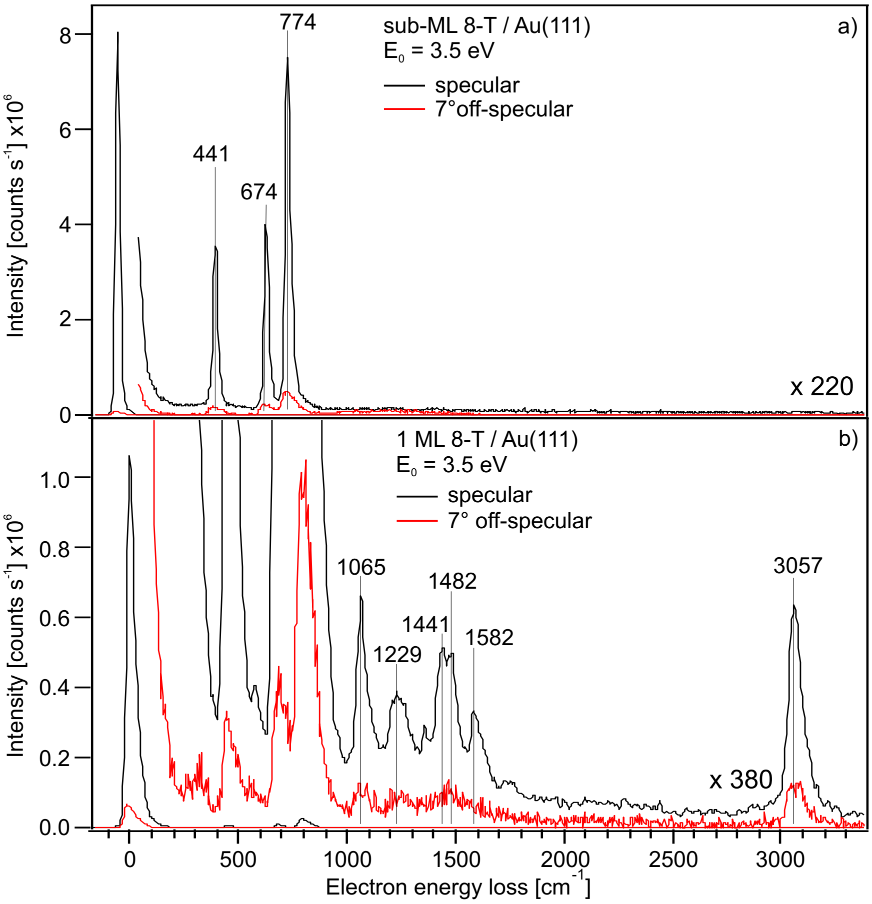

Figure 5.3: Vibrational HREEL spectra measured with a primary electron energy of E_0=3.5 eV in specular (solid black line) and in 7°-off-specular geometry (solid red line) respectively of a sub-ML a) and a 1 ML b) coverage of α-Octithiophene molecules on Au(111). The achieved resolution (FWHM) for the specular geometry was 24 cm^{-1} (3.0 meV) and for the off-specular 30 cm^{-1} (3.8 meV).

When increasing the coverage towards one monolayer, as shown in Figure 5.3 b), more vibrational losses can be observed suggesting a major change in the molecular orientation on the surface. The dipole active, out-of-plane features arising from ring deformation and bending modes of δ_{CH} still contribute to the spectrum. Furthermore, in the monolayer regime, vibrational losses arising from in plane modes appear as well.

Table 5.1: Assignment of vibrational modes for different α-octithiophene coverages on Au(111). All vibrational frequencies are given in cm^{-1}. IR data from condensed phase adapted from Ref. [166]. ν, indicates stretch; δ, bending; oop, out-of-plane; ip, in-plane. w, indicates weak; m, medium; s, strong; vs, very strong. A strong dipole activity is indicated by (da).

vibrational mode		**sub-ML**	**1 ML**	**IR data**
$\delta_{thiophene}$	oop	441s(da)	433s(da)	455
δ_{CH}	oop	674s(da)	670s(da)	687
δ_{CH}	oop	774vs(da)	770vs(da)	790
δ_{CH}	ip	–	1065w	1047
δ_{CH}	ip	–	1229w	1222
$\nu_{symC=C}$	ip	–	1441w	1424
$\nu_{asymC=C}$	ip	–	1482w	1491
$\nu_{thiophene}$	ip	–	1582w	1510
ν_{symC-H}	ip	–	3057m(da)	3050

At 1065 cm^{-1} and 1229 cm^{-1} respectively bending modes assigned to δ_{CH} appear. In plane stretching vibrations arising from $\nu_{symC=C}$ and $\nu_{asymC=C}$ can be observed at 1441 cm^{-1} and 1482 cm^{-1} respectively. The thiophene ring stretching mode can be found at 1582 cm^{-1}. At 3057 cm^{-1} an intense, dipole active feature arising from the symmetrical stretch vibration of ν_{sym} CH appears. These findings lead to the conclusion, that the

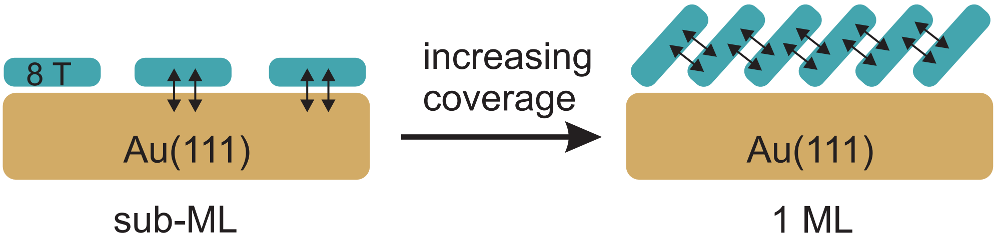

Figure 5.4: Sketch of molecular reorientation of 8T molecules when increasing the coverage towards 1 ML. Side view along the long molecular axis. Arrows indicate attractive interaction.

α-octithiophene molecules adapt a tilted orientation with respect to the Au(111) substrate when a coverage of 1 ML is reached. In Figure 5.4 a schematic drawing elucidates the orientational rearrangement of the 8T molecules.

5.2 Conclusions

The adsorption behavior of sub-monolayer and monolayer coverages of α-octithiophene molecules evaporated on a Au(111) surface was investigated by means of HREEL spectroscopy.

The sub-ML and ML HREEL spectra measured in specular geometry are shown together in Figure 5.5 (sub-ML as black line, 1 ML as blue line) for comparison. From the conducted vibrational HREELS measurements it can be stated that in the sub-ML regime the 8T molecules adapt in a planar geometry with respect to the surface since the observed vibrational losses, which comprise a strong dipole activity, arise only from out-of-plane modes. In-plane modes are completely absent in this coverage regime.

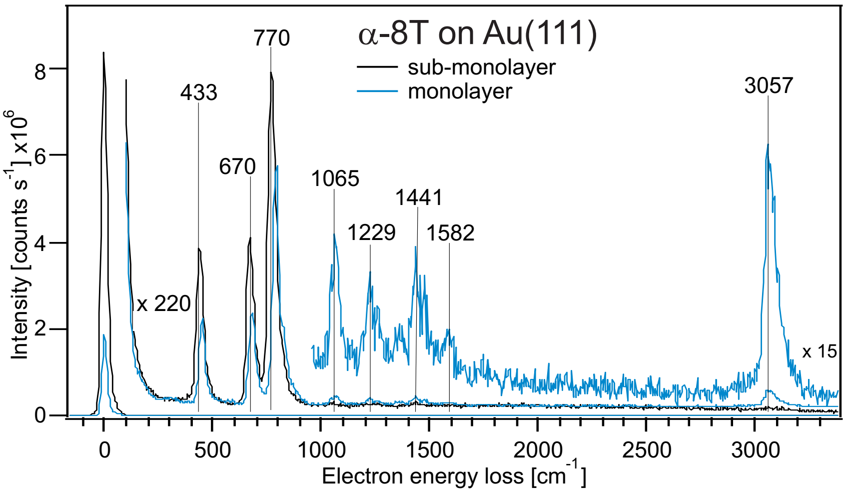

Figure 5.5: Vibrational HREEL spectra measured with a primary electron energy of E_0=3.5 eV in specular geometry of a sub-ML α-octithiophene (solid black line) and of one ML α-octithiophene (solid blue line) respectively for ease of comparison.

When increasing the coverage to 1 ML the spectrum becomes more complex and vibrational losses arising from in-plane modes appear in the spectrum. The overall intensity of the 1 ML spectrum is considerable lower than for the sub-ML case. In plane modes, containing some dipole activity, originating from C-H bending δ_{CH} and C=C stretching $\nu_{C=C}$ modes show up in the spectrum, confirming a structural change of the adsorbed molecules. The appearance of the rather strong ν_{C-H} stretching mode exhibiting a strong dipole activity underpins the previous findings and lead to the conclusion that for the ML regime the α-octithiophene molecules adapt a tilted orientation along its long molecular axis with respect to the surface. In the sub-monolayer regime

the molecule/substrate interaction, like molecule π-system overlapping with density of states (dos) of the metal, dominate and define the adsorption geometry. When reaching a certain coverage threshold, repulsion between the nearest neighboring molecules lead to a reorientation and the former planar adsorbate begins to tilt its molecular plane and intermolecular interaction like π-π stacking between the octithiophenes takes over resulting in another energetically favoured structural motif on the surface.
The results of this chapter were published under the title: Coverage-dependent adsorption geometry of octithiophene on Au(111) in Phys. Chem. Chem. Phys., 14, **2012**, 691-696.

Chapter 6

3,4,9,10-Perylene-tetracarboxylic-dianhydride on Au(111)

The adsorption behavior of organic molecules on different substrates have been intensively investigated to gain insights into the properties of the substrate adsorbate system, it was found that some organic molecules have the ability to form well ordered structures upon adsorption, such knowledge is the key for further application in organic electronic devices [167–169]. One of the best studied molecular system adsorbed on a metal surface is the model compound 3,4,9,10-Perylene-tetracarboxylic-dianhydride (PTCDA). The structure is shown in Figure 6.1. There exist numerous reports of PTCDA on many different substrates investigated by a wide range of spectroscopic methods [170–177]. The adsorption behavior of PTCDA on metal substrates strongly depends on the growth conditions applied. For substrate temperatures around 298 K a nonequilibrium growth regime was found via grazing incidence x-ray diffraction (GXID) [170]. The first 2 monolayers grow in the layer by layer type. Multilayer growth was observed via spot profile analysis(SPA)low-energy electron diffraction (LEED) and GXID. At sample temperatures of 298 K this regime is preserved although the surface

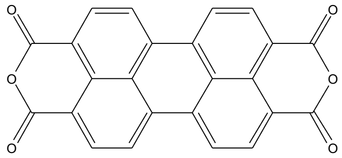

Figure 6.1: Structure of PTCDA molecule.

roughness increases with increasing coverage [171,172]. These findings are in agreement with near edge x-ray absorption fine structure (NEXAFS) spectroscopy [173,174]. For PTCDA on the Au(111) surface scanning tunneling microscopy (STM) combined with reflection high-energy electron diffraction (RHEED) and LEED measurements respectively reveal a dominant herringbone-like molecular pattern among other structural motifs on the substrate. The herringbone reconstruction of the Au(111) surface is still visible through the first PTCDA layer, suggesting a rather weak interaction between the substrate and the molecules [175–177]. The observed superstructure motifs arise from the different hydrogen bonding possibilities of the PTCDA molecules [178]. Employing normal incident X-ray standing wave (NIXSW), the adsorption height of PTCDA on Cu(111), Ag(111) and Au(111) substrates were measured, revealing a bonding distance of 2.66, 2.86 and 3.27 Å respectively [179–181], suggesting a chemisorptive bond formation for the Cu(111) and Ag(111) system. In case of the Au(111) substrate, the bonding distance is very close to the stacking distance in bulk PTCDA of 3.22 Å [182], leading to the assumption that the bonding situation can best be described as physisorptive. The chemisorptive character of the PTCDA molecules in contact with the Ag(111) or Cu(111) substrate leads to a dissociation of the PTCDA molecules upon heating [183,184]. Hence the binding energy of the molecules can not be determined with TPD. An alternative route to overcome such obstructions would be a calorimetric experiment [185,186]. The optical HOMO/LUMO-gap derived from absorption spectra was found at 2.6 eV [187,188]. Hobley *et al.* performed absorbtion spectroscopy on PTCDA nanoparticle clusters in polar solvents down to 200 nm. On the high energy side in those spectra, transitions at 5.6, 4.9, 3.3 and 3,5 eV besides the HOMO/LUMO including vibronic components are observed [189]. For 100 nm thick films of PTCDA on SiO_2, UV/Vis absorbtion spectra also exhibit transitions at 3.3 and 3,5 eV [187]. A theoretical approach of Zhanpeisov *et al.* employed time dependant density functional theory (TDDFT) to simulate discrete UV/Vis spectra of PTCDA in the range from 200 to 510 nm, resulting transitions at 2.5, 3.6, 4.7, 5.2 and 5.4 eV. The strongest feature on the low energy side at 2.5 eV is attributed to the HOMO/LUMO transition. The feature at 3.6 eV was assigned to a transition from HOMO-5 to LUMO [190]. Employing combined ultraviolet photoemission spectroscopy (UPS) and inverse photoelectron spectroscopy (IPES) the HOMO and LUMO positions respectively of 50-100 Å thick films of PTCDA on Au were found to be at -2.5 and +1.5 eV with respect to the Au Fermi level (E_F) measured at the corresponding peak maximum positions. Subtracting the vibrational contributions and the difference between bulk and surface polarization leads to a transport gap of 3.2 eV [191]. Scanning tunneling spectroscopy (STS) for 1 ML of PTCDA on Au reveal the HOMO and LUMO positions to be at -2.18 and 1.33 eV relevant to E_F respectively resulting in a transport gap of 3.5 eV when taking the peak maximum positions. This gap increases upon increasing coverage and was found to be 3.8 eV for 2-3 layer coverage. Note that the transport gap for the creation of an electron-hole pair contains a high polarization energy contribution which can not be neglected and thus leads to a transport gap which is approximately 1 eV larger than the optical gap [188].

For details about the dosage parameters of PTCDA and the sample preparation see section 2.1.3 in the Experimental Details chapter.

In this chapter we report on the adsorption and electronic properties of PTCDA on Au(111) from the monolayer regime up to several layers by means of HREELS and TPD measurements. Furthermore the binding energy in the limit of a single PTCDA molecule was elucidated via a complete analysis approach [192].

6.1 Adsorption Geometry

In order to gain information about the adsorption geometry as a function of coverage HREEL spectra for 1, 2 and 6 monolayer (ML) coverage were measured in specular and off-specular scattering geometry respectively, see Figure 6.2. See Table 6.1 for an assignment of the observed vibrational modes and a comparison between the different coverages. The vibrational loss spectra of 1 ML PTCDA on the Au(111) surface is shown in Fig. 6.2a. It consists of five distinct modes. The most intense vibrational modes at 871 cm^{-1}, 807 cm^{-1} and 727 cm^{-1} are assigned to the out-of-plane bending of C-H and out-of-plane bending modes of the CCC backbone of the molecule. The very intense loss feature at 201 cm^{-1} is attributed to out-of-plane bending modes of the PTCDA scaffold along its short axis. The off-specular spectrum contains only very low intensities, meaning that all of the observed vibrational loss features can be assigned to dipole-active modes, therefore we conclude that the PTCDA molecules adopt a planar adsorption geometry with respect to the Au(111) substrate. Upon increasing coverage,

Table 6.1: Assignment of vibrational modes for different PTCDA coverages on Au(111). All vibrational frequencies are given in cm^{-1}. IR data adapted from Ref. [193]. *Calculation was done with the DFT B3LYP functional using the 6-31G basis set adapted from Ref. [194]. ν, indicates stretch; δ, bending; oop, out-of-plane; ip, in-plane. w, indicates weak; m, medium; s, strong; vs, very strong. A strong dipole activity is indicated by (da).

vibrational mode		**1 ML**	**2 ML**	**6 ML**	**IR data**	**calc.***
δ_{C-C-C}	oop	201 vs (da)	199 vs (da)	199 vs (da)	–	194
δ_{C-O-C}, $\delta_{C=O}$	ip	–	–	380 w	–	371
δ_{C-C-C}, $\delta_{C-C=O}$	ip	–	–	436 w	438	446
δ_{CC}, long axis folding	oop	562 m	559 m	569 m	572	592
$\delta_{O=C-C}$, δ_{C-O-C}, δ_{CCC}	oop	727 vs (da)	729 s (da)	740 s (da)	734	732
δ_{C-H}, δ_{CCC}	oop	807 s (da)	803 s (da)	811 s (da)	809	803
δ_{C-H}	oop	871 s (da)	869 s (da)	874 s (da)	862	889
ν_{C-O}, ν_{CC}	ip	–	–	1022 m	1025	1036
δ_{CH}, ν_{C-O}	ip	–	–	1134 w	1122	1133
δ_{CH}, ν_{CC}	ip	–	–	1239 w	1234	1278
δ_{CH}, ν_{CC}	ip	–	–	1298 m	1300	1325
ν_{C-C}, δ_{C-H}	ip	–	–	1592 m	1594	1649
$\nu_{C=O}$	ip	–	1765 w	1767 m	1772	1763
ν_{symC-H}	ip	–	3092 w	3094 w	–	–

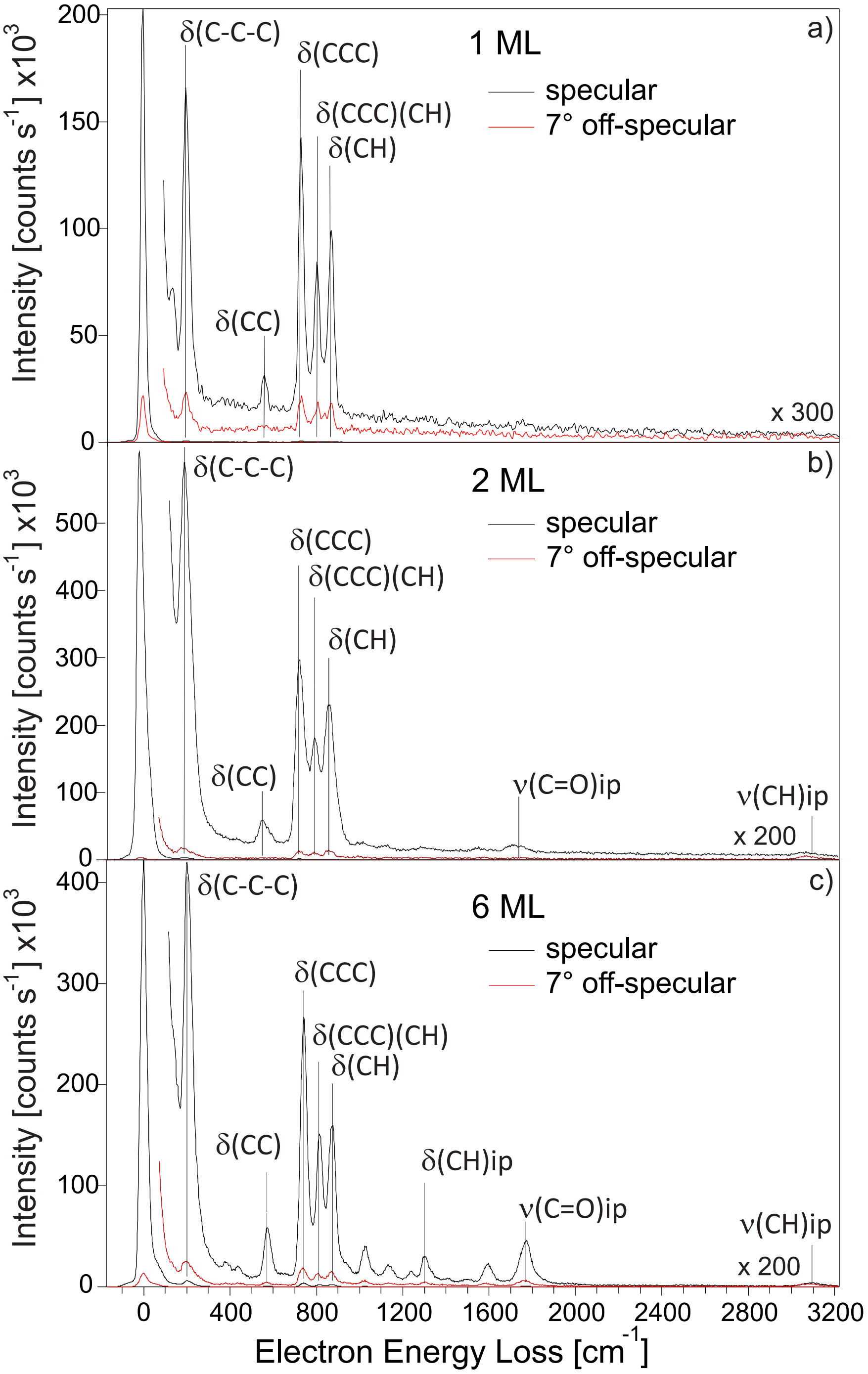

Figure 6.2: Vibrational HREEL spectra of PTCDA on Au(111) in specular (black line) and 7° off-specular (red line) scattering geometry, respectively. Primary electron energy was e_0=3.5 eV for a) 1 ML, b) 2 ML and c) 6 ML PTCDA coverages.

losses arising from in-plane vibrations are observed in the spectrum. In the 2 ML regime, shown in Fig. 6.2b, the in-plane stretch vibration of C=O at 1767 cm^{-1} appears and gets more intense in the higher coverage spectra at 6 ML as shown in Fig. 6.2c. In this high coverage spectrum all of the out-of-plane, dipole-active modes which were already observed for the monolayer coverage still persist. Furthermore it shows several in-plane vibrations which all contain dipole-activity. The loss feature at 1022 cm^{-1} was assigned to in-plane stretching modes of C-O and C-C. The vibrational mode at 1592 cm^{-1} was assigned to in-plane bending modes of C-H. At 3094 cm^{-1} the in-plane stretching mode of C-H can be observed. The appearance of dipole-active, in-plane vibrational modes lead to the conclusion that the adsorption geometry of the PTCDA molecules with respect to the metal surface are no longer strictly planar and that under the present growth condition, the molecules adopt a slightly tilted geometry in the high coverage phase. These findings are in good agreement to previously published results [171–174]. The first two layers grow in a layer by layer fashion thereby the growth strongly depends on the substrate temperature. For sample temperatures around 300 K, a layer by layer type growth was observed. At high coverages, PTCDA molecules begin to adopt a more tilted orientation leading to a rougher surface.

6.2 Binding Energy

To obtain further informations concerning the binding properties of PTCDA on Au(111), a series of TPD spectra for coverages up to 16 ML were measured, as shown in Figure 6.3. The multilayer spectrum contains three peaks (α_1, α_2 and α_3). The inset shows a close up of peak α_3 for a more detailed view. All traces belonging to peak α_1 share their leading edges and a clear shift of Tα_{1max} to higher temperatures with increasing coverage can be observed, which is explained due to intramolecular hydrogen bonds which are formed within the PTCDA domains [178], suggesting a zero order desorption process. Desorption most likely starts at the boundaries of such domains. Upon increasing dosage time, peak α_3 saturates at around Tα_{3max} = 710 K, we assign this peak to the first ML of PTCDA. Upon further adsorption a second peak at 520 K (α_2)

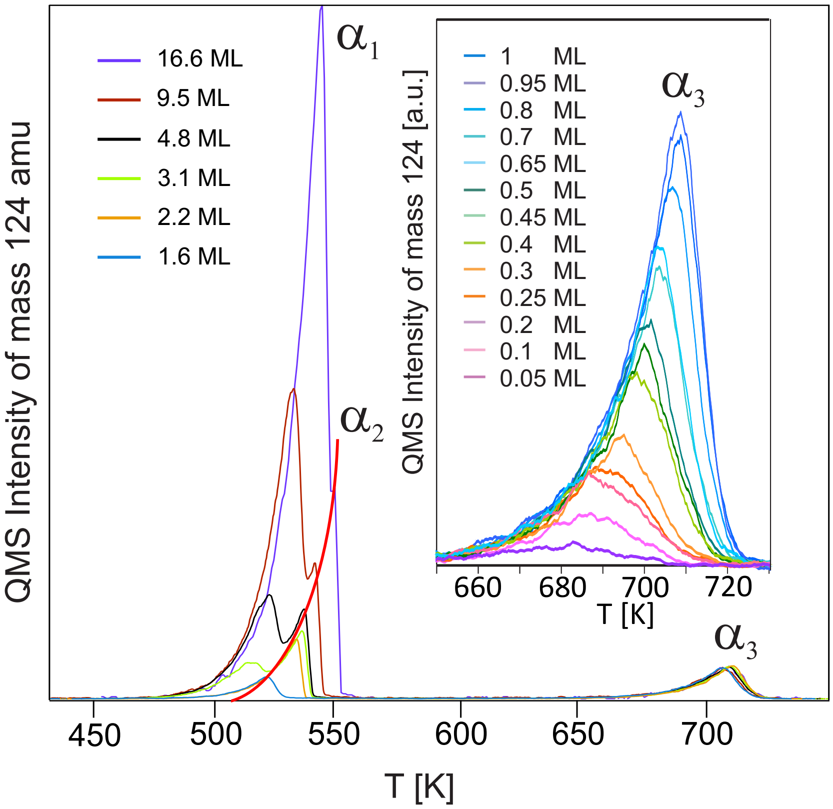

Figure 6.3: TPD data as a function of coverage. α_1 depicts the multilayer, α_2 the second layer and α_3 the monolayer. Evolution of peak α_2 is indicated as a guide to the eye (solid red line). Inset shows TPD dataset of peak α_3 for sub-monolayer coverages.

evolves which we assign, according to previously published data for PTCDA on Ag(111) [183], to the second ML of PTCDA. If the coverage is increased further the Tα_{2max} of α_2 settles at 545 K and the infinite increasing multilayer α_1 finally masks the second monolayer peak α_2 completely. In order to elucidate the binding energy of PTCDA on Au(111) the complete analysis was applied. This approach was found to be the most reliable method yielding the most accurate result with the least amount of assumptions necessary [195]. The complete analysis is based on the Polanyi-Wigner equation shown in (6.1) [60] and gives the relation of the rate of desorption dθ/dt with the desorption energy E$_B(\theta)$. With $\nu(\theta_0)$ the pre-exponential factor, n the order of desorption, θ_0 the initial coverage, k the Boltzmann constant and the temperature T.

$$d\theta/dt = -\nu(\theta_0)\theta_0^n exp(E_B(\theta_0)/kT) \tag{6.1}$$

The Polanyi-Wigner equation can be converted, if we assume that the coverage is constant $\theta = \theta_0$, into an Arrhenius like expression (6.2) of the type:

$$lnI_{QMS}(T) = -E_B(\theta_0)/kT + f(\theta_0) \tag{6.2}$$

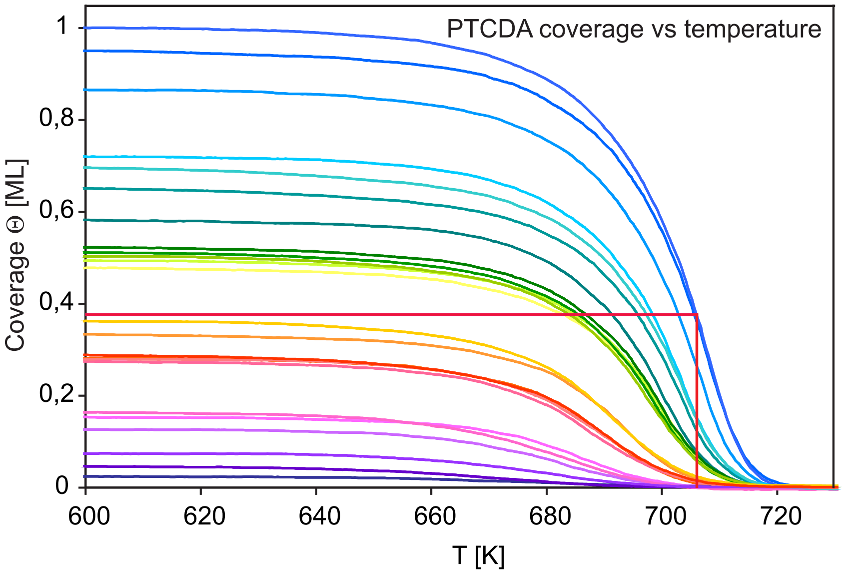

Figure 6.4: Normalized PTCDA coverage as a function of desorption temperature. Intersection line for evaluation is shown as well as a solid red line

The pre-exponential factor the order of desorption and the proportional dependence between the QMS signal intensity I_{QMS} and the desorption rate is contained in $f(\theta_0)$. In order to elucidate the binding energy from the TPD spectra, the spectra were integrated and normalized to 1 ML coverage. Figure 6.4 depicts the result of this procedure. When drawing intersection lines parallel to the x-axis (70 were used in this work) one receives data points at the crossing points yielding the temperature and the corresponding intensity of the QMS signal. The intensities, belonging to the intersection line were then printed in a logarithmic scale versus the reciprocal temperature yielding the Arrhenius like plots containing the binding energy as the slope of the resulting graph. The final result is shown in Figure 6.5. The inset shows one exemplary Arrhenius plot for 0.07 ML residual coverage which allows to calculate the binding energy from its slope. The binding energy increases with increasing coverage up to 0.3 ML this behavior can be explained by the formation of intermolecular hydrogenbonds between the PTCDA molecules [178]. In order to obtain the binding energy in the limit of a single molecule a linear fit up to 0.3 ML coverage was used resulting in 1.93(±0.04) eV.

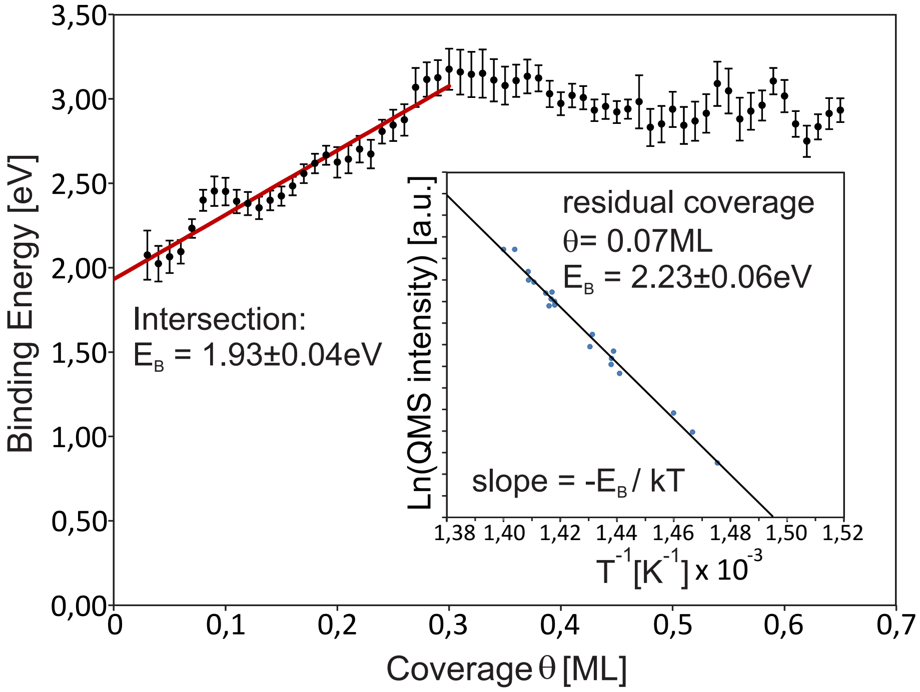

Figure 6.5: Binding energy of PTCDA as a function of coverage, solid red line represents extrapolation down to single molecule. Inset shows an exemplary Arrhenius plot for a 0.07 ML residual coverage.

There exists only few other experimental approaches for resolving the binding energy. Employing combined STM and frequency modulated atomic force microscopy equipped with a qPlus sensor Wagner *et al.* measured the junction stiffness while detaching and reclining a PTCDA molecule from the Au(111) surface. Since all interaction potentials amount to the bond strength and enough information can be retrieved in the measurements, the different possible bonding channels of the PTCDA Au(111) interaction is parameterized with generic potentials followed by a simulation of the junction stiffness based an these potentials. This simulation is then fitted to the experimental data allowing to extract the exact potential parameters, from which the intended values are calculated. Following this approach gives a binding energy of 2.5 eV upon lifting a single molecule from the Au(111) surface [196]. A different approach using high-resolution angle-resolved photoelectron spectroscopy (ARPES) in order to determine the binding strength of PTCDA on Au(111) was done by Ziroff *et al.* receiving a binding energy of 2.0 eV [197]. Theoretical studies employing the Perdew-Burke-Ernzerhof (PBE) and van der Waals(vdW) density functional (DF) self consistent field method (scf) obtained 1.88 eV or when using a classical potential approach 2.03 eV per molecule PTCDA on Au(111) [198]. Recently, Ruiz *et al.* reported a binding energy of 2.4 eV using a PBE vdW surface functional [199].

6.3 Electronic Properties

To gain more insights in the electronic properties of the different PTCDA coverages on the Au(111) substrate, we employed electronic HREELS with a primary electron

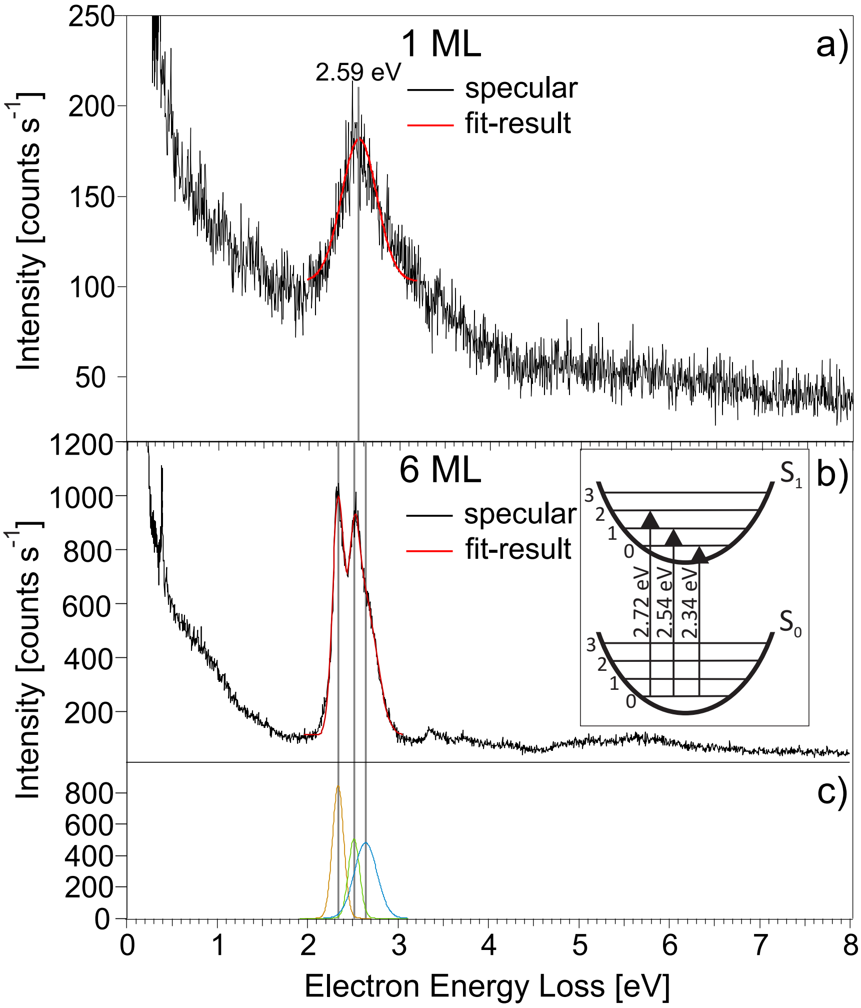

Figure 6.6: Electronic HREEL spectra for 1 ML a) and 6 ML b) PTCDA (black line) including the corresponding Gaussian peak fits (red line). Spectra have been measured with a pimary electron energy of E_0=15.5 eV in specular geometry. 6 ML spectra was fitted as indicated in c). The fit results unequivocally describes the measured data. Inset illustrates HOMO-LUMO (S_0-S_1) transition with vibronic components.

energy of 15.5 eV see Figure 6.6. The kinetic energy of the electrons is now sufficiently high enough to excite electronic transitions. See Table 6.2 for a summary of the observed electronic transitions. The transitions energies given are the result of the employed Gaussian fits and represent the peak maximum positions. Figure 6.6 a) shows the monolayer loss spectrum of PTCDA up to 8 eV. The specular spectrum (black line) exhibits one dominant feature, centered at 2.59 eV which we assign to the HOMO/LUMO-gap. This finding is in good agreement with previously published absorption data of the optical HOMO/LUMO gap of PTCDA on Au(111) of 2.6 eV [191]. In the 6 ML spectrum, shown in Figure 6.6 b), two strong features centered at

Table 6.2: Electronic transitions for 1 and 6 ML PTCDA. Peak positions are determined via the peak maximum of the employed Gaussian fit.

coverage	**electronic transition** [eV]
1 ML	2.59
6 ML	2.34, 2.54 and 2.72 3.37, 3.77, 4.20, 4.98 and 5.67

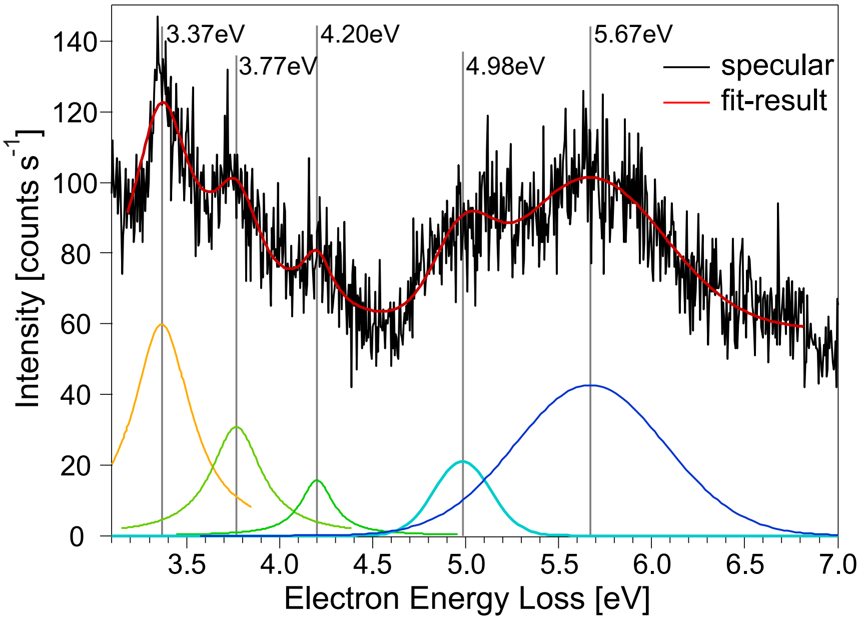

Figure 6.7: Close up view of the electronic HREEL spectra for 6 ML PTCDA (black line) in the range from 3 to 7 eV. Corresponding Gaussian fits are shown as well as the envelope of the fit-result (red line).

2.34 eV and at 2.54 eV are observed, the latter with a shoulder at the high energy side at 2.72 eV, the corresponding peak fit results are shown in Figure 6.6 c). In Figure 6.7 a zoom-in of the energy region between 3 and 7 eV is shown. Five electronic transitions are observed, located at 3.37, 3.77, 4.20, 4.98 and 5.67 eV respectively. The lowest energy feature at 2.34 eV can be assigned to the HOMO/LUMO (S_0-S_1) transition. The equal spacing between the signals at 2.34, 2.54 and 2.72 eV lead to the assumption that transitions into different vibronic states in the singlet S_1 band occur [200–203]. The loss features on the high energy side above 3 eV are as well found in UV/Vis absorption spectra of PTCDA nanoparticles [189] and transitions at 3.3 and 3.5 eV are observed in UV/Vis absorption spectra of 100nm thick layers of PTCDA on $\mathrm{Si}O_2$ [187]. We assign these to transitions between lower lying HOMO to higher LUMO.

6.4 Conclusions

Employing angular dependent HREELS and TPD spectroscopy we investigated the adsorption behavior and electronic properties of PTCDA on the Au(111) surface as a function of coverage. Furthermore we determine the binding energy of PTCDA on the gold substrate in the limit of a single molecule by means of the complete analysis approach for TPD data evaluation. Depending on the incident primary electron energy in HREELS, vibrational modes or electronic transition can be excited. Vibrational HREEL spectra reveal a planar adsorption geometry of PTCDA in the monolayer (ML) regime and a tilted orientation for higher coverages. Electronic HREEL spectra of 1 ML expose a gap between the highest occupied molecular orbital (HOMO) and the lowest unoccupied molecular orbital (LUMO) of 2.59 eV. For 6 ML coverage the HOMO/LUMO-gap is found at 2.34 eV with further vibronic transitions at 2.54 and 2.72 eV. On the high energy loss side, transitions from lower HOMO to higher LUMO are observed at 3.37, 3.77, 4.2, 4.98 and 5.67 eV, respectively. The bonding situation of PTCDA on the Au(111) surface is of rather physisorptive nature in contrast to other noble metal surfaces like Ag(111) and Cu(111). Thus, a determination of the binding energy via TPD is feasible and results in value of 1.93±0.04 eV in the limit of a single molecule PTCDA on Au(111).

Chapter 7

Di-Meta-Cyano-Azobenzene on Bi(111)

In the context of functional organic molecules, the group of molecular switches based on azobenzene undergoing a trans to cis isomerization is of great interest [29, 30]. For the pristine azobenzene molecule it is known that the reversible isomerization can be triggered in solution to the metastable cis conformation via illumination with ultraviolet light and back to the stable trans form by applying heat or shine visible light on the sample [31]. The mechanism of the trans to cis isomerization can follow two routes, namely through the inversion of one of the N-phenyl bonds or via a rotation around the N=N double bond. Investigation have been done to shine some light on the cis

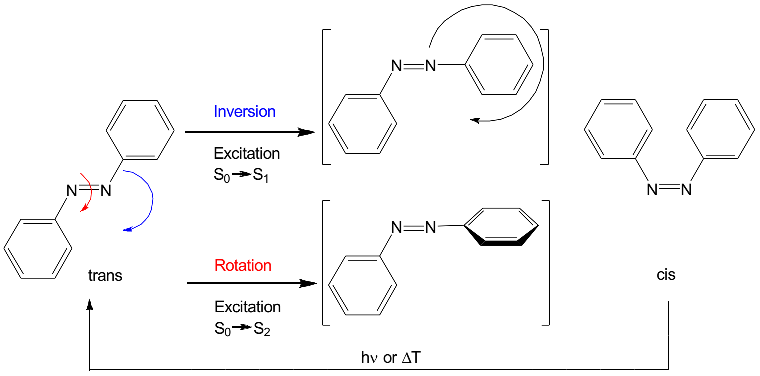

Figure 7.1: Trans to cis isomerization of azobenzenes via two possible excitation pathways as indicated. Scheme adapted from Reference [204].

to trans transition to elucidate the effect of different substituents and different substitution positions [205–208]. For the reaction in solution it was found that the nonbonding electron pair at the nitrogen can lead to a n $\rightarrow \pi^*$ transition ($S_0 \rightarrow S_1$) which results in an inversion at the nitrogen [209, 210]. The possible rotation pathway is induced via a $\pi \rightarrow \pi^*$ transition ($S_0 \rightarrow S_2$) [211, 212]. These findings are depicted in Figure 7.1. The photoisomerization capabilities of the molecular switches is usually quenched when the molecule is adsorbed on a metal surface which offers a problem for technology applications that needs to be overcome [213, 214]. This topic is addressed via different routes, for example it is attempted to lower the trans to cis barrier via substituting the parent azobenzene with one or more electron withdrawing or donating groups in different ring positions [215]. Previous studies of Di-Meta-Cyano-Azobenzene (DMC) on Au(111) reveal a very strong adsorbate substrate coupling leading to a suppression of the isomerization process [40, 216]. STM investigation of DMC on Cu(110) show a feasible trans to cis isomerization and reveal an almost covalent bonding situation among the DMC and the copper substrate thus rendering the switching process irreversible [37, 217]. Adsorbed on a Bi(111) substrate the photoinduced isomerization from trans to the cis form was feasible [101]. To reduce the metal molecule interaction different approaches were followed like the addition of bulky spacer groups to decouple the whole molecule from the substrate [41, 43–47], by attaching the molecular switches to spacer groups in self organizing frameworks (SAMs) [218–221] or by introducing isolating films between the molecular switch and the surface [222–224].

For further applications of the molecular switch DMC a profound knowledge of the initial adsorption geometry and electronic properties is of major importance. Details concerning the sample preparation and the employed dosage parameters are described in section 2.1.3 in the Experimental Details.

In this chapter we will show and discuss the findings of angular-dependent vibrational and electronic HREEL measurements and TPD spectroscopy of different coverages DMC on the Bi(111) surface.

7.1 Adsorption Geometry

In order to gain more insights in the adsorption and electronic properties of di-meta-cyano-azobenzene on Bi(111) we performed angular dependent HREEL and TPD spectroscopy ranging from the 1 ML to the 4 ML coverage regime.
As a first step to better understand the adsorption process of DMC on Bi(111) TPD spectra were measured for different initial coverages. Figure 7.2 shows an exemplary TPD spectrum of a 3 ML coverage DMC, the observed mass m = 102 amu is assigned to the $C_6H_4CN^+$ fragment of the parent molecule that corresponds to a phenyl ring with a cyano group attached to it. The heating rate during conducting the TPD experiments was set to $\beta = 1Ks^{-1}$. Two distinct peaks are observable in the spectrum. The assignment is identical to previously published data [101]. The low temperature peak, desorption starts at 291 K, with a maximum desorption temperature of 311 K (in the presented figure) grows infinitely with increasing coverage and the peak maximum slightly shifts towards higher desorption temperatures. These finding lead to the assignment of said peak to the multilayer α_1. The high temperature feature with a maximum desorption temperature of 321 K saturates and is therefore assigned to the monolayer coverage α_2.

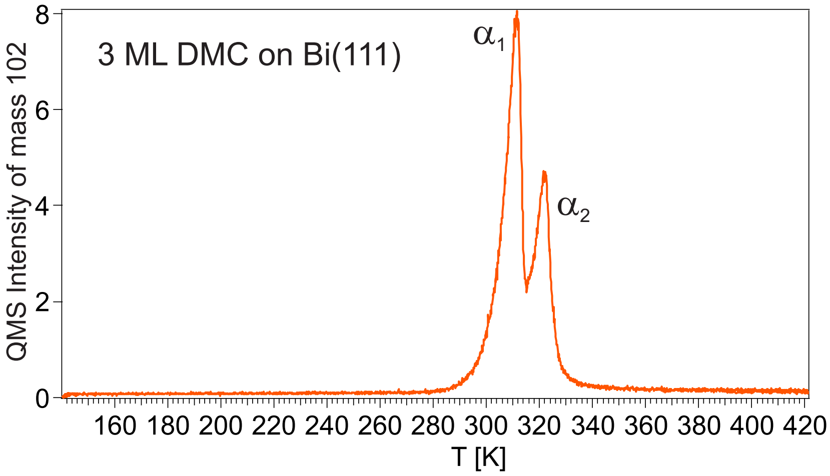

Figure 7.2: TPD spectrum of 3 ML DMC on Bi(111) recorded with a heating rate of $\beta = 1Ks^{-1}$. Observed mass fragment 102 amu is assigned to $C_6H_4CN^+$, a phenyl ring containing one cyano group. Peak α_1 denotes the multilayer, peak α_2 the monolayer.

The in specular and in 7°-off-specular (black line and red line respectively) geometry measured HREEL spectra of a 1 and 4 ML coverage is shown in Figure 7.3. The overall resolution measured as the full width at half maximum (FWHM) was 28 cm^{-1} (3.3

meV). The specular spectrum of the 1 ML coverage is shown in Figure 7.3 a). It is noteworthy that no vibrational modes originating from the cyano groups like $\nu_{C\equiv N}$ are observable in the spectrum. The strong background on the high loss energy side of the elastic peak originates from the bismuth phonon mode and can be seen more clearly in the HREEL spectra of a clean Bi(111) surface with different primary electron energies presented in Figure C.1 and Figure C.2 in Appendix C. Six distinguishable loss features are observed. See Table 7.1 for a detailed assignment of all observed loss features. At 160 cm^{-1} the out-of-plane bending mode originating from δ_{C-N} can be seen. Torsion modes arising from out-of-plane bending τ_{C-C} of the azobenzene core are found at 305 cm^{-1} and 693 cm^{-1} respectively. The latter containing a strong dipole activity. Dipole active features at 822 cm^{-1} and 902 cm^{-1} originate from out-of-plane bending modes from δ_{C-H} at the edges of the parent azobenzene core.

Observing only out-of-plane vibrational modes containing dipole activity lead to the conclusion that the DMC molecules in the 1 ML coverage regime adsorb in a planar geometry in their trans conformation with respect to the Bi(111) surface. In order to investigate the growth behavior exceeding the 1 ML regime HREEL measurements for a 4 ML coverage were conducted in specular and in 7°-off-specular (black line and red line respectively) geometry. The resulting angular dependant spectra are shown in Figure 7.3 b). The quenching of the bismuth phonon mode in this high coverage regime leads to a less pronounced background in the spectra and eight vibrational losses can

Table 7.1: Assignment of vibrational modes for 1 ML and 4 ML DMC coverage on Bi(111) as indicated. All vibrational frequencies are listed in cm^{-1}. IR/Raman data of azobenzene adapted from Ref. [225, 226]^{a}. Calculated data adapted from Ref. [227]^{b}. IR/Raman data for benzonitrile adapted from Ref. [228]^{c}. ν, indicates stretch; δ, bending; oop, out-of-plane; ip, in-plane. w, indicates weak; m, medium; s, strong; vs, very strong. A strong dipole activity is indicated by (da).

vibrational mode		**1 ML**	**4 ML**	**vib. data**
δ_{C-N}	oop	160s(da)	163vs(da)	219^{a}
τ_{C-C}, δ_{C-N}	oop	305w	303w	298^{b}
τ_{C-C}	oop	–	383vw	403^{a}
δ_{C-N}	oop	493m	488s	521^{a}
δ_{C-C}	oop	–	628vw	545^{a}
τ_{C-C}	oop	693vs(da)	688vs(da)	689^{a},688^{c}
δ_{C-H}, δ_{C-C}	oop	822s(da)	812s(da)	776^{a}
δ_{C-H}	oop	902m(da)	908m(da)	927^{a},922^{c}
$\nu_{C\equiv N}$	ip	–	–	2242^{c}

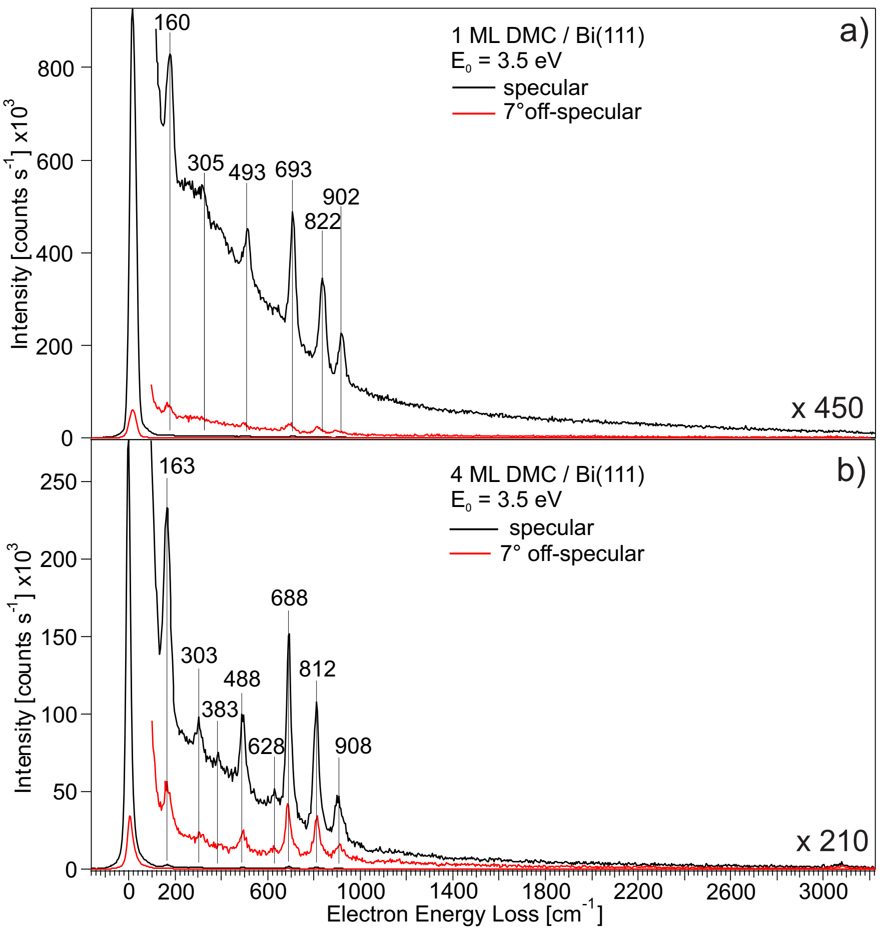

Figure 7.3: Vibrational HREEL spectrum measured with a primary electron energy of E_0=3.5 eV in specular (solid black line) and in 7°-off-specular geometry (solid red line) respectively of 1 (a) and 4 (b) ML DMC on Bi(111). The resolution (FWHM) for the specular geometry was in the range of 24 cm^{-1} (3 meV) and for the off-specular not higher than 32 cm^{-1} (4 meV).

be observed. The out-of-plane bending mode δ_{C-N} is now slightly shifted to 163 cm^{-1}. Vibrational losses arising from torsion modes of the carbon skeleton τ_{C-C} are found at 303 cm^{-1}, 383 cm^{-1} and at 688 cm^{-1} respectively. At 488 cm^{-1} the bending mode assigned to δ_{C-N} of the azobenzene is found. The out-of-plane bending modes originating from δ_{C-H} appear at 812 cm^{-1} and 908 cm^{-1} respectively. The difference in intensity of the specular and the off-specular spectra clearly confirms that all of the observed, out-of-plane vibrational modes contain at least some dipole activity. These findings point out that the planar adsorption geometry already seen for the 1 ML regime persists even for higher coverages at least up to 4 ML. The found layer by layer growth mode (Frank van der Merwe [229–231]) was recently also reported for DMC multilayers up to 4.7 ML coverage on Bi(111) employing Auger electron spectroscopy (AES) [232].

7.2 Electronic Properties

For a more advanced understanding of the molecular properties of DMC evaporated on Bi(111) we performed electronic HREEL spectroscopy with a primary electron energy of $E_0 = 15.5eV$. In this energy range excitation of electronic transitions is feasible.

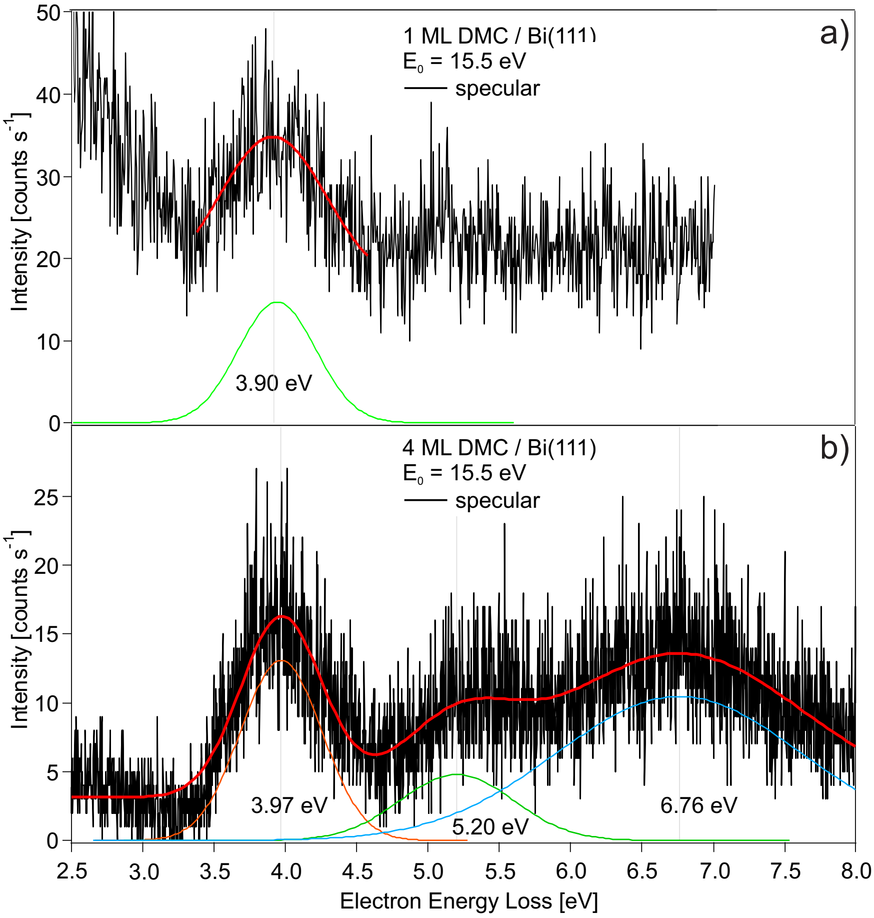

Figure 7.4: Electronic HREEL spectrum measured with a primary electron energy of E_0=15.5 eV in specular (solid black line) geometry of 1 ML a) and 4 ML b) DMC on Bi(111). The employed Gaussian fits are shown as well. The low loss side ranging up to 2.5 eV is omitted for clarity. The resolution (FWHM) for the specular geometry was 11 meV.

The specular HREEL spectrum of one and 4 ML DMC on Bi(111) is shown in Figure 7.4 (black line). The low loss energy side ranging from the elastic peak up to 2.5 eV, containing only vibrational contributions, is omitted for the sake of clarity. The employed Gaussian fits are depicted in the spectra as well as the resulting envelope (red line). See Table 7.2 for a list of the observed electronic transitions for 1 ML and 4 ML DMC on Bi(111). In the 1 ML coverage regime shown in 7.4 a) one electronic transition was observed located at 3.90 eV. We assign this feature to the HOMO/LUMO transition of the DMC molecule originating from the symmetry-allowed $\pi \rightarrow \pi^*$ (S_2) transition. The symmetry-forbidden n $\rightarrow \pi^*$ (S_1) transition and thus having much less intensity is usually contributing to absorption spectra in the energy region around 2.8 eV. In the HREEL measurements this transition could not be observed. The optical gap of 3.90 eV found in this work fits nicely to previously published data for the HOMO/LUMO gap ($\pi \rightarrow \pi^*$ transition), derived by mainly UV/vis spectroscopy, ranging from 3.40 eV up to 3.93 eV for differently substituted azobenzenes [42, 233–240]. The electronic HREEL spectrum for a 4 ML coverage DMC on Au(111) is shown in Figure 7.4 b). We observe three distinct features located at 3.97 eV, 5.20 eV and at 6.76 eV respectively. The first feature at 3.97 eV is assigned to the symmetry-allowed $\pi \rightarrow \pi^*$ (S_2) HOMO/LUMO transition of DMC (the symmetry-forbidden n $\rightarrow \pi^*$ (S_1) transition is not observed for the 4 ML coverage as well). The features at higher loss energies located at 5.20 eV and 6.67 eV are assigned to electronic transitions between lower lying HOMOs to higher lying LUMOs. Since conclusive data an the electronic structure of the azobenzene derivate DMC on Bi(111) is absent in literature so far, the findings for

Table 7.2: Electronic transitions for 1 and 4ML DMC on Bi(111). Peak positions are determined via the peak maximum of the employed Gaussian fit.

coverage	**electronic transition [eV]**
1 ML	3.90
4 ML	3.97, 5.20 and 6.76

tertbutyl-azobenzene (TBA) adsorbed on Au(111) will be taken into consideration. The different substituents e.g. cyano groups in meta-position versus tert-butyl groups in para position have a minor effect on the electronic structure of the molecule [215]. The differences in the considered substrates (Bi(111) and Au(111)) leading to varying degrees of level alignment of the molecular HOMO and LUMO orbitals with the substrates density of states upon adsorption can certainly not be neglected. For the TBA Au(111) system the proposed electronic structure for the trans- and cis-state including HOMO-1, HOMO, LUMO and LUMO+1 positions were determined by photoemission spectroscopy yielding conceivable excitation energies of 3.65 eV for the

HOMO/LUMO transition, 4.85 eV for a possible HOMO-1/LUMO transition and 6.6 eV for the HOMO/LUMO+1 transient [42]. This qualitatively comparison with the electronic transitions found by HREELS measurements in this work does not take into account if these suggested transitions are symmetry-allowed or forbidden furthermore for the comparison the origin of the electronic transition should result of a positive ion resonance since for the case of a negative ion resonance a strong shift of involved transition energies can be expected. Nevertheless the overall agreement of the in this work observed transitions compared to the TBA/Au(111) data is very astonishing.

7.3 Conclusions

Employing angular dependant vibrational and electronic HREEL spectroscopy and TPD measurements we investigated the adsorption behavior and the electronic properties of the molecular switch DMC on a Bi(111) surface. In the monolayer regime the molecules desorb with a maximin desorption temperature of 321 K from the Bi(111) surface. The in specular and off-specular geometry measured, vibrational HREEL spectra reveal that the molecules adsorb in a planar geometry,in its trans configuration with respect to the underlying substrate since only dipole active out-of-plane modes contribute to the spectra. When increasing the DMC coverage to 4 ML the planar adsorption geometry of the trans form persists and the observed vibrational, out-of-plane losses remain dipole active.

With a primary electron energy of $E_0 = 15.5$ eV electronic are excited and electronic transition can be measured as well. The 1 ML electronic HREEL spectrum (measured in specular geometry) reveals one electronic feature located at 3.90 eV and is assigned to the HOMO/LUMO transition of DMC which fits nicely to previous published data for the HOMO/LUMO gap of differently substituted azobenzene derivates reporting values from 3.40 eV to 3.93 eV [42, 233–240].

When the coverage is increased to 4 ML three electronic transitions can be observed in the electronic HREEL spectrum. These features are found at 3.97 eV, at 5.20 eV and at 6.76 eV respectively. The low loss energy feature located at 3.97 eV is assigned to the HOMO/LUMO transition of DMC. The electronic transitions found at 5.20 eV and at 6.76 eV are assigned to transitions between lower lying HOMO to LUMO and to HOMO to higher lying LUMO respectively.

Chapter 8

Nitro-Spiropyran on Bi(114)

A conclusive understanding of the switching capabilities of organic molecules adsorbed on different surfaces triggered by external incitements is required for further development of molecular devices that show promising properties for applications in data storage and sensor-like devices [241–244]. Molecular switches most often tend to lose their switching capability or at least the reversibility of the switching process when in contact with a metal surfaces [32–42]. Reasons for this can be found in steric hinderance (suppressing molecular rearrangement during switching) and in the electronic coupling of the adsorbate with the metallic substrate. Meaning that the lifetime of excited state, accountable for successful switching, is drastically reduced on metal surfaces [147, 245–250]. The photochromic 1,3,3-trimethylindolino-6-nitrobenzopyrylospiran (Nitro-Spiropyran, SP) is known to reversibly switch in solution from its three-dimensional,

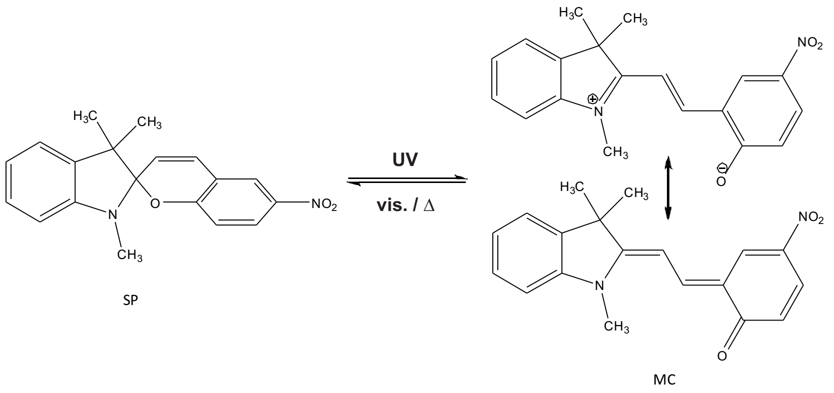

Figure 8.1: Structure of 3D nitrospiropyran molecule and its conversion into the planar merocyanine form.

colourless SP form to its planar, zwitterionic merocyanine (MC) form via cleavage of the central O-C-N bond. The ring-opening reaction can be induced by shining ultraviolett light on the sample and the backreaction is initiated via visible light or simple by temperature and is depicted in Figure 8.1 [251–254]. Among with the structural changes upon isomerization comes an enormous dipole moment change within the molecule which makes this system a very promising candidate for sensor like applications [255, 256], for molecular electronics [257–259] and for data storage devices [260–262]. Multilayers of Nitro-spiropyran adsorbed on a MgO(100) surface fully retain their photoisomerization ability and the ring-opening ring-closing reaction remains completely reversible [263]. From a combined scanning tunneling microscopy (STM), X-ray photoelectron spectroscopy (XPS), near-edge X-ray absorption fine structure spectroscopy (NEXAFS), and high-resolution electron energy loss spectroscopy (HREELS) study, the adsorption geometry of nitro-spiropyran on Au(111) is well known. Upon deposition of Nitro-spiropyran on the substrate the molecules form self-assembled islands and the molecules remain in their SP form. HREEL measurements reveal that the molecules adsorb with their indoline part perpendicular and the benzopyran unit parallel to the surface. A thermally induced isomerization from the closed SP form to the open MC form is reported for the monolayer regime. It was found that an inversion of the thermodynamically stability occurs which is due to the interaction of the planar, open MC form and the gold substrate and that the light induced reaction is inhibited [217]. In order to investigate the influence of the substrate on the quenching of the photoisomerization process a semimetallic surface, having a low density of states at the Fermi level, e.g. Bi(110) [58, 265] was chosen in another STM experimental approach. It was found that upon heating the sample to 350 K (monolayer regime), a complete transition towards the MC form is feasible. Illumination of the sample with a blue laser diode with a photon energy of $E_{ph} = 2.8$ eV ($\lambda = 445 nm,$)

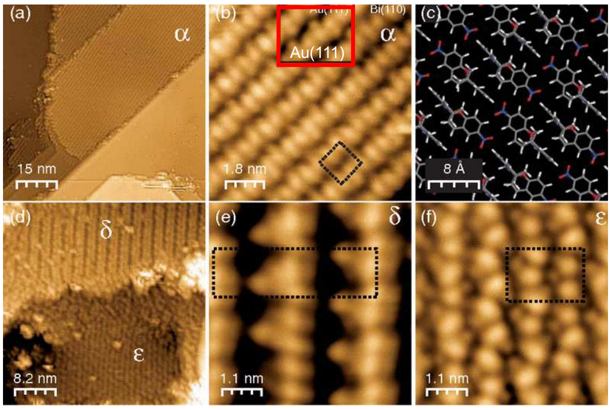

Figure 8.2: (a) STM image of nitro-Spiropyran islands on Bi(110) at RT and (b) its close-up. The inset shows a SP island obtained on Au(111), for comparison.(c) Ball-and-stick model of the SP island following force-field model simulations. (d) Overview image showing the coexistence of two molecular phases and after annealing the bismuth sample to 330 K. (e), (f) Zoomed image of the two different phases outlining their different molecular structures. Adapted from Ref. [264]

revealed that the photoisomerization capability is retained and MC formation is observed. For high Laser Fluences (above 3kJ/cm^2) a photostationary equilibrium state of SP:MC at high illumination intensities was found. Since no full transformation to the MC form could be achieved a back reaction to the SP form has to be taken into account. The bidirectionality of the isomerization process with monochromatic light is at first intriguing. By varying the photon energy for the illuminations (going from red-visible to UV range) it was found that conversion to the MC:SP mixed phase is independent of the photon energy used and thus in contrast to the results in solutions where switching is triggered by a specific wavelength (corresponding to the absorption transition). The bismuths narrow surface band is believed to play a crucial role. The continuum origin of electronic states allows for photon-activated transfer of electrons or holes, respectively in the molecular states, thus leading to the observed ring-opening / ring-closing with only one photon energy. The initial adsorption of the nitrospiropyran molecules on the Bi(110) surface, forming well ordered islands of the SP form, can be explained by the formation of π-H bonds and H bonds among the molecules and strongly resembles the behavior found on the Au(111) surface as shown in Figure 8.2 [264].

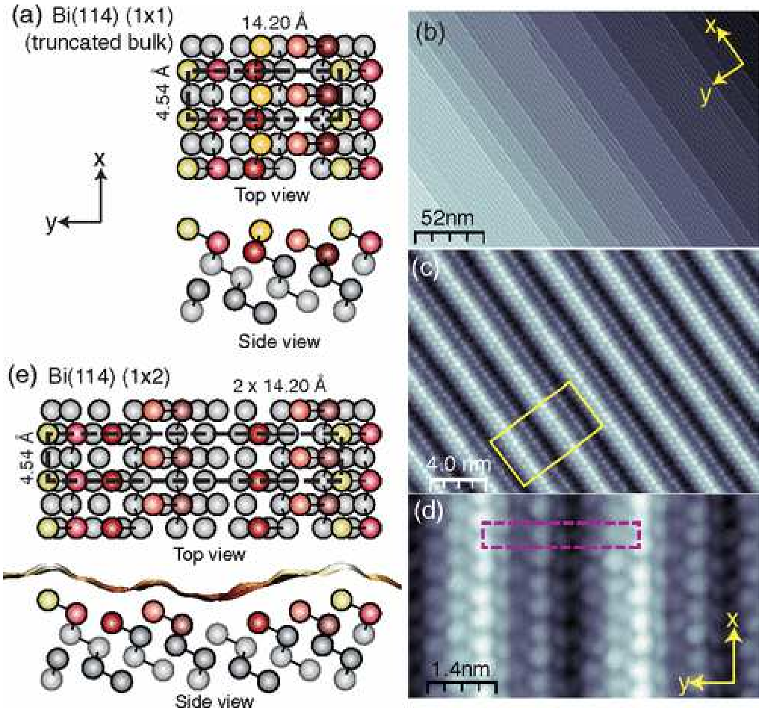

Figure 8.3: (a) Truncated bulk structure of Bi(114). (b-d) STM images with sample bias of 54 mV, -150 mV and -40 mV, respectively. (e) Top and side view of atomic model and the projected STM topography along x direction. Image adapted from Reference [57].

In Figure 8.3 STM images of the Bi(114) surface are shown. One can clearly observe the channel like appearance which is depicted in the projected STM topography. The Bi(114) surface shows some unique properties and a quasi-one-dimensional, metallic surface state was found on the semimetallic bulk in a STM study [57].

In the following chapter we investigate the influence of the substrate Bi(114) on the molecular switch nitro-spiropyran by means of TPD and HREEL measurements. Therefore we employed sub-ML and multilayer coverages of SP, evaporated on the Bi(114) surface. We investigated the thermally induced isomerization and the photoisomerization capabilities for different coverage regimes.

8.1 Adsorption Geometry of Nitro-Spiropyran on Bi(114)

To gain first informations about the studied system we performed TPD measurements for increasing initial coverages of nitro-spiropyran on the Bi(114) substrate. Figure 8.4 shows the TPD traces for different coverages. The observed mass = 144 amu is assigned to the fragment $[C_9H_6NO]^+$. The evaporation temperature in the homebuild effusion-cell evaporator was kept at 363 K and the sample temperature was kept at 120 K during deposition. For the HREEL measurement the sample was annealed at 240 K for 10 min to ensure a homogenous molecular surface. The TPD spectra in Figure 8.4 shows 2 distinct features. The peak labeled with α_1 shows an increasing intensity upon increasing coverage and is therefore assigned to the multilayer regime. With increasing coverage the intensity of the peak labeled α_2 saturates and a small shift of the maximum desorption temperature towards higher temperatures is observed and we assign this peak to a monolayer coverage. We will later show that this assignment will need some further investigations since a HREEL spectrum taken after a TPD measurement reaching 420 K of a multilayer coverage still shows the intact nitro-spiropyran molecules on the surface. Note that the sample temperature can not be increased further which is due

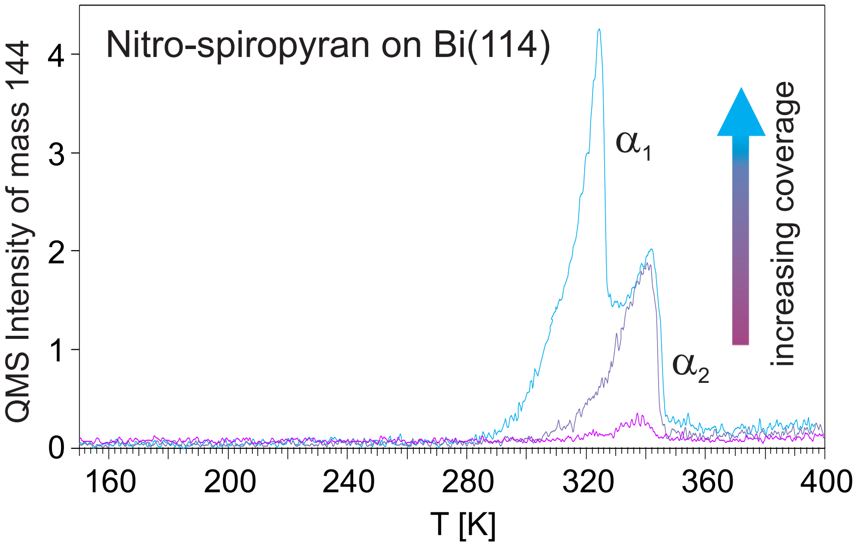

Figure 8.4: TPD spectra of different initial coverages of Nitro-spiropyran on Bi(114). The heating rate was $\beta = 1$ Ks^{-1}

.

to the rather low melting point of the bismuth sample (bismuth melts at 544 K at standard conditions). The HREEL spectrum is shown in Appendix D Figure D.1.
In Figure 8.5 the in specular and 7°-off-specular geometry measured HREEL spectra of a sub-monolayer in a) and a multilayer in b) coverage nitro-spiropyran on Bi(114) is shown. The specular spectra look very similar compared to HREEL spectra of nitro-spiropyran on Au(111) [217]. In Table 8.1 all observed vibrational features are assigned to their corresponding modes by employing IR data obtained by the references listed.

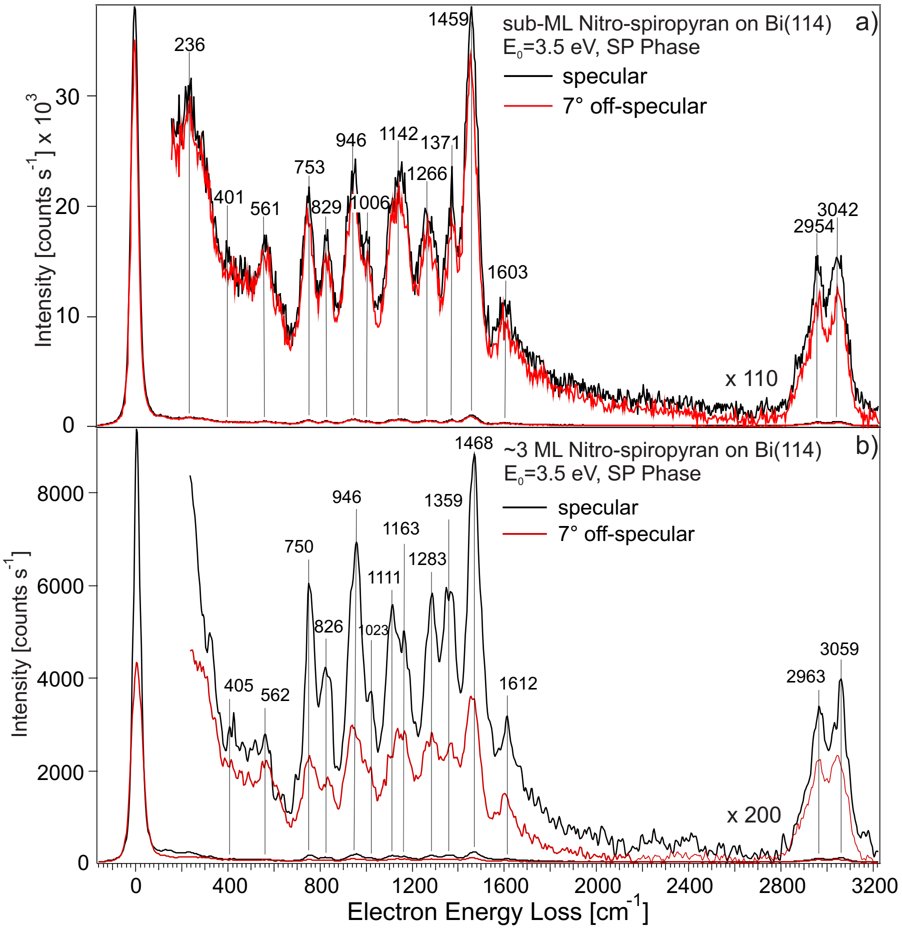

Figure 8.5: Vibrational HREEL spectrum measured with a primary electron energy of E_0=3.5 eV in specular (solid black line) and in 7°-off-specular geometry (solid red line) respectively of a sub-ML a) and a multilayer coverage nitro-spiropyran on Bi(114). The fwhm was better than 30 cm^{-1}.

As already stated in Ref. [217] two loss features assigned to the vibrational fingerprint of the ring-closed SP form can be found at 236 cm^{-1} and more intense at 946 cm^{-1}. The first arising from the butterfly torsion mode among the pyran and the phenyl rings and the latter from the O-C-N stretch vibration which can exclusively be observed in the closed spiropyran form. The sub-monolayer spectrum in Figure 8.5 a) shows 13 distinct vibrational feature. Besides the above mentioned two modes representative for the SP form we observe the C-C bending mode δ_{C-C} at 401 cm^{-1} and at 405 cm^{-1} in the multilayer, respectively. At around 562 cm^{-1} the torsion mode τ_{NO_2} appears in both spectra. The third "marker" vibrational mode for the in the following section discussed ring-opening reaction is found at 750 cm^{-1} and is assigned to the out-of-plane bending mode δ_{C-H}. This mode shows medium intensity in the SP phase (in Figure 8.5 a) and b)) and its intensity will strongly increase when the molecules isomerize to the planar, open merocyanine form as shown in Figure 8.6 which will be discussed later on.

Table 8.1: Assignment of vibrational modes for different phases on Bi(114). All vibrational frequencies are given in cm^{-1}. IR data of spiropyran adapted from Ref. [266–268] *a*. IR and Raman data of nitrobenzene adapted from Ref. [269, 270] *b*. IR and Raman data of benzopyren adapted from Ref. [271] *c*. ν, indicates stretch; δ, bending; τ, torsion; oop, out-of-plane; ip, in-plane. w, indicates weak; m, medium; s, strong; vs, very strong. A strong dipole activity is indicated by (da).

vibrational mode		**sub ML SP**	**3 ML SP**	**3 ML MC**	**spiropyran**[a]	**nitrobenzene** [b]	**benzopyran** [c]
τ_{butt},δ_{C-H},τ_{C-C}	oop	236s	–	–	–	–	269
δ_{C-C}	ip	401w	405w	–	–	392	–
τ_{C-C}	oop	–	–	478w	–	–	442
τ_{NO_2}	oop	561m	562m	551w	–	532	–
δ_{C-H}	oop	753s	750s	755vs(da)	748	–	740
δ_{C-H},τ_{C-C},ν_{C-C}	oop	829m	826m	835m	–	852	859
δ_{C-H}, δ_{C-C}	oop	–	–	923s	–	935	938
ν_{O-C-N}	oop	946s	946s(da)	–	954	–	–
δ_{C-C-N}	ip	1006w	1023w	–	1026	1021	–
δ_{C-H},ν_{C-C},	ip	–	1111w	1116m	1123	–	1118
δ_{C-H},ν_{C-C}	oop	1142s	1163s	–	–	1162	1158
ν_{C-N}	oop	1266m	1283s	1272m	1278	–	–
ν_{N-CH_3},δ_{C-C}	oop	1371m	1359s	1364m	–	–	1385
δ_{CH_3},ν_{C-C}	oop	1459vs	1468vs(da)	1464m	1466	1479	1464
ν_{C-C}	oop	1603w	1612w	1605w	–	1590	1606
ν_{C-H_3}	oop	2954m	2963m	2940m	2969	–	–
ν_{C-H}	ip	3042m	3059m	3064m	–	3082	3064

In the case of the multilayer coverage, this mode shows some dipole activity. Around 830 cm^{-1}, the spectra for both coverages show vibrational modes assigned to bending and torsion modes arising from δ_{C-H},τ_{C-C},ν_{C-C}. At 1266 cm^{-1} in the sub-ML spectrum and at 1283 cm^{-1} in the multilayer regime, respectively, the symmetric stretch vibration assigned to ν_{C-N} is observed and shows some dipole activity in the latter case. The intense stretching vibration mode of ν_{N-CH_3} in combination with ν_{C-C} is found at 1459 cm^{-1} (sub-ML) and at 1468 cm^{-1} (multilayer), respectively. This loss feature will as well show a drastic change upon the isomerization reaction, which will be discussed later. Stretching vibrations assigned to the carbon hydrogen of the methylenegroups, ν_{C-H_3}, are found at 2954 cm^{-1} (sub-ML) and 2963 cm^{-1} for the multilayer, respectively. At 3042 cm^{-1} (sub-ML) and 3059 cm^{-1} (multilayer) the stretching vibration of the aromatic hydrogens can be observed.

When comparing the HREEL spectra of the sub-ML and the multilayer coverage very striking difference meets the eye. In the case of the sub-ML the specular and the off-specular spectra show nearly the same intensity, a very unique finding. Since the dipole scattering mechanism is only valid for vibrations having a dipole moment change perpendicular with respect to the surface which is due to the image charge build up in the substrate we conclude that the molecules are embed in a substrate surrounding. When looking at the STM images of the Bi(114) surface (see Figure 8.3) one clearly sees channels continuing over the whole surface that are wide enough to fit a chain of SP molecules inside. From the HREEL spectrum of the sub-ML coverage we can definitively conclude that the nitro-spiropyran molecules adsorb in their ring-closed SP form since the fingerprint vibrational features are all observable, especially the existence of the O-C-N vibration ν_{O-C-N} at around 946 cm^{-1} is a strong evidence. The appearance of the C-N and the N-CH_3 stretching vibrations as well as the absence of stretch modes originating from the NO_2 (usually found at around 1336 cm^{-1} and 1515 cm^{-1}, respectively) group emphasizes that the molecules adsorb with their indoline part perpendicular and its benzopyran unit parallel to the surface. This finding is true for the multilayer regime as well and is in agreement to earlier published results of nitro-spiropyran adsorbed on Au(111) [217]. Interestingly, after performing a TPD experiment, starting from a multilayer coverage, the HREEL spectrum taken hereafter (see Appendix D Figure D.1) exactly resembles the spectrum for the sub-ML coverage shown in Figure 8.5 a). We thus conclude that the nitro-spiropyran molecules adsorbed inside the channels of the Bi(114) surface do not desorb and stay intact on the surface upon annealing of the sample to 420 K. The peak labeled α_2 in the TPD spectra in Figure 8.4 therefore does not represent the desorption of the complete monolayer. From the STM images of the Bi(114) surface showing the periodicity of the channels to occur at approximately every 3 nm we estimate the occupancy of the channels to be in the order of a third monolayer meaning that the α_2 peak represents the desorption of roughly 2/3 of a monolayer. In the next section we will show the drastic vibrational changes upon the ring-opening reaction to the MC form and show the thermally and light induced MC formation in the multilayer regime. In the sub-ML coverage, the molecules remain in their apparently more stable SP form and no ring-opening reaction could be triggered either via heating of the sample nor via illuminating the sample with varying laser wavelength.

8.2 Ring-Opening isomerization reactions

8.2.1 Vibrational changes upon isomerization

The conversion from the 3-dimensional SP form to the ring-opened, planar merocyanine from is accompanied by drastic changes in the vibrational HREEL spectra. In Figure 8.6 the in specular and off-specular geometry measured spectra of a multilayer coverage of the MC phase nitro-spiropyran is shown after the thermally induced ring-opening reaction. The sample was therefore heated to 280 K for 15 minutes. See Table 8.1 for a complete assignment of all observed vibrational modes. As discussed in section 8.1 the fingerprint modes characterizing the successful phase conversion are tagged. The first striking difference between the multilayer SP and MC phase is the enormous increase in the intensity of the elastic peak (by a factor of 250) which is attributed to the fact that the planar MC form offers a much smoother surface for the electrons and diffuse scattering is largely reduced. This finding is very similar to the MC phase on Au(111) [217]. The out-of-plane bending mode of the aromatic carbon hydrogen bonds, δ_{C-H}, shows an increased intensity and a large dipole activity. The, for the SP phase characteristic, O-C-N stretching mode, found at 946 cm^{-1} is not observed anymore.

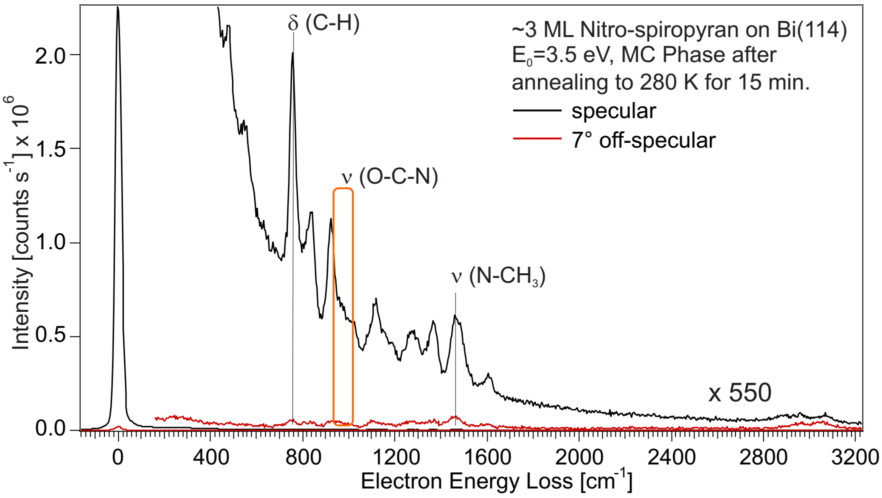

Figure 8.6: Vibrational HREEL spectrum measured with a primary electron energy of E$_0$=3.5 eV in specular (black line) and in 7°-off-specular geometry (red line), respectively, of a multilayer coverage nitrospiropyran in its MC form on Bi(114) after annealing the sample to 280 K for 15 minutes. The red rectangle highlights the switching marker namely the O-C-N vibrational mode.

These findings strongly correspond to the MC formation and we thus conclude that the observed vibrational features arise from the planar, ring-opened merocyanine form.

8.2.2 Thermally and Light induced isomerization

In order to investigate the thermally induced ring-opening reaction we evaporated multilayer coverages of SP molecules on the Bi(114) surface and annealed the sample at 240 K to ensure that it is homogenous. In Figure 8.7 a) the specular HREEL spectra during the SP to MC conversion are shown. Each spectrum is the result of a freshly prepared layer and was annealed to 280 K for 5, 10 and 15 min, respectively. It was found that no conversion to the planar MC form occurs when the sample is annealed for 30 minutes at 270 K and below. The temperature window for the isomerization process is very small and annealing of the sample at 280 K for 5 minutes leads almost to a complete conversion. For sub-ML coverages adsorbed on Au(111) the conversion takes place between 300 K and 330 K [217] and for Bi(110) the thermally induced isomerization was reported to be complete at around 350 K sample temperature [264].
To shine some light on the photoisomerization ability of nitro-spiropyran we prepared multilayer coverages of the SP form followed by annealing of the sample at 240 K to ensure well ordered SP phases. The prepared films of Sp were then exposed to laser light for 60 and 240 minutes, respectively and the resulting HREEL spectra are depicted in Figure 8.7 b). The used LASER source was a continous wave Laser diode with a photon energy of 2.8 eV (λ = 445 nm). The Laser spot was not focused and illuminated almost the whole sample from an angle of 45° (oval spot profile). The Laser power was 45 mW and we estimated the photon fluence to be 3.6 kJ/cm^2 (at maximum at the center of the spot) and the photon dose was estimated to 1.84x$10^{21}cm^{-2}$. During illumination the sample was held at 270 K, below the temperature for thermal isomerization. Again the intensity of the elastic peaks is increased but far less than compared to the thermally induced isomerization. The stretching mode of the O-C-N unit can still be seen as a shoulder at the higher loss energy side of the neighboring loss feature located at 923 cm^{-1} in the spectrum. No further changes can be observed if the illumination time is increased, we therefore conclude that the photoisomerization does not lead to a full conversion from SP to MC and that an equilibrium photostationary state is reached. The back reaction to the ring-closed SP form on the other hand was not feasible and was attempted via illumination with a Neodymium-doped Yttrium-Aluminium-Granate (Nd:YAG) -laser with its fundamental wavelength either doubled to hν = 532 nm (2.33 eV) or tripled to ν = 355 nm (3.49 eV). We conclude that the reaction is hindered most likely due to the fact the the ring-opened MC form exhibits strong intramolecular interaction which can be explained by their zwitterionic character

leading to a stabilized dimer network. Furthermore the lifetime of an excited molecular state is strongly reduced in the presence of a substrate (even in the investigated coverage regime) and thus results in the observed quenching of the ring-closing reaction. The findings for the ring-opening reaction are very similar to the Bi(110) results and are ascribed to a bidirectional isomerization process [264]. When the backreaction would be blocked a pure MC form would be received which is not the case. On the semimetallic Bi(110) the photoexcitations will show a longer lifetime since compared to a metallic surface a lower density of electrons or holes around the Fermi level that could possibly

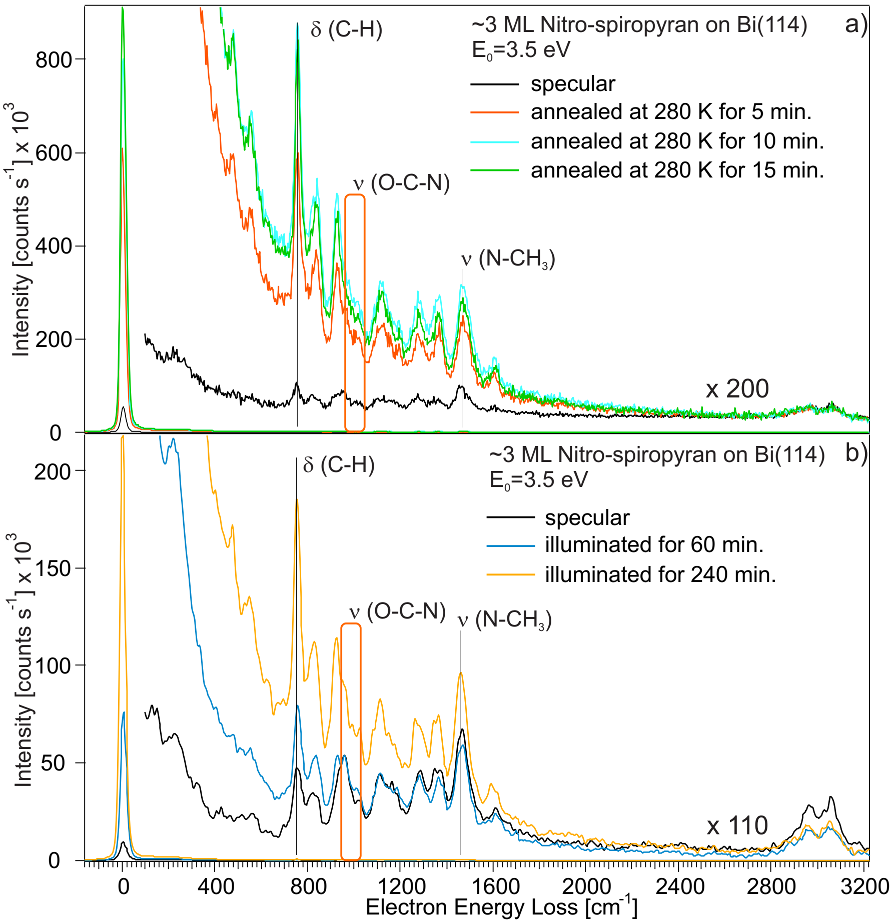

Figure 8.7: Specular vibrational HREEL spectra of the SP to MC conversion of a 3 ML coverage upon annealing the sample at 280 K in a). UV light induced isomerization employing a photon energy of 2.8 eV ($\lambda = 445$ nm) in b). The red rectangle marks the region of the O-C-N vibrational mode.

resonant couple to molecular, excited states, exist [213]. The used photon energy of the laser diode is much smaller than the optical gap of the nitro-spiropyran molecules (UV/vis data revealed transitions located at at 272 - 296 nm (4.55 - 4.18 eV) that is assigned to the $\pi - \pi^*$ electronic transition in the indoline part, and a feature arising at 323 - 351 nm (3.83 - 3.53 eV) which corresponds to the chromene moiety of the molecule [272]), thus this conversion can not be explained by a direct HOMO/LUMO transition. The metallic Bi(114) surface is most probably involved in the excitation reaction. The continuum of electronic states allows for photon-activated electron or hole injection into molecular states, driving the isomerization process [34].

8.3 Conclusions

Employing TPD and HREEL spectroscopy we investigated the adsorption properties and the isomerization capabilities of the molecular switch nitro-spiropyran on the Bi(114) surface. The Bi(114) substrate exhibits a quasi-one-dimensional metallic surface state on the semimetallic bulk and shows a channel-like surface topology with a periodicity of 3 nm [57].

The angular dependent HREEL spectra of a sub-ML nitro-spiropyran reveals the adsorption in the ring-closed SP form. Since the in specular and of–specular geometry measured HREEL spectra show almost identical intensities we conclude that in the sub-ML regime the moelecules adsorb in the channels on the Bi(114) surface, thus the surrounding substrate quenches dipole scattering via image charge formation. HREEL spectra taken after a TPD experiment, where a sample temperature of 420 K was reached, reveal that molecules stay intact on the surface and remain in their SP form. Isomerization was not feasible in the sub-ML regime neither thermally nor photon induced.

Multilayer HREEL spectra reveal that the nitro-spiropyran molecules in this coverage regime are still in the SP form and that the molecules adsorb with their indoline part perpendicular and its benzopyran unit parallel to the surface. The SP form remains stable up to a sample temperature of 270 K. When the sample is heated at 280 K for 5 minutes one yields the ring-open, planar MC form exclusively. Illumination of a multilayer with a cw Laser diode ($E_{h\nu} = 2.8$ eV, $\lambda = 445$ nm) yields a SP:MC mixture and after 240 minutes illumination time no further changes are observed in the spectra. A photoinduced ring-closing reaction could not be observed.

It is attributed to the unique surface of Bi(114) that a quenching of the isomerization process in the sub-ML regime is observed whereas we successfully show the thermal and light induced ring-opening reaction for the multilayer coverage.

Chapter 9

Summary

This thesis focuses on the investigation of functional organic molecules adsorbed on metal or semi-metal substrates by means of vibrational spectroscopy. Within this thesis six different adsorbate/substrate systems have been shown in detail. To gain a more comprehensive insight in the adsorption geometries and the electronic properties of the investigated molecule substrate systems was the main goal of this work. The experimental method of choice was the high resolution electron energy loss spectroscopy (HREELS) that proves to be the ideal tool to observe initial adsorption properties and changes in molecular orientation and furthermore is capable to directly measure electronic transitions.

In the first part we investigated the bottom up fabrication processes of graphen nanoribbons starting from a pristine carbon precursor molecule 6,11-dibromo-1,2,3,4-tetraphenyl-triphenylene and two nitrogen doped derivatives by means of TPD, vibrational and electronic HREEL spectroscopy.

The monomer phases reveal a planar adsorption geometry of the triphenylene core of the molecules while the attached four aromatic six membered rings (benzene or benzene and pyridine in combination) show a strong deviation from the molecular plane due to steric hinderance. The rather crowded vibrational spectra gets much less complex after the final annealing step to 710 K when cyclodehydrogenation occurs and only out-of-plane bending modes from C-H and C-C-C remain in the spectra depicting the now overall planar configuration of the graphen nanoribbon. Electronic HREEL spectra reveal the band gaps of the 3 different nanoribbons to be in the range of 2.8 eV. The doping effect on the gap size in the singly nitrogen doped GNR is negligible and only in the doubly nitrogen doped GNR a small shift of the gap of 100 meV towards a smaller gap size is observed. In addition to the HREELs measurements ultra-violett photoelectron spectroscopy (UPS) experiments were performed by Christopher Bronner in in our group and we found that the band gap is shifted relative to the electronic structure of the gold substrate.

The bottom up fabrication process for graphene nanoribbons is feasible with the chosen precursor molecules and yields precise GNR. HREEL spectroscopy is able to directly measure the HOMO-LUMO band gap of GNR on the chosen Au(111) substrate.

In the next part we investigated the adsorption behavior and electronic properties of 1,3,8,10-Tetraazaperopyren and its two derivates 2,9-bisperfluoro-propyl-1,3,8,10-tetraazaperopyren and the halogenated species 2,9-bisperfluoropropyl-4,7,11,14-tetrachloro-1,3,8,10-tetraazaperopyren on a Au(111) substrate for different coverages. We found that the TAPP molecules adsorb in a planar fashion with respect to the substrate, this behavior persists during further adsorption and only a slightly roughening of the surface can be observed for higher coverages. The fluorinated derivatives show an reorientation of their side chains for higher coverages converging towards the trans geometry found in the crystal. When using sufficiently high enough primary electron energies in HREEL, electronic transitions can be excited as well. The electronic HREEL spectra of the different TAPP precursor molecules reveal their optical gaps which fit nicely to published data. Furthermore we found evidence for an adatom complex in which gold atoms mediated by the substrate bond to the TAPP molecules.

In conclusion it can be stated that in the monolayer regime a planar adsorption geometry with respect to the substrate is favoured. For higher coverages the substituents in 2 and 9 position govern the further molecular orientation. When no substituents are present the planar motif persists. With the fluorinated propyl chains attached the molecular orientation approaches the trans configuration as seen in the bulk crystal structure. Furthermore it was found that the core substitution of the tetraazaperopyrenes with halogens (electron withdrawing groups) alters its electronic properties and a decrease of the HOMO-LUMO gap size results.

In the following part we investigated the adsorption properties of α-octithiophene molecules evaporated on a Au(111) for increasing coverages up to 1 ML. We found that in the sub-ML regime the 8T molecules adapt a planar orientation with respect to the substrate, when the coverage reaches approxamitely 1 ML we found that the molecules adapt a tilted orientation along its long molecular axis with respect to the surface. In the sub-monolayer regime the molecule/substrate interaction, like molecule π-system overlapping with density of states (dos) of the metal, dominate and define the adsorption geometry. When reaching a certain coverage threshold, repulsion between the nearest neighboring molecules lead to a reorientation and the former planar adsorbate begins to tilt its molecular plane and intermolecular interaction like π-π stacking between the octithiophenes becomes dominant.

Next we investigated the adsorption properties of PTCDA molecules on the Au(111) substrate. We found a planar adsorption geometry of PTCDA in the monolayer (ML) regime and a slightly tilted orientation for higher coverage phases. Electronic HREEL spectra of 1 ML expose a gap between the highest occupied molecular orbital (HOMO) and the lowest unoccupied molecular orbital (LUMO) of 2.59 eV. For higher coverages the HOMO/LUMO-gap is found at 2.34 eV and we observe further vibronic transitions at 2.54 and 2.72 eV. On the high energy loss side, transitions from lower HOMO to higher LUMO are observed at 3.37, 3.77, 4.2, 4.98 and 5.67 eV, respectively. Furthermore we determine the binding energy of PTCDA on the gold substrate in the limit of a single molecule by means of the complete analysis approach for TPD data evaluation and found a value of 1.93±0.04 eV.

Now we investigated the adsorption and electronic properties of the potential molecular switch DMC on a Bi(111) surface. We found that the molecules adsorb in a planar geometry,in its trans configuration with respect to the substrate, with increasing coverage the planar adsorption geometry of the trans form persists at least up to 4 ML. Furthermore we found electronic features for the 1 ML coverage located at 3.90 eV which we assigned to the HOMO/LUMO of DMC. Its value fits nicely to previous published data for the HOMO/LUMO gap of differently substituted azobenzene derivates. For higher coverages three electronic transitions were observed and we assign them to the HOMO/LUMO transition and to transitions between lower lying HOMO to LUMO and to HOMO to higher lying LUMO respectively. Finally we investigated the adsorption properties and the isomerization capabilities of the molecular switch nitro-spiropyran on the Bi(114) surface. The Bi(114) substrate exhibits a quasi-one-dimensional metallic surface state on the semimetallic bulk and shows a channel-like surface topology. The angular dependent HREEL spectra in the sub-ML coverage regime reveals the adsorption in the ring-closed SP form. The in specular and of–specular geometry measured HREEL spectra show almost identical intensities we thus conclude that in the sub-ML regime the moelecules adsorb in the channels on the Bi(114) surface, thus the surrounding substrate quenches dipole scattering via image charge formation. The SP molecules stay intact on the surface up to sample temperature of 420 K and remain in their SP form. Isomerization was not feasible in the sub-ML regime neither thermally nor photon induced.

Nevertheless we found that for multilayer coverages the molecules remain in the SP form and that the molecules adsorb with their indoline part perpendicular and its chromene unit parallel to the surface. The SP form is stable up to 270 K. The ring-opening reaction in this coverage regime could be induced when heating the sample to 280 K for 5 minutes and yields the ring-open, planar MC form exclusively. When a multilayer is illuminated with a cw Laser diode ($E_{h\nu} = 2.8$ eV, $\lambda = 445$ nm) for 240 minutes illumination time we observe a SP:MC mixture and no further changes are observed for longer illuminations times. A photoinduced ring-closing reaction could not be observed which is most probably due to the MC MC interaction forming stable dimer networks. The fact that no isomerisation is observed for the sub-ML coverage we attribute to the unique surface of Bi(114) quenching of the isomerization process. We successfully show the thermal and light induced ring-opening reaction for the multilayer coverage.

In Summary we gained insight into the adsorption properties regarding molecule/substrate-interactions and molecule/molecule-interactions. It is not surprising that such interactions govern the geometry and electronic properties of the molecule substrate system. It was found that the orientation and electronic structure of the investigated system in detail the moleculesubstrate complex must be taken into consideration for the successful design of devices in the field of organic electronics.

Appendix A

GNR

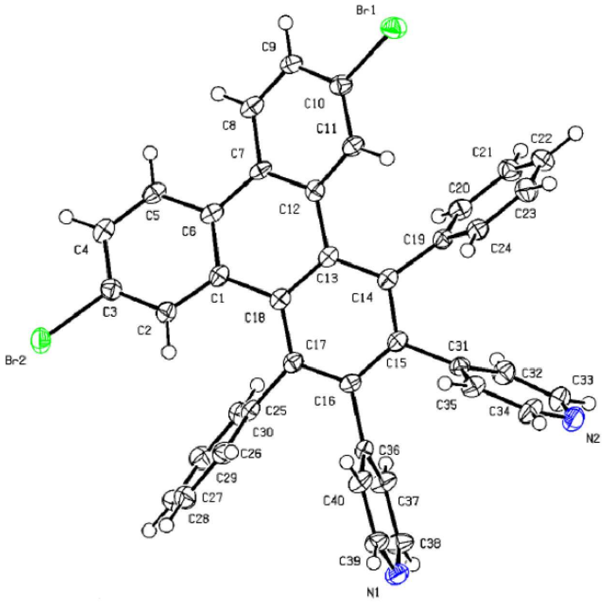

Figure A.1: Ortep plot of the 2N-GNR, 4,4-(6,11-Dibromo-1,4-diphenyltriphenylene-2,3-diyl)dipyridine precursor molecule obtained via single crystal X-ray structure analysis adapted from suppl. informations of Ref. [101]. A co-crystallized THF molecule is omitted for clarity. The molecule crystallizes in the monoclinic P $2_1/_c$ space group with four molecules per unit cell. The deviation of the two benzene and two pyridine rings respectively from the planar triphenylene core in a propeller like shape can be observed.

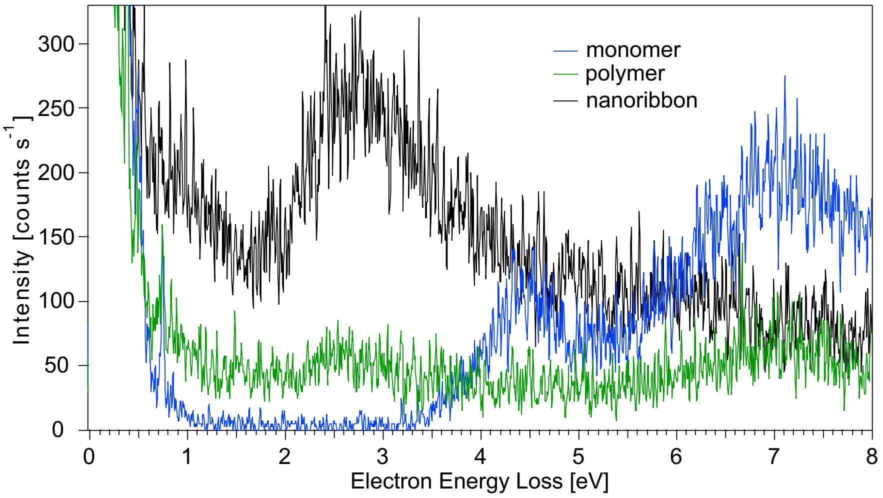

Figure A.2: Electronic HREEL spectra of the GNR fabrication process originating from the monomer 6,11-dibromo-1,2,3,4-tetraphenyl-triphenylene. All spectra were measured with a primary electron energy of $E_0 = 15.5eV$ in specular geometry on Au(111). The different molecular phases depicted are the monomer precursor (blue line), the polymer phase (green line) and the GNR phase(black line) are plotted in one graph for ease of comparison.

Appendix B

TAPP

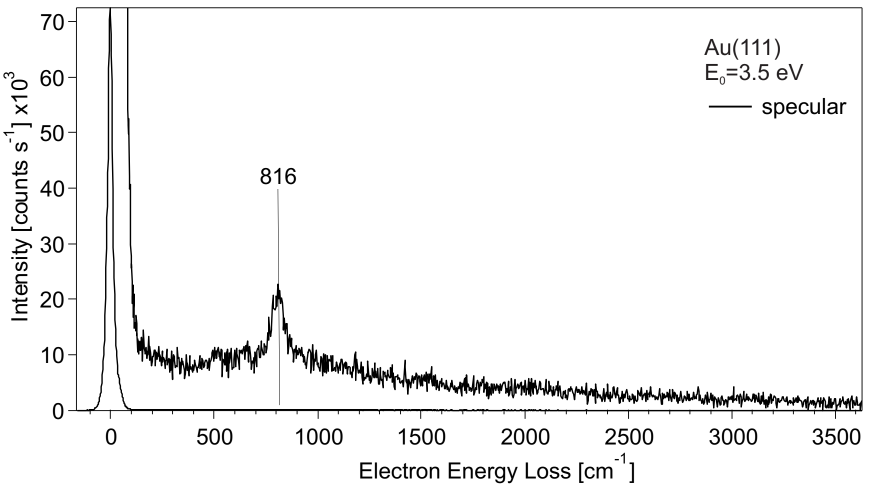

Figure B.1: Vibrational HREEL spectrum in specular geometry measured with a primary electron energy of E_0=3.5 eV of residual TAPP molecule fragments on Au(111) after full TPD up to T=800 K.

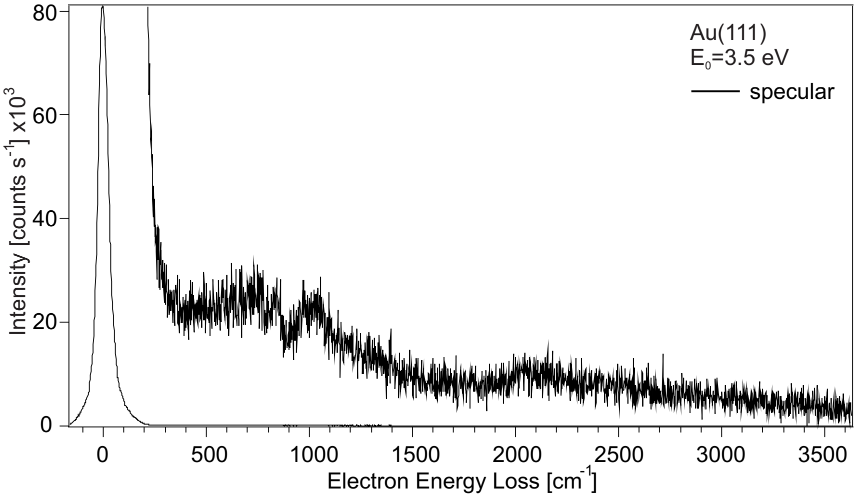

Figure B.2: Vibrational HREEL spectrum in specular geometry measured with a primary electron energy of E_0=3.5 eV of residual TAPP-$(C_3F_7)_2$ molecule fragments on Au(111) after full TPD up to T=900 K.

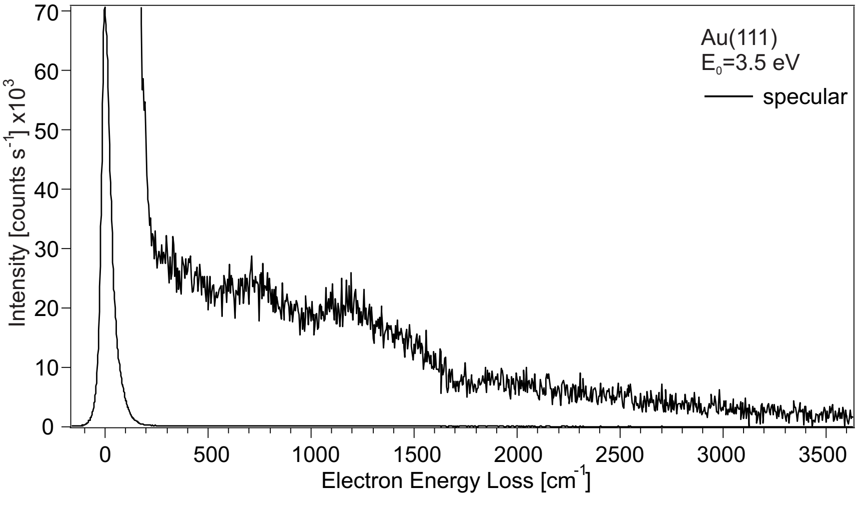

Figure B.3: Vibrational HREEL spectrum in specular geometry measured with a primary electron energy of E_0=3.5 eV of residual TAPP-$Cl_4(C_3F_7)_2$ molecule fragments on Au(111) after full TPD up to T=900 K.

Appendix C

DMC Bi(111)

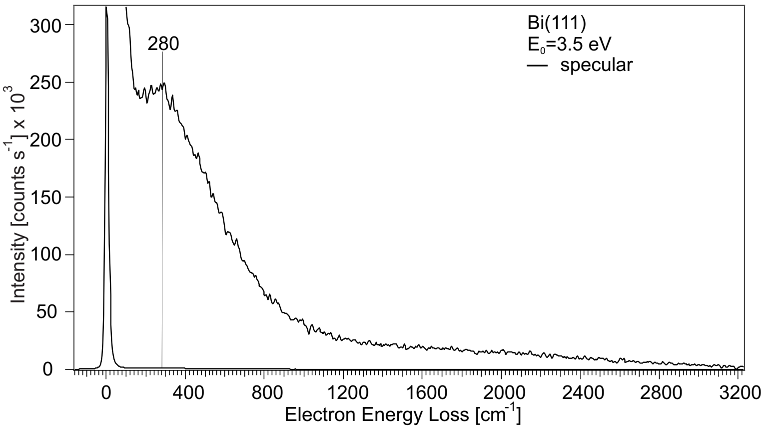

Figure C.1: Vibrational HREEL spectrum of clean Bi(111) showing the Bismuth phonon mode, measured with a primary electron energy of E_0= 3.5 eV.

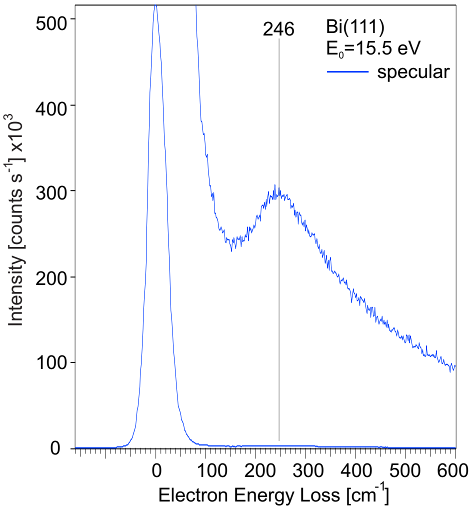

Figure C.2: HREEL spectrum of Bi(111) phonon mode measured with a primary electron energy of E_0= 15.5 eV.

Appendix D

Nitro-Spiro on Bi(114)

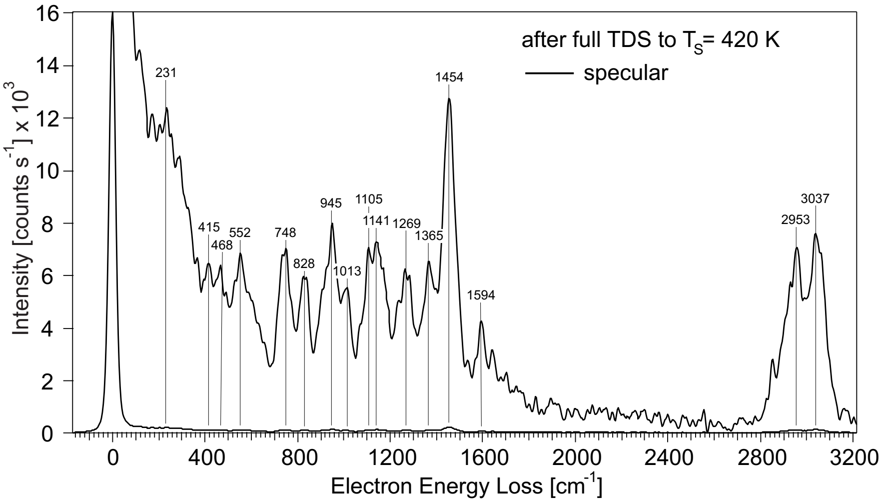

Figure D.1: Specular vibrational HREEL spectrum taken after a full TPD up to 420 K, one can clearly observe all vibrational modes that belong to intact SP molecules on the surface.

Bibliography

[1] H. Klauk, *Organic Electronics.* Weinheim, FRG: Wiley-VCH Verlag GmbH & Co. KGaA, May 2006.

[2] S. Allard, M. Forster, B. Souharce, H. Thiem, and U. Scherf, "Organic semiconductors for solution-processable field-effect transistors (OFETs).," *Angew. Chem. (Int. ed. Engl.)*, vol. 47, pp. 4070–98, Jan. 2008.

[3] D. Braga and G. Horowitz, "High-Performance Organic Field-Effect Transistors," *Adv. Mat.*, vol. 21, pp. 1473–1486, Apr. 2009.

[4] H. E. Katz and J. Huang, "Thin-Film Organic Electronic Devices," *A. Rev. Mat. Res.*, vol. 39, pp. 71–92, Aug. 2009.

[5] H. Usta, C. Risko, Z. Wang, H. Huang, M. K. Deliomeroglu, A. Zhukhovitskiy, A. Facchetti, and T. J. Marks, "Design, synthesis, and characterization of ladder-type molecules and polymers. Air-stable, solution-processable n-channel and ambipolar semiconductors for thin-film transistors via experiment and theory.," *J. Am. Chem. Soc.*, vol. 131, pp. 5586–608, Apr. 2009.

[6] F. Würthner and K. Meerholz, "Systems chemistry approach in organic photovoltaics.," *Chemistry*, vol. 16, pp. 9366–73, Aug. 2010.

[7] X. Guo, R. P. Ortiz, Y. Zheng, Y. Hu, Y.-Y. Noh, K.-J. Baeg, A. Facchetti, and T. J. Marks, "Bithiophene-imide-based polymeric semiconductors for field-effect transistors: synthesis, structure-property correlations, charge carrier polarity, and device stability.," *J. Am. Chem. Soc.*, vol. 133, pp. 1405–18, Feb. 2011.

[8] M. M. Ling and Z. Bao, "Thin Film Deposition, Patterning, and Printing in Organic Thin Film Transistors," *Chem. Mater.*, pp. 4824–4840, 2004.

[9] C. R. Newman, C. D. Frisbie, A. Demetrio, S. Filho, and J.-l. Bre, “Introduction to Organic Thin Film Transistors and Design of n-Channel Organic Semiconductors,” *Chem. Mater.*, pp. 4436–4451, 2004.

[10] L. Schmidt-Mende, a. Fechtenkötter, K. Müllen, E. Moons, R. H. Friend, and J. D. MacKenzie, “Self-organized discotic liquid crystals for high-efficiency organic photovoltaics.,” *Science (New York, N.Y.)*, vol. 293, pp. 1119–22, Aug. 2001.

[11] F. Würthner and R. Schmidt, “Electronic and crystal engineering of acenes for solution-processible self-assembling organic semiconductors.,” *Chemphyschem*, vol. 7, pp. 793–7, Apr. 2006.

[12] J. E. Anthony, “Functionalized acenes and heteroacenes for organic electronics.,” *Chem. Rev.*, vol. 106, pp. 5028–48, Dec. 2006.

[13] A. W. Hains, Z. Liang, M. a. Woodhouse, and B. a. Gregg, “Molecular semiconductors in organic photovoltaic cells.,” *Chem. Rev.*, vol. 110, pp. 6689–735, Nov. 2010.

[14] D. S. Weiss and M. Abkowitz, “Advances in organic photoconductor technology.,” *Chem. Rev.*, vol. 110, pp. 479–526, Jan. 2010.

[15] F. Würthner, “KunststoffTransistoren werden reif für Massenanwendungen in der Mikroelektronik,” *Angew. Chem.*, pp. 1069–1071, 2001.

[16] H. Klauk, “Organic thin-film transistors.,” *Chem. Soc. Rev.*, vol. 39, pp. 2643–66, July 2010.

[17] H. Usta, A. Facchetti, and T. J. Marks, “n-Channel semiconductor materials design for organic complementary circuits.,” *Acc. Chem. Res.*, vol. 44, pp. 501–10, July 2011.

[18] X. Zhan, A. Facchetti, S. Barlow, T. J. Marks, M. a. Ratner, M. R. Wasielewski, and S. R. Marder, “Rylene and related diimides for organic electronics.,” *Adv. Mat.*, vol. 23, pp. 268–84, Jan. 2011.

[19] E. Menard, M. a. Meitl, Y. Sun, J.-U. Park, D. J.-L. Shir, Y.-S. Nam, S. Jeon, and J. a. Rogers, “Micro- and nanopatterning techniques for organic electronic and optoelectronic systems.,” *Chem. Rev.*, vol. 107, pp. 1117–60, Apr. 2007.

[20] C. Dimitrakopoulos and P. Malenfant, “Organic Thin Film Transistors for Large Area Electronics,” *Adv. Mat.*, vol. 14, pp. 99–117, Jan. 2002.

[21] R. D. Boer, “Organic single-crystal field-effect transistors,” *Materials Today*, vol. 10, no. 3, pp. 20–27, 2004.

[22] F. Schwierz, “Graphene transistors.,” *Nature Nano.*, vol. 5, pp. 487–96, July 2010.

[23] R. Chau, B. Doyle, S. Datta, J. Kavalieros, and K. Zhang, “Integrated nanoelectronics for the future.,” *Nature Mat.*, vol. 6, pp. 810–2, Nov. 2007.

[24] J. Anthony, “Höhere Acene: vielseitige organische Halbleiter,” *Angew. Chem.*, vol. 120, pp. 460–492, Jan. 2008.

[25] P. Gao, D. Beckmann, H. N. Tsao, X. Feng, V. Enkelmann, M. Baumgarten, W. Pisula, and K. Müllen, “Dithieno[2,3- d ;2,3- d]benzo[1,2- b ;4,5- b]dithiophene (DTBDT) as Semiconductor for High-Performance, Solution-Processed Organic Field-Effect Transistors,” *Adv. Mat.*, vol. 21, pp. 213–216, Jan. 2009.

[26] M. Halik, H. Klauk, U. Zschieschang, G. Schmid, S. Ponomarenko, S. Kirchmeyer, and W. Weber, “Relationship Between Molecular Structure and Electrical Performance of Oligothiophene Organic Thin Film Transistors,” *Adv. Mat.*, vol. 15, pp. 917–922, June 2003.

[27] S. Subramanian, S. K. Park, S. R. Parkin, V. Podzorov, T. N. Jackson, and J. E. Anthony, “Chromophore fluorination enhances crystallization and stability of soluble anthradithiophene semiconductors.,” *J. Am. Chem. Soc.*, vol. 130, pp. 2706–7, Mar. 2008.

[28] M. Tang and A. Reichardt, “Trialkylsilylethynyl-functionalized tetraceno thiophene and anthra thiophene organic transistors,” *Chem. Mater.*, no. 6, pp. 4669–4676, 2008.

[29] S. Venkataramani and U. Jana, “Magnetic bistability of molecules in homogeneous solution at room temperature,” *Science*, vol. 331, pp. 445–8, Jan. 2011.

[30] K. Ichimura, S. Oh, and M. Nakagawa, “Light-driven motion of liquids on a photoresponsive surface,” *Science*, vol. 288, pp. 1624–1626, June 2000.

[31] B. Feringa and W. Browne, *Molecular switches.* Weinheim, Germany: Wiley-VCH Verlag GmbH & Co. KGaA, July 2001.

[32] L. Ovári, Y. Luo, F. Leyssner, R. Haag, M. Wolf, and P. Tegeder, “Adsorption and switching properties of a N-benzylideneaniline based molecular switch on a Au(111) surface.,” *J. Chem. Phys.*, vol. 133, p. 044707, July 2010.

[33] F. Leyssner, S. Hagen, J. D. S. P. Ovári, L, H. S. Peters, Maike V., T. Klamroth, and P. Tegeder, "Photoisomerization ability of molecular switches adsorbed on Au (111): comparison between azobenzene and stilbene derivatives," *J. Phys. Chem. C*, no. 111, pp. 1231–1239, 2009.

[34] M. Wolf and P. Tegeder, "Reversible molecular switching at a metal surface: A case study of tetra-tert-butyl-azobenzene on Au(111)," *Surf. Sci.*, vol. 603, pp. 1506–1517, June 2009.

[35] X. Wang, Y. Ouyang, X. Li, H. Wang, J. Guo, and H. Dai, "Room-Temperature All-Semiconducting Sub-10-nm Graphene Nanoribbon Field-Effect Transistors," *Phys. Rev. Lett.*, vol. 100, p. 206803, May 2008.

[36] M. Alemani, S. Selvanathan, F. Ample, M. V. Peters, K.-H. Rieder, F. Moresco, C. Joachim, S. Hecht, and L. Grill, "Adsorption and Switching Properties of Azobenzene Derivatives on Different Noble Metal Surfaces: Au(111), Cu(111), and Au(100)," *J. Phys. Chem. C*, vol. 112, pp. 10509–10514, July 2008.

[37] N. Henningsen, R. Rurali, K. J. Franke, I. Fernández-Torrente, and J. I. Pascual, "Trans to cis isomerization of an azobenzene derivative onaCu(100) surface," *Appl. Phys. A*, vol. 93, pp. 241–246, Aug. 2008.

[38] L. Óvári, J. Schwarz, M. V. Peters, S. Hecht, M. Wolf, and P. Tegeder, "Reversible isomerization of an azobenzene derivative adsorbed on Au(111): Analysis using vibrational spectroscopy," *Int. J. Mass Spec.*, vol. 277, pp. 223–228, Nov. 2008.

[39] J. Henzl, T. Bredow, and K. Morgenstern, "Irreversible isomerization of the azobenzene derivate Methyl Orange on Au(111)," *Chem. Phys. Lett.*, vol. 435, pp. 278–282, Feb. 2007.

[40] N. Henningsen and K. Franke, "Inducing the rotation of a single phenyl ring with tunneling electrons," *J. Phys. Chem. C*, pp. 14843–14848, 2007.

[41] P. Tegeder, S. Hagen, F. Leyssner, M. Peters, S. Hecht, T. Klamroth, P. Saalfrank, and M. Wolf, "Electronic structure of the molecular switch tetra-tert-butyl-azobenzene adsorbed on Ag(111)," *Appl. Phys. A*, vol. 88, pp. 465–472, June 2007.

[42] S. Hagen, P. Kate, F. Leyssner, D. Nandi, M. Wolf, and P. Tegeder, "Excitation mechanism in the photoisomerization of a surface-bound azobenzene derivative: Role of the metallic substrate.," *J. Chem. Phys.*, vol. 129, p. 164102, Oct. 2008.

[43] F. Moresco, G. Meyer, K. Rieder, and H. Tang, “Conformational changes of single molecules induced by scanning tunneling microscopy manipulation: A route to molecular switching,” *Phys. Rev. Lett.*, vol. 86, pp. 672–675, Jan. 2001.

[44] T. Jung, R. Schlittler, and J. Gimzewski, “Conformational identification of individual adsorbed molecules with the STM,” *Lett. to Nature*, 1997.

[45] E. McNellis, G. Mercurio, and S. Hagen, “Bulky spacer groupsA valid strategy to control the coupling of functional molecules to surfaces?,” *Chem. Phys. Lett.*, vol. 499, pp. 247–249, Oct. 2010.

[46] M. Corno, A. Rimola, V. Bolis, and P. Ugliengo, “Hydroxyapatite as a key biomaterial: quantum-mechanical simulation of its surfaces in interaction with biomolecules,” *Phys. Chem. Chem. Phys.*, vol. 12, pp. 6309–29, June 2010.

[47] D. N. M. W. P. T. Sebastian Hagen, Felix Leyssner, “Reversible switching of tetra- tert-butyl-azobenzene on a Au (111) surface induced by light and thermal activation,” *Chem. Phys. Lett.*, vol. 444, pp. 85–90, Aug. 2007.

[48] F. Leyß ner, “Analysis of Functional Organic Molecules at Noble Metal Surfaces by Means of Vibrational Spectroscopies,” 2011.

[49] H. Ibach, D. Mills, and H. Ibach, “Electron energy loss spectroscopy and surface vibrations,” 1982.

[50] M. Henzler and W. Göpel, “Oberflächenphysik des Festkörpers,” *Oberflächenphysik des Festkörpers*, 1994.

[51] SPECS, “Delta 0.5 HREEL spectrometer,”

[52] P. a. Thiry, M. Liehr, J. J. Pireaux, and R. Caudano, “Electron Interaction Mechanisms in High Resolution Electron Energy Loss Spectroscopy,” *Phys. Scri.*, vol. 35, pp. 368–379, Mar. 1987.

[53] M. Rocca, “Low-energy EELS investigation of surface electronic excitations on metals,” *Surf. Sci. Rep.*, vol. 22, pp. 1–71, Jan. 1995.

[54] F. Maaß, “Untersuchung des Adsorptionsverhaltens und der elektronischen Eigenschaften organischer Halbleitermaterialien auf der Au(111) Oberflche,” 2014.

[55] S. Park and R. Palmer, “Plasmon Dispersion of the Au (111) Surface with and without Self-Assembled Monolayers,” *Physical review letters*, vol. 102, p. 216805, May 2009.

[56] S. Park and R. Palmer, “Acoustic plasmon on the Au (111) surface,” *Physical review letters*, vol. 105, p. 016801, July 2010.

[57] J. Wells, J. Dil, F. Meier, J. Lobo-Checa, V. Petrov, J. Osterwalder, M. Ugeda, I. Fernandez-Torrente, J. Pascual, E. Rienks, M. Jensen, and P. Hofmann, “Nondegenerate Metallic States on Bi(114): A One-Dimensional Topological Metal,” *Phys. Rev. Lett.*, vol. 102, p. 096802, Mar. 2009.

[58] S. Agergaard and C. Sø ndergaard, “The effect of reduced dimensionality on a semimetal: the electronic structure of the Bi (110) surface,” *J. Phys.*, vol. 15, 2001.

[59] R. Musket and W. McLean, “Preparation of atomically clean surfaces of selected elements: a review,” *Appl. Surf. Sci.*, vol. 10, pp. 143–207, 1982.

[60] K. Christmann, “Introduction to surface physical chemistry,” 1991.

[61] F. Neese, “Orca a dft and semiempirical scf-mo package,” 2011.

[62] F. Jensen, *Introduction to computational chemistry.* 2007.

[63] P. Hohenberg and W. Kohn, “Inhomogeneous electron gas,” *Phys. Rev.*, vol. 155, no. 1962, 1964.

[64] P. Loewdin, “Density functional theory,” *Int. J. Quant. Chem.*, 1986.

[65] M. Born and R. Oppenheimer, “Zur quantentheorie der molekeln,” *Annalen der Physik*, 1927.

[66] W. Kohn and L. Sham, “Self-consistent equations including exchange and correlation effects,” *Physical Review*, vol. 385, no. 1951, 1965.

[67] K. S. Novoselov, a. K. Geim, S. V. Morozov, D. Jiang, Y. Zhang, S. V. Dubonos, I. V. Grigorieva, and a. a. Firsov, “Electric field effect in atomically thin carbon films.,” *Science*, vol. 306, pp. 666–9, Oct. 2004.

[68] K. S. Novoselov, a. K. Geim, S. V. Morozov, D. Jiang, M. I. Katsnelson, I. V. Grigorieva, S. V. Dubonos, and a. a. Firsov, “Two-dimensional gas of massless Dirac fermions in graphene.,” *Nature*, vol. 438, pp. 197–200, Nov. 2005.

[69] C. Soldano, A. Mahmood, and E. Dujardin, “Production, properties and potential of graphene,” *Carbon*, vol. 48, pp. 2127–2150, July 2010.

[70] M. Terrones, A. R. Botello-Méndez, J. Campos-Delgado, F. López-Urías, Y. I. Vega-Cantú, F. J. Rodríguez-Macías, A. L. Elías, E. Muñoz Sandoval, A. G. Cano-Márquez, and J.-C. Charlier, "Graphene and graphite nanoribbons: Morphology, properties, synthesis, defects and applications," *Nano Today*, vol. 5, pp. 351–372, Aug. 2010.

[71] X. Li, X. Wang, L. Zhang, S. Lee, and H. Dai, "Chemically derived, ultrasmooth graphene nanoribbon semiconductors.," *Science.*, vol. 319, pp. 1229–32, Feb. 2008.

[72] L. Liao, J. Bai, Y. Qu, Y.-c. Lin, Y. Li, Y. Huang, and X. Duan, "High-kappa oxide nanoribbons as gate dielectrics for high mobility top-gated graphene transistors.," *PNAS*, vol. 107, pp. 6711–5, Apr. 2010.

[73] I. Meric, M. Y. Han, A. F. Young, B. Ozyilmaz, P. Kim, and K. L. Shepard, "Current saturation in zero-bandgap, top-gated graphene field-effect transistors.," *Nature Nano.*, vol. 3, pp. 654–9, Nov. 2008.

[74] F. Xia, D. B. Farmer, Y.-M. Lin, and P. Avouris, "Graphene field-effect transistors with high on/off current ratio and large transport band gap at room temperature.," *Nano Lett.*, vol. 10, pp. 715–8, Feb. 2010.

[75] Y. Zhang, T.-T. Tang, C. Girit, Z. Hao, M. C. Martin, A. Zettl, M. F. Crommie, Y. R. Shen, and F. Wang, "Direct observation of a widely tunable bandgap in bilayer graphene.," *Nature*, vol. 459, pp. 820–3, June 2009.

[76] T. Ohta, A. Bostwick, T. Seyller, K. Horn, and E. Rotenberg, "Controlling the electronic structure of bilayer graphene.," *Science*, vol. 313, pp. 951–4, Aug. 2006.

[77] Z. H. Ni, T. Yu, Y. H. Lu, Y. Y. Wang, Y. P. Feng, and Z. X. Shen, "Uniaxial strain on graphene: Raman spectroscopy study and band-gap opening," *Am. Chem. Soc. Nano*, vol. 2, no. 11, pp. 2301–2305, 2008.

[78] T. Mohiuddin, a. Lombardo, R. Nair, a. Bonetti, G. Savini, R. Jalil, N. Bonini, D. Basko, C. Galiotis, N. Marzari, K. Novoselov, a. Geim, and a. Ferrari, "Uniaxial strain in graphene by Raman spectroscopy: G peak splitting, Grüneisen parameters, and sample orientation," *Phys. Rev. B*, vol. 79, p. 205433, May 2009.

[79] K. Nakada, M. Fujita, G. Dresselhaus, and M. Dresselhaus, "Edge state in graphene ribbons: Nanometer size effect and edge shape dependence.," *Phys. Rev. B, Cond. Matt.*, vol. 54, pp. 17954–17961, Dec. 1996.

[80] Y.-W. Son, M. L. Cohen, and S. G. Louie, “Energy Gaps in Graphene Nanoribbons,” *Phys. Rev. Lett.*, vol. 97, p. 216803, Nov. 2006.

[81] M. Han, B. Özyilmaz, Y. Zhang, and P. Kim, “Energy Band-Gap Engineering of Graphene Nanoribbons,” *Phys. Rev. Lett.*, vol. 98, p. 206805, May 2007.

[82] F. Cervantes-Sodi, G. Csányi, S. Piscanec, and a. Ferrari, “Edge-functionalized and substitutionally doped graphene nanoribbons: Electronic and spin properties,” *Phys. Rev. B*, vol. 77, p. 165427, Apr. 2008.

[83] S. Braun, W. R. Salaneck, and M. Fahlman, “Energy-Level Alignment at Organic/Metal and Organic/Organic Interfaces,” *Adv. Mat.*, vol. 21, pp. 1450–1472, Apr. 2009.

[84] I. G. Hill, a. Rajagopal, a. Kahn, and Y. Hu, “Molecular level alignment at organic semiconductor-metal interfaces,” *Appl. Phys. Lett.*, vol. 73, no. 5, p. 662, 1998.

[85] D. Wei, Y. Liu, Y. Wang, H. Zhang, L. Huang, and G. Yu, “Synthesis of N-doped graphene by chemical vapor deposition and its electrical properties.,” *Nano Lett.*, vol. 9, pp. 1752–8, May 2009.

[86] H. Wang, T. Maiyalagan, and X. Wang, “Review on Recent Progress in Nitrogen-Doped Graphene: Synthesis, Characterization, and Its Potential Applications,” *ACS Catalysis*, vol. 2, pp. 781–794, May 2012.

[87] X. Wang, X. Li, L. Zhang, Y. Yoon, P. K. Weber, H. Wang, J. Guo, and H. Dai, “N-doping of graphene through electrothermal reactions with ammonia.,” *Science*, vol. 324, pp. 768–71, May 2009.

[88] H. Terrones, R. Lv, M. Terrones, and M. S. Dresselhaus, “The role of defects and doping in 2D graphene sheets and 1D nanoribbons.,” *Rep. Prog. Phys. Phys. Soc.*, vol. 75, p. 062501, June 2012.

[89] a. Fasoli, a. Colli, a. Lombardo, and a. C. Ferrari, “Fabrication of graphene nanoribbons via nanowire lithography,” *Phys. Stat. Sol. (B)*, vol. 246, pp. 2514–2517, Dec. 2009.

[90] S. Ryu, J. Maultzsch, M. Y. Han, P. Kim, and L. E. Brus, “Raman spectroscopy of lithographically patterned graphene nanoribbons.,” *ACS Nano*, vol. 5, pp. 4123–30, May 2011.

[91] J. G. Son, M. Son, K.-J. Moon, B. H. Lee, J.-M. Myoung, M. S. Strano, M.-H. Ham, and C. a. Ross, “Sub-10 nm Graphene Nanoribbon Array field-effect transistors fabricated by block copolymer lithography.,” *Adv. Mat.*, vol. 25, pp. 4723–8, Sept. 2013.

[92] L. Tapasztó, G. Dobrik, P. Lambin, and L. P. Biró, “Tailoring the atomic structure of graphene nanoribbons by scanning tunnelling microscope lithography.,” *Nature Nano.*, vol. 3, pp. 397–401, July 2008.

[93] D. V. Kosynkin, A. L. Higginbotham, A. Sinitskii, J. R. Lomeda, A. Dimiev, B. K. Price, and J. M. Tour, “Longitudinal unzipping of carbon nanotubes to form graphene nanoribbons.,” *Nature*, vol. 458, pp. 872–6, Apr. 2009.

[94] L. Jiao, L. Zhang, X. Wang, G. Diankov, and H. Dai, “Narrow graphene nanoribbons from carbon nanotubes.,” *Nature*, vol. 458, pp. 877–80, Apr. 2009.

[95] F. Cataldo, G. Compagnini, G. Patané, O. Ursini, G. Angelini, P. R. Ribic, G. Margaritondo, A. Cricenti, G. Palleschi, and F. Valentini, “Graphene nanoribbons produced by the oxidative unzipping of single-wall carbon nanotubes,” *Carbon*, vol. 48, pp. 2596–2602, Aug. 2010.

[96] I. Janowska, O. Ersen, T. Jacob, P. Vennégues, D. Bégin, M.-J. Ledoux, and C. Pham-Huu, “Catalytic unzipping of carbon nanotubes to few-layer graphene sheets under microwaves irradiation,” *Appl. Catal. A: Gen.*, vol. 371, pp. 22–30, Dec. 2009.

[97] Q. Peng, Y. Li, X. He, X. Gui, Y. Shang, C. Wang, C. Wang, W. Zhao, S. Du, E. Shi, P. Li, D. Wu, and A. Cao, “Graphene nanoribbon aerogels unzipped from carbon nanotube sponges.,” *Adv. Mat.*, vol. 26, pp. 3241–7, May 2014.

[98] L. Xie, H. Wang, C. Jin, X. Wang, L. Jiao, K. Suenaga, and H. Dai, “Graphene nanoribbons from unzipped carbon nanotubes: atomic structures, Raman spectroscopy, and electrical properties.,” *J. Am. Chem. Soc.*, vol. 133, pp. 10394–7, July 2011.

[99] J. Cai, P. Ruffieux, R. Jaafar, M. Bieri, T. Braun, S. Blankenburg, M. Muoth, A. P. Seitsonen, M. Saleh, X. Feng, K. Müllen, and R. Fasel, “Atomically precise bottom-up fabrication of graphene nanoribbons.,” *Nature*, vol. 466, pp. 470–3, July 2010.

[100] L. Grill, M. Dyer, L. Lafferentz, M. Persson, M. V. Peters, and S. Hecht, “Nanoarchitectures by covalent assembly of molecular building blocks.,” *Nature Nano.*, vol. 2, pp. 687–91, Nov. 2007.

[101] C. Bronner, B. Priewisch, K. Rük-Braun, and P. Tegeder, “Photoisomerization of an Azobenzene on the Bi (111) Surface,” *J. Phys. Chem.*, no. 111, 2013.

[102] C. Bronner, F. Leyssner, S. Stremlau, M. Utecht, P. Saalfrank, T. Klamroth, and P. Tegeder, “Electronic structure of a subnanometer wide bottom-up fabricated graphene nanoribbon: End states, band gap, and dispersion,” *Phys. Rev. B*, vol. 86, p. 085444, Aug. 2012.

[103] K. Merkel and A. Kocot, “Density Functional Theory Studies on Ir Spectra of the Triphenylene Derivatives. A Scaled Quantum Mechanical Force Field Approach,” *Acta Phys. Pol. A*, vol. 98, no. 5, pp. 525–531, 2000.

[104] V. Schettino, “Infrared and Raman spectra of crystalline triphenylene and triphenylene- d 12 and normal coordinates calculations,” *J. Mol. Spec.*, vol. 96, 1970.

[105] L. Colangeli and V. Mennella, “Raman and infrared spectra of polycyclic aromatic hydrocarbon molecules of possible astrophysical interest,” *Astrophys. J.*, 1992.

[106] C. D. Keefe, L. a. Donovan, and S. D. Fleet, “Vibrational Assignment and Dipole Moment Derivatives of Liquid Bromobenzene at 25 C,” *J. Phys. Chem. A*, vol. 103, pp. 6420–6428, Aug. 1999.

[107] G. Shakila, S. Periandy, and S. Ramalingam, “Molecular Structure and Vibrational Analysis of 1-Bromo-2-Chlorobenzene Using ab initio HF and Density Functional Theory (B3LYP) Calculations,” *J. Atom., Mol., Opt. Phys.*, vol. 2011, pp. 1–10, 2011.

[108] M. Kumar, M. Srivastava, and R. a. Yadav, “Vibrational studies of benzene, pyridine, pyridine-N-oxide and their cations.,” *Spectr. Acta. Part A, Mol. Biomol. Spec.*, vol. 111, pp. 242–51, July 2013.

[109] C. Bronner, S. Stremlau, M. Gille, F. Brauß e, A. Haase, S. Hecht, and P. Tegeder, “Aligning the band gap of graphene nanoribbons by monomer doping.,” *Angew. Chem. (Int. ed. Engl.)*, vol. 52, pp. 4422–5, Apr. 2013.

[110] M. Saleh, M. Baumgarten, A. Mavrinskiy, T. Schafer, and K. Mullen, “Triphenylene-Based Polymers for Blue Polymeric Light Emitting Diodes,” *Macromolecules*, vol. 43, pp. 137–143, Jan. 2010.

[111] S. Linden, D. Zhong, a. Timmer, N. Aghdassi, J. H. Franke, H. Zhang, X. Feng, K. Müllen, H. Fuchs, L. Chi, and H. Zacharias, “Electronic Structure of Spatially Aligned Graphene Nanoribbons on Au(788),” *Phys. Rev. Lett.*, vol. 108, p. 216801, May 2012.

[112] U. Müllen, Klaus; Scherf, *Organic Light Emittinng Devices.* 2005.

[113] J. Zaumseil and H. Sirringhaus, “Electron and ambipolar transport in organic field-effect transistors.,” *Chem. Rev.*, vol. 107, pp. 1296–323, Apr. 2007.

[114] Z. Chen, V. Stepanenko, V. Dehm, P. Prins, L. D. a. Siebbeles, J. Seibt, P. Marquetand, V. Engel, and F. Würthner, “Photoluminescence and conductivity of self-assembled pi-pi stacks of perylene bisimide dyes.,” *Chemistry*, vol. 13, pp. 436–49, Jan. 2007.

[115] W. Pisula, a. Menon, M. Stepputat, I. Lieberwirth, U. Kolb, a. Tracz, H. Sirringhaus, T. Pakula, and K. Mllen, “A Zone-Casting Technique for Device Fabrication of Field-Effect Transistors Based on Discotic Hexa-peri-hexabenzocoronene,” *Adv. Mat.*, vol. 17, pp. 684–689, Mar. 2005.

[116] T. Fujimoto, Y. Miyoshi, M. M. Matsushita, and K. Awaga, “A complementary organic inverter of porphyrazine thin films: low-voltage operation using ionic liquid gate dielectrics.,” *Chem. Comm. (Cambridge, England)*, vol. 47, pp. 5837–9, May 2011.

[117] H. Klauk, U. Zschieschang, J. Pflaum, and M. Halik, “Ultralow-power organic complementary circuits.,” *Nature*, vol. 445, pp. 745–8, Feb. 2007.

[118] S. Alibert-Fouet, I. Seguy, J.-F. Bobo, P. Destruel, and H. Bock, “Liquid-crystalline and electron-deficient coronene oligocarboxylic esters and imides by twofold benzogenic Diels-Alder reactions on perylenes.,” *Chemistry*, vol. 13, pp. 1746–53, Jan. 2007.

[119] M. Bosdet, W. Piers, T. Sorensen, and M. Parvez, “10a-Aza-10b-borapyrenes: Heterocyclic Analogues of Pyrene with Internalized BN Moieties,” *Angew. Chem.*, vol. 119, pp. 5028–5031, June 2007.

[120] M. Takase, V. Enkelmann, D. Sebastiani, M. Baumgarten, and K. Müllen, “Annularly Fused Hexapyrrolohexaazacoronenes: An Extended πSystem with Multiple Interior Nitrogen Atoms Displays Stable Oxidation States,” *Angew. Chem.*, vol. 119, pp. 5620–5623, July 2007.

[121] F. Würthner and M. Stolte, “Naphthalene and perylene diimides for organic transistors.,” *Chem. Comm.*, vol. 47, pp. 5109–15, May 2011.

[122] R. T. Weitz, K. Amsharov, U. Zschieschang, E. B. Villas, D. K. Goswami, M. Burghard, H. Dosch, M. Jansen, K. Kern, and H. Klauk, “Organic n-channel transistors based on core-cyanated perylene carboxylic diimide derivatives.,” *J. Am. Chem. Soc.*, vol. 130, pp. 4637–45, Apr. 2008.

[123] U. Zschieschang, K. Amsharov, R. T. Weitz, M. Jansen, and H. Klauk, “Low-voltage organic n-channel thin-film transistors based on a core-cyanated perylene tetracarboxylic diimide derivative,” *Synthetic Metals*, vol. 159, pp. 2362–2364, Nov. 2009.

[124] Z. Bao, A. Lovinger, and J. Brown, “New air-stable n-channel organic thin film transistors,” *J. Am. Chem. Soc.*, vol. 7863, no. 23, pp. 207–208, 1998.

[125] B. a. Jones, M. J. Ahrens, M.-H. Yoon, A. Facchetti, T. J. Marks, and M. R. Wasielewski, “High-Mobility Air-Stable n-Type Semiconductors with Processing Versatility: Dicyanoperylene-3,4:9,10-bis(dicarboximides),” *Angew. Chem.*, vol. 116, pp. 6523–6526, Nov. 2004.

[126] H. E. Katz, J. Johnson, A. J. Lovinger, and W. Li, “Naphthalenetetracarboxylic Diimide-Based n-Channel Transistor Semiconductors: Structural Variation and Thiol-Enhanced Gold Contacts,” *J. Am. Chem. Soc.*, vol. 122, pp. 7787–7792, Aug. 2000.

[127] J. H. Oh, S.-L. Suraru, W.-Y. Lee, M. Könemann, H. W. Höffken, C. Röger, R. Schmidt, Y. Chung, W.-C. Chen, F. Würthner, and Z. Bao, “High-Performance Air-Stable n-Type Organic Transistors Based on Core-Chlorinated Naphthalene Tetracarboxylic Diimides,” *Adv. Func. Mat.*, vol. 20, pp. 2148–2156, June 2010.

[128] R. Schmidt, J. H. Oh, Y.-S. Sun, M. Deppisch, A.-M. Krause, K. Radacki, H. Braunschweig, M. Könemann, P. Erk, Z. Bao, and F. Würthner, “High-performance air-stable n-channel organic thin film transistors based on halogenated perylene bisimide semiconductors.,” *J. Am. Chem. Soc.*, vol. 131, pp. 6215–28, May 2009.

[129] M. Gsänger, J. Oh, M. Könemann, H. Höffken, A.-M. Krause, Z. Bao, and F. Würthner, "A Crystal-Engineered Hydrogen-Bonded Octachloroperylene Diimide with a Twisted Core: An n-Channel Organic Semiconductor," *Angew. Chem.*, vol. 122, pp. 752–755, Jan. 2010.

[130] T. Riehm, G. De Paoli, A. E. Konradsson, L. De Cola, H. Wadepohl, and L. H. Gade, "Tetraazaperopyrenes: a new class of multifunctional chromophores.," *Chemistry*, vol. 13, pp. 7317–29, Jan. 2007.

[131] S. C. Martens, U. Zschieschang, H. Wadepohl, H. Klauk, and L. H. Gade, "Tetrachlorinated tetraazaperopyrenes (TAPPs): highly fluorescent dyes and semiconductors for air-stable organic n-channel transistors and complementary circuits.," *Chem. Eur. J.*, vol. 18, pp. 3498–509, Mar. 2012.

[132] J. Björk, M. Matena, M. S. Dyer, M. Enache, J. Lobo-Checa, L. H. Gade, T. a. Jung, M. Stöhr, and M. Persson, "STM fingerprint of molecule-adatom interactions in a self-assembled metal-organic surface coordination network on Cu(111).," *Phys. Chem. Chem. Phys. : PCCP*, vol. 12, pp. 8815–21, Aug. 2010.

[133] A. Soukopp, K. Glöckler, and P. Kraft, "Superstructure formation of large organic adsorbates on a metal surface: A systematic approach using oligothiophenes on Ag (111)," *Phys. Rev. B*, vol. 58, no. 20, pp. 882–894, 1998.

[134] S. Roke, J. Coquel, and A. Kleyn, "The adsorption behaviour of isobutane on Pt (533): A combined RAIRS and TPD study," *Chem. Phys. Lett.*, no. June, pp. 201–208, 2000.

[135] L. Wendling and R. Bergman, "Thermal decomposition of 2H-azirines. Formation of products resulting from carbon-carbon bond cleavage," *J. Org. Chem.*, vol. 2221, no. 1935, 1976.

[136] S. J. Blanksby and G. B. Ellison, "Bond dissociation energies of organic molecules.," *Acc. Chem. Res.*, vol. 36, pp. 255–63, Apr. 2003.

[137] F. Tautz, S. Sloboshanin, J. Schaefer, R. Scholz, V. Shklover, M. Sokolowski, and E. Umbach, "Vibrational properties of ultrathin PTCDA films on Ag(110)," *Phys. Rev. B*, vol. 61, pp. 16933–16947, June 2000.

[138] V. Shklover, F. S. Tautz, R. Scholz, S. Sloboshanin, M. Sokolowski, J. A. Schaefer, and E. Umbach, "Differences in vibronic and electronic excitations of PTCDA on Ag (111) and Ag (110)," *Surf. Sci.*, vol. 456, pp. 60–66, 2000.

[139] V. Shklover, S. Schmitt, and E. Umbach, “Strong K-induced changes in perylene-tetracarboxylic-dianhydride films on Ag (110) studied by HREELS and LEED,” *Surf. Sci.*, vol. 485, pp. 1241–1248, 2001.

[140] K. Tiwari, M. Mishra, and V. P. Singh, “8(E)-4-[{2-(2,4-dinitrophenyl)hydrazono}benzene-1,3-diol] as a solvatochromic Schiff base and chromogenic signaling of water content by its deprotonated form in acetonitrile,” *RSC Advances*, vol. 4, no. 52, p. 27556, 2014.

[141] L. E. Santos-Figueroa, M. E. Moragues, M. M. M. Raposo, R. M. F. Batista, S. P. G. Costa, R. C. M. Ferreira, F. Sancenón, R. Martínez-Máñez, J. V. Ros-Lis, and J. Soto, “Synthesis and evaluation of thiosemicarbazones functionalized with furyl moieties as new chemosensors for anion recognition.,” *Organic and biomolecular chemistry*, vol. 10, pp. 7418–28, Sept. 2012.

[142] C. R. Nicoleti, “Anionic Chromogenic Chemosensors Highly Selective for Fluoride or Cyanide Based on 4-(4-Nitrobenzylideneamine)phenol,” *J. Braz. Chem. Soc.*, vol. 23, no. 8, pp. 1488–1500, 2012.

[143] S. C. Martens, T. Riehm, S. Geib, H. Wadepohl, and L. H. Gade, “Substitutent effects in the periphery of 2,9-bisaryl-tetraazaperopyrene dyes.,” *J. Org. Chem.*, vol. 76, pp. 609–17, Jan. 2011.

[144] Y. Shirota and H. Kageyama, “Charge carrier transporting molecular materials and their applications in devices.,” *Chem. Rev.*, vol. 107, pp. 953–1010, Apr. 2007.

[145] P. Peumans, A. Yakimov, and S. R. Forrest, “Small molecular weight organic thin-film photodetectors and solar cells,” *J. Appl. Phys.*, vol. 93, no. 7, p. 3693, 2003.

[146] D. Fichou, “Structural order in conjugated oligothiophenes and its implications on opto-electronic devices,” *J. Mat. Chem.*, 2000.

[147] X. Yang, L. Wang, C. Wang, W. Long, and Z. Shuai, “Influences of Crystal Structures and Molecular Sizes on the Charge Mobility of Organic Semiconductors: Oligothiophenes,” *Chem. Mat.*, vol. 20, pp. 3205–3211, May 2008.

[148] G. Horowitz, R. Hajlaoui, D. Fichou, and A. El Kassmi, “Gate voltage dependent mobility of oligothiophene field-effect transistors,” *J. Appl. Phys.*, vol. 85, no. 6, p. 3202, 1999.

[149] R. Yamada, H. Kumazawa, T. Noutoshi, S. Tanaka, and H. Tada, "Electrical conductance of oligothiophene molecular wires.," *Nano Letters*, vol. 8, pp. 1237–40, Apr. 2008.

[150] B. Q. Xu, X. L. Li, X. Y. Xiao, H. Sakaguchi, and N. J. Tao, "Electromechanical and conductance switching properties of single oligothiophene molecules.," *Nano Letters*, vol. 5, pp. 1491–5, July 2005.

[151] H. Egelhaaf, D. Oelkrug, and D. Oeter, "HREELS and UV/VIS spectroscopic studies on the electronic structure of oligothiophene thin films," *J. Mol. Struc.*, vol. 348, no. I 995, pp. 7–10, 1995.

[152] G. Koller, S. Berkebile, J. Ivanco, F. Netzer, and M. Ramsey, "Device relevant organic films and interfaces: A surface science approach," *Surf. Sci.*, vol. 601, pp. 5683–5689, Dec. 2007.

[153] T. Okajima, S. Narioka, and S. Tanimura, "NEXAFS spectroscopic studies of molecular orientation in α-sexithienyl evaporated thin films on metal films," *J. Ele. Spec. Rel. Phen.*, vol. 78, no. 100, pp. 379–382, 1996.

[154] A. J. Mäkinen, J. P. Long, N. J. Watkins, and Z. H. Kafafi, "Sexithiophene adlayer growth on vicinal gold surfaces.," *J. Phys. Chem. B*, vol. 109, pp. 5790–5, Mar. 2005.

[155] M. Kiel, K. Duncker, C. Hagendorf, and W. Widdra, "Molecular structure and chiral separation in α-sexithiophene ultrathin films on Au(111): Low-energy electron diffraction and scanning tunneling microscopy," *Phys. Rev. B*, vol. 75, p. 195439, May 2007.

[156] H. Glowatzki, S. Duhm, K.-F. Braun, J. Rabe, and N. Koch, "Molecular chains and carpets of sexithiophenes on Au(111)," *Phys. Rev. B*, vol. 76, p. 125425, Sept. 2007.

[157] S. Prato, L. Floreano, D. Cvetko, V. D. Renzi, A. Morgante, S. Modesti, F. Biscarini, R. Zamboni, and C. Taliani, "Anisotropic Ordered Planar Growth of α-Sexithienyl Thin Films," *J. Phys. Chem. B*, no. 110, pp. 7788–7795, 1999.

[158] K. Duncker, M. Kiel, A. Höfer, and W. Widdra, "Commensurate surface structures and concerted cis-trans-isomerization within ordered monolayers of α-sexithiophene on Ag(001)," *Phys. Rev. B*, vol. 77, p. 155423, Apr. 2008.

[159] G. Yoshikawa, M. Kiguchi, S. Ikeda, and K. Saiki, “Molecular orientations and adsorption structures of α-sexithienyl thin films grown on Ag and Ag surfaces,” *Surf. Sci.*, vol. 559, pp. 77–84, June 2004.

[160] H. Inoue, G. Yoshikawa, and K. Saiki, “Molecular chain structure of α-sexithienyl on Ag (110) observed by scanning tunneling microscopy,” *Ja. J. Appl. Phys.*, 2006.

[161] M. Kiguchi, S. Entani, K. Saiki, and G. Yoshikawa, “One-dimensional ordered structure of α-sexithienyl on Cu(110),” *Appl. Phys. Lett.*, vol. 84, no. 18, p. 3444, 2004.

[162] E. Varene, Y. Pennec, and P. Tegeder, “Assembly and electronic structure of octithiophene on Au(111),” *Chem. Phys. Lett.*, vol. 515, pp. 141–145, Oct. 2011.

[163] T. Kakudate, S. Tsukamoto, M. Nakaya, and T. Nakayama, “Initial stage of adsorption of octithiophene molecules on Cu(111),” *Surf. Sci.*, vol. 605, pp. 1021–1026, June 2011.

[164] S. Nagamatsu, K. Kaneto, R. Azumi, M. Matsumoto, Y. Yoshida, and K. Yase, “Correlation of the number of thiophene units with structural order and carrier mobility in unsubstituted even- and odd-numbered alpha-oligothiophene films.,” *J. Phys. Chem. B*, vol. 109, pp. 9374–8, May 2005.

[165] R. Bourguiga, “Extracting parameters from the current-voltage characteristics of polycrystalline octithiophene thin film field-effect transistors,” *Eur. Phys. J. Appl. Phys.*, vol. 16, pp. 7–16, 2007.

[166] G. Louarn and J. Buisson, “Vibrational Studies of a Series of. alpha.-Oligothiophenes as Model Systems of Polythiophene,” *J. Phys. Chem.*, pp. 11399–11404, 1995.

[167] S. Forrest, “Organicinorganic semiconductor devices and 3, 4, 9, 10 perylenetetracarboxylic dianhydride: an early history of organic electronics,” *J. Phys.: Condens. Matter*, vol. 2599, 2003.

[168] A. Dodabalapur, “Organic light emitting diodes,” *Solid State Commun.*, vol. 102, no. 2, pp. 259–267, 1997.

[169] H. Hoppe and N. S. Sariciftci, “Organic solar cells: An overview,” *J. Mater. Res.*, vol. 19, pp. 1924–1945, Mar. 2011.

[170] P. Fenter, F. Schreiber, L. Zhou, P. Eisenberger, and S. Forrest, “In situ studies of morphology, strain, and growth modes of a molecular organic thin film,” *Phys. Rev. B*, vol. 56, pp. 3046–3053, Aug. 1997.

[171] L. Kilian, E. Umbach, and M. Sokolowski, “A refined structural analysis of the PTCDA monolayer on the reconstructed Au(111) surfaceRigid or distorted carpet?,” *Surf. Sci.*, vol. 600, pp. 2633–2643, July 2006.

[172] P. Fenter, P. Burrows, P. Eisenberger, and S. Forrest, “Layer-by-layer quasi-epitaxial growth of a crystalline organic thin film,” *J. Cryst. Growth*, vol. 152, pp. 65–72, June 1995.

[173] L. Cao, W. Zhang, Y. Han, and T. Chen, “Angular dependent NEXAFS study of the molecular orientation of PTCDA multilayers on Au (111) surface,” *Chinese Sci. Bull.*, vol. 56, pp. 3575–3577, Nov. 2011.

[174] L. Cao, Y. Wang, T. Chen, and W. Zhang, “Charge transfer dynamics of 3, 4, 9, 10-perylene-tetracarboxylic-dianhydride molecules on Au (111) probed by resonant photoemission spectroscopy,” *J. Chem. Phys.*, vol. 135, p. 174701, Nov. 2011.

[175] I. Chizhov, A. Kahn, and G. Scoles, “Initial growth of 3, 4, 9, 10-perylenetetracarboxylic-dianhydride (PTCDA) on Au (111): a scanning tunneling microscopy study,” *J. Cryst. Growth*, vol. 208, pp. 449–458, 2000.

[176] T. Schmitz-Hübsch, T. Fritz, F. Sellam, R. Staub, and K. Leo, “Epitaxial growth of 3, 4, 9, 10-perylene-tetracarboxylic-dianhydride on Au (111): A STM and RHEED study,” *Phys. Rev. B*, vol. 55, no. 12, pp. 7972–7976, 1997.

[177] S. Mannsfeld, M. Toerker, T. Schmitz-Hübsch, F. Sellam, T. Fritz, and K. Leo, “Combined LEED and STM study of PTCDA growth on reconstructed Au(111) and Au(100) single crystals,” *Org. Electron.*, vol. 2, pp. 121–134, Dec. 2001.

[178] M. Mura, X. Sun, F. Silly, and H. Jonkman, “Experimental and theoretical analysis of H-bonded supramolecular assemblies of PTCDA molecules,” *Phys. Rev. B*, vol. 81, p. 195412, May 2010.

[179] A. Gerlach, S. Sellner, F. Schreiber, N. Koch, and J. Zegenhagen, “Substrate-dependent bonding distances of PTCDA: A comparative x-ray standing-wave study on Cu(111) and Ag(111),” *Phys. Rev. B*, vol. 75, p. 045401, Jan. 2007.

[180] S. Henze, O. Bauer, T.-L. Lee, M. Sokolowski, and F. Tautz, “Vertical bonding distances of PTCDA on Au(111) and Ag(111): Relation to the bonding type,” *Surf. Sci.*, vol. 601, pp. 1566–1573, Mar. 2007.

[181] A. Hauschild, K. Karki, B. Cowie, M. Rohlfing, F. Tautz, and M. Sokolowski, “Molecular Distortions and Chemical Bonding of a Large π-Conjugated Molecule on a Metal Surface,” *Phys. Rev. Lett.*, vol. 94, p. 036106, Jan. 2005.

[182] A. A. Levin, T. Leisegang, R. Forker, M. Koch, D. C. Meyer, and T. Fritz, “Preparation and crystallographic characterization of crystalline modifications of 3,4:9,10-perylenetetracarboxylic dianhydride at room temperature,” *Cryst. Res. Technol.*, vol. 45, pp. 439–448, Apr. 2010.

[183] Y. Zou, L. Kilian, A. Schöll, T. Schmidt, R. Fink, and E. Umbach, “Chemical bonding of PTCDA on Ag surfaces and the formation of interface states,” *Surf. Sci.*, vol. 600, pp. 1240–1251, Mar. 2006.

[184] T. Wagner, H. Karacuban, A. Bannani, C. Bobisch, and R. Möller, “Thermal desorption of PTCDA on Cu(111),” *J. Phys.: Conf. Ser.*, vol. 100, p. 052068, Mar. 2008.

[185] N. Al-Sarraf, J. Stuckless, and D. King, “Direct measurement of potassium-promoted change in heat of adsorption of CO on Ni {100},” *Nature*, 1992.

[186] H. Ihm, H. M. Ajo, J. M. Gottfried, P. Bera, and C. T. Campbell, “Calorimetric Measurement of the Heat of Adsorption of Benzene on Pt(111) ,” *J. Phys. Chem. B*, vol. 108, pp. 14627–14633, Sept. 2004.

[187] T. Ertl, *Alkalimetall-Dotierung von Perylentetracarbonsäuredianhydrid (PTCDA) Charakterisierung mit oberflächenanalytischen, elektrischen und quantentheorethischen Methoden.* PhD thesis, Universität Tübingen, 2001.

[188] E. Tsiper, Z. Soos, W. Gao, and A. Kahn, “Electronic polarization at surfaces and thin films of organic molecular crystals: PTCDA,” *Chem. Phys. Lett.*, vol. 360, no. July, pp. 47–52, 2002.

[189] J. Hobley, T. Nakamori, S. Kajimoto, M. Kasuya, K. Hatanaka, H. Fukumura, and S. Nishio, “Formation of 3,4,9,10-perylenetetracarboxylicdianhydride nanoparticles with perylene and polyyne byproducts by 355 nm nanosecond pulsed laser ablation of microcrystal suspensions,” *J. Photochem. Photobio. A: Chem.*, vol. 189, pp. 105–113, June 2007.

[190] N. U. Zhanpeisov, S. Nishio, and H. Fukumura, "Density functional theory study of vibrational properties of the 3,4,9,10-perylene tetracarboxylic dianhydride (PTCDA) molecule: IR, Raman, and UV-vis spectra," *Int. J. Quant. Chem.*, vol. 105, no. 4, pp. 368–375, 2005.

[191] I. Hill, A. Kahn, Z. Soos, and R. P. Jr, "Charge-separation energy in films of π-conjugated organic molecules," *Chem. Phys. Lett.*, no. September, pp. 181–188, 2000.

[192] D. King, "Thermal desorption from metal surfaces: A review," *Surf. Sci.*, vol. 47, pp. 384–402, 1975.

[193] K. Akers and R. Aroca, "Molecular organization in perylenetetracarboxylic dianhydride films," *J. Phys. Chem.*, no. 6, pp. 2954–2959, 1987.

[194] A. Kobitski, R. Scholz, and D. Zahn, "Theoretical studies of the vibrational properties of the 3, 4, 9, 10,-perylene tetracarboxylic dianhydride (PTCDA) molecule," *J. Mol. Struct.*, vol. 625, pp. 39–46, 2003.

[195] A. D. Jong and J. Niemantsverdriet, "Thermal desorption analysis: Comparative test of ten commonly applied procedures," *Surf. Sci.*, vol. 233, pp. 355–365, 1990.

[196] C. Wagner, N. Fournier, F. S. Tautz, and R. Temirov, "Measurement of the Binding Energies of the Organic-Metal Perylene-Teracarboxylic-Dianhydride/Au(111) Bonds by Molecular Manipulation Using an Atomic Force Microscope," *Phys. Rev. Lett.*, vol. 109, p. 076102, Aug. 2012.

[197] J. Ziroff, P. Gold, A. Bendounan, F. Forster, and F. Reinert, "Adsorption energy and geometry of physisorbed organic molecules on Au (111) probed by surface-state photoemission," *Surf. Sci.*, vol. 603, pp. 354–358, Jan. 2009.

[198] M. Mura, A. Gulans, T. Thonhauser, and L. Kantorovich, "Role of van der Waals interaction in forming molecule-metal junctions: flat organic molecules on the Au(111) surface.," *Phys. Chem. Chem. Phys*, vol. 12, pp. 4759–67, May 2010.

[199] V. G. Ruiz, W. Liu, E. Zojer, M. Scheffler, and A. Tkatchenko, "Density-Functional Theory with Screened van der Waals Interactions for the Modeling of Hybrid Inorganic-Organic Systems," *Phys. Rev. Lett.*, vol. 108, p. 146103, Apr. 2012.

[200] V. Bulović, P. Burrows, and S. Forrest, “Study of localized and extended excitons in 3, 4, 9, 10-perylenetetracarboxylic dianhydride (PTCDA) I. Spectroscopic properties of thin films and solutions,” *Chem. Phys.*, vol. 210, pp. 1–12, 1996.

[201] M. Friedrich and G. Gavrila, “Optical properties and molecular orientation in organic thin films,” *J. Phys.: Condens. Matter*, vol. 2699, 2003.

[202] T. Dienel, C. Loppacher, S. Mannsfeld, R. Forker, and T. Fritz, “Growth-Mode-Induced Narrowing of Optical Spectra of an Organic Adlayer,” *Adv. Mat.*, vol. 20, pp. 959–963, Mar. 2008.

[203] E. Engel, K. Schmidt, D. Beljonne, J.-L. Brédas, J. Assa, H. Fröb, K. Leo, and M. Hoffmann, “Transient absorption spectroscopy and quantum-chemical studies of matrix-isolated perylene derivatives,” *Phys. Rev. B*, vol. 73, p. 245216, June 2006.

[204] E. Merino and M. Ribagorda, “Control over molecular motion using the cistrans photoisomerization of the azo group,” *Beil. J. Org. Chem.*, 2012.

[205] T. Asano, T. Yano, and T. Okada, “Mechanistic study of thermal ZE isomerization of azobenzenes by high-pressure kinetics,” *J. Am. Chem. Soc.*, no. 11, pp. 4900–4904, 1982.

[206] C.-W. Chang, Y.-C. Lu, T.-T. Wang, and E. W.-G. Diau, “Photoisomerization dynamics of azobenzene in solution with S1 excitation: a femtosecond fluorescence anisotropy study.,” *J. Am. Chem. Soc.*, vol. 126, pp. 10109–18, Aug. 2004.

[207] D. Gegiou, K. Muszkat, and E. Fischer, “Temperature dependence of photoisomerization. VI. Viscosity effect,” *J. Am. Chem. Soc.*, vol. 245, no. 5, pp. 12–18, 1968.

[208] S. Malkin and E. Fischer, “TEMPERATURE DEPENDENCE OF PHOTOISOMERIZATION. PART II. 1 QUANTUM YIELDS OF cis and trans ISOMERIZATIONS IN AZO-COMPOUNDS,” *J. Phys. Chem.*, vol. 3441, no. 7, 1962.

[209] N. Nishimura and T. Tanaka, “A volumetric study on the thermal cis-to-trans isomerization of 4-(dimethylamino)-4-nitroazobenzene and 4, 4-bis (dialkylamino) azobenzenes: evidence of an inversion mechanism,” *J. Chem. Soc. Perkin Trans. II*, 1986.

[210] B. Marcandalli, “Solvent and substituent effects on thermal cistrans-isomerization of some 4-diethylaminoazobenzenes,” *J. Chem. Soc. Perkin Trans. II*, 1984.

[211] D. Shin and D. Whitten, “Solvent-induced mechanism change in charge-transfer molecules. Inversion versus rotation paths for the Z. fwdarw. E isomerization of donor-acceptor substituted,” *J. Am. Chem. Soc.*, no. 13, pp. 5206–5208, 1988.

[212] E. Brown and G. Granneman, “Cis-trans isomerism in the pyridyl analogs of azobenzene. Kinetic and molecular orbital analysis,” *J. Am. Chem. Soc.*, vol. 49, no. 48, 1975.

[213] M. Comstock, N. Levy, A. Kirakosian, J. Cho, F. Lauterwasser, J. Harvey, D. Strubbe, J. Fréchet, D. Trauner, S. Louie, and M. Crommie, “Reversible Photomechanical Switching of Individual Engineered Molecules at a Metallic Surface,” *Phys. Rev. Lett.*, vol. 99, p. 038301, July 2007.

[214] P. Tegeder, “Optically and thermally induced molecular switching processes at metal surfaces,” *J. Phys.: Con. Matt.*, vol. 24, p. 394001, Oct. 2012.

[215] J. Dokić, M. Gothe, J. Wirth, M. V. Peters, J. Schwarz, S. Hecht, and P. Saalfrank, “Quantum chemical investigation of thermal cis-to-trans isomerization of azobenzene derivatives: substituent effects, solvent effects, and comparison to experimental data.,” *J. Phys. Chem.. A*, vol. 113, pp. 6763–73, June 2009.

[216] C. L. R. D. J. I. P. N. Henningsen, R. Rurali and K. J. Franke, “Site-dependent coordination bonding in self-assembled metal organic networks,” *J. Phys. Chem. Lett.*, vol. 2, pp. 55–61, Jan. 2010.

[217] M. Piantek, J. Miguel, and A. Kruger, “Temperature, surface, and coverage-induced conformational changes of azobenzene derivatives on Cu (001),” *J. Phys. Chem. C*, no. 001, pp. 20307–20315, 2009.

[218] C. Gahl, R. Schmidt, and D. Brete, “Structure and excitonic coupling in self-assembled monolayers of azobenzene-functionalized alkanethiols,” *J. Am. Chem. Soc.*, vol. 132, pp. 1831–8, Feb. 2010.

[219] S. Wagner, F. Leyssner, C. Kördel, S. Zarwell, R. Schmidt, M. Weinelt, K. Rü ck Braun, M. Wolf, and P. Tegeder, “Reversible photoisomerization of an azobenzene-functionalized self-assembled monolayer probed by sum-frequency generation vibrational spectroscopy,” *Phys. Chem. Chem. Phys.*, vol. 11, pp. 6242–8, Aug. 2009.

[220] C. de Villeneuve, F. Michalik, J. N. Chazalviel, K. Rck-Braun, and P. Allongue, “Quantitative IR Readout of Fulgimide Monolayer Switching on Si (111) Surfaces,” *Adv. Mat.*, vol. 25, pp. 416–21, Jan. 2013.

[221] G. Pace, V. Ferri, and C. Grave, "Cooperative light-induced molecular movements of highly ordered azobenzene self-assembled monolayers," *PNAS*, vol. 104, pp. 9937–42, June 2007.

[222] A. Safiei, J. Henzl, and K. Morgenstern, "Isomerization of an azobenzene derivative on a thin insulating layer by inelastically tunneling electrons," *Phys. Rev. Lett.*, vol. 104, p. 216102, May 2010.

[223] J. Henzl, P. Puschnig, and C. Ambrosch-Draxl, "Photoisomerization for a molecular switch in contact with a surface," *Phys. Rev. B*, vol. 85, p. 035410, Jan. 2012.

[224] F. Mohn, J. Repp, L. Gross, and G. Meyer, "Reversible bond formation in a gold-atomorganic-molecule complex as a molecular switch," *Phys. Rev. Lett.*, vol. 105, p. 266102, Dec. 2010.

[225] S. Kubler, R.; Luttke, W.; Weckherlin, "Infrared spectroscopic investigations on isotopic nitrogen compounds. I. The localization of the stretching vibration of the N:N double bond," *Z. Elek.chem. Angew. Phys. Chem.*, vol. 64, p. 650, 1960.

[226] J. Kellerer, B.; Hacker, H. H.; Brandmueller, "Structure of azobenzene and tolane in solution. Raman spectra of azobenzene, azobenzene-d10, p,p'-azobenzene-d2, azobenzene-15N2, and tolane," *I. J. Pure Appl. Phys.*, vol. 9, pp. 903–909, 1971.

[227] N. Biswas and S. Umapathy, "Density functional calculations of structures, vibrational frequencies, and normal modes of trans-and cis-azobenzene," *J. Phys. Chem. A*, vol. 5639, no. 97, pp. 5555–5566, 1997.

[228] J. Green and D. Harrison, "Vibrational spectra of benzene derivativesXVII. Benzonitrile and substituted benzonitriles," *Chim. Acta Part A: Mol. Spec.*, vol. 32, 1976.

[229] F. Frank and J. V. der Merwe, "One-dimensional dislocations. II. Misfitting monolayers and oriented overgrowth," *Proc. Roy. Soc. Lon.. Ser. A, Math. Phys. Sci.*, 1949.

[230] F. Frank and J. V. der Merwe, "One-dimensional dislocations. III. Influence of the second harmonic term in the potential representation, on the properties of the model," *Proc. Roy. Soc. Lon.. Ser. A, Math. Phys. Sci.*, 1949.

[231] F. C. F. van der Merwe and J. H., "Dislocations. I. Static Theory," *Proc. Roy. Soc. Lon.. Ser. A, Math. Phys. Sci.*, 1949.

[232] C. Bronner and P. Tegeder, “Photo-induced and thermal reactions in thin films of an azobenzene derivative on Bi (111),” *New J. Phys.*, vol. 16, p. 053004, May 2014.

[233] A. Airinei, N. Fifere, M. Homocianu, C. Gaina, V. Gaina, and B. C. Simionescu, “Optical properties of some new azo photoisomerizable bismaleimide derivatives.,” *Int. J. Mol. Sci.*, vol. 12, pp. 6176–93, Jan. 2011.

[234] A. Airinei, E. Rusu, and V. Barboiu, “Responsive Behavior of 4-(N-maleimido)azobenzene in Polymers with Aromatic Main Chain and Side Chain Linked Units,” *J. Braz. Chem. Soc.*, vol. 21, no. 3, pp. 489–495, 2010.

[235] J. Garcia-Amorós, M. Martínez, H. Finkelmann, and D. Velasco, “Photoactuation and thermal isomerisation mechanism of cyanoazobenzene-based liquid crystal elastomers.,” *Phys. Chem. Chem. Phys. : PCCP*, vol. 16, pp. 8448–54, May 2014.

[236] J. García-Amorós and D. Velasco, “Recent advances towards azobenzene-based light-driven real-time information-transmitting materials.,” *Beil. J. Org. Chem.*, vol. 8, pp. 1003–17, Jan. 2012.

[237] M. R. Han and M. Hara, “Chain length-dependent photoinduced formation of azobenzene aggregates,” *New J. Chem.*, vol. 30, no. 2, p. 223, 2006.

[238] I. Lednev, T. Ye, P. Matousek, and M. Towrie, “Femtosecond time-resolved UV-visible absorption spectroscopy of trans-azobenzene: dependence on excitation wavelength,” *Chem. Phys. Lett.*, no. June, pp. 68–74, 1998.

[239] A. S. Matharu, S. Jeeva, and P. S. Ramanujam, “Liquid crystals for holographic optical data storage.,” *Chem. Soc. Rev.*, vol. 36, pp. 1868–80, Dec. 2007.

[240] T. Nägele, R. Hoche, W. Zinth, and J. Wachtveitl, “Femtosecond photoisomerization of cis-azobenzene,” *Chem. Phys. Lett.*, vol. 2614, no. July, 1997.

[241] V. Balzani, A. Credi, and M. Venturi, “Molecular machines working on surfaces and at interfaces.,” *Chemphyschem*, vol. 9, pp. 202–20, Mar. 2008.

[242] W. R. Browne and B. L. Feringa, “Making molecular machines work.,” *Nature Nano.*, vol. 1, pp. 25–35, Oct. 2006.

[243] T. Kudernac, N. Katsonis, W. R. Browne, and B. L. Feringa, “Nano-electronic switches: Light-induced switching of the conductance of molecular systems,” *J. Mat. Chem.*, vol. 19, no. 39, p. 7168, 2009.

[244] S. Jan van der Molen and P. Liljeroth, "Charge transport through molecular switches.," *J. Phys.. Cond. Matt. : Inst. Phys. J.*, vol. 22, p. 133001, Apr. 2010.

[245] G. Dutton, D. Quinn, C. Lindstrom, and X.-Y. Zhu, "Exciton dynamics at molecule-metal interfaces: C60Au(111)," *Phys. Rev. B*, vol. 72, p. 045441, July 2005.

[246] P. S. Kirchmann, P. Loukakos, U. Bovensiepen, and M. Wolf, "Ultrafast electron dynamics studied with time-resolved two-photon photoemission: intra- and interband scattering in C 6 F 6 /Cu(111)," *N. J. Phys.*, vol. 7, pp. 113–113, Apr. 2005.

[247] H. Petek, H. Nagano, M. J. Weida, and S. Ogawa, "Surface Femtochemistry: Frustrated Desorption of Alkali Atoms from Noble Metals," *J. Phys. Chem. B*, vol. 105, pp. 6767–6779, July 2001.

[248] C. Gahl, K. Ishioka, Q. Zhong, a. Hotzel, and M. Wolf, "Structure and dynamics of excited electronic states at the adsorbate/metal interface: C6F6/Cu(111).," *Faraday Disc.*, pp. 191–202, Jan. 2000.

[249] C. Bronner, G. Schulze, K. J. Franke, J. I. Pascual, and P. Tegeder, "Switching ability of nitro-spiropyran on Au(111): electronic structure changes as a sensitive probe during a ring-opening reaction.," *J. Phys.. Cond. Matt. : Inst. Phys. J.*, vol. 23, p. 484005, Dec. 2011.

[250] D. Dulić, S. van der Molen, T. Kudernac, H. Jonkman, J. de Jong, T. Bowden, J. van Esch, B. Feringa, and B. van Wees, "One-Way Optoelectronic Switching of Photochromic Molecules on Gold," *Phys. Rev. Lett.*, vol. 91, p. 207402, Nov. 2003.

[251] G. Cottone, R. Noto, and G. La Manna, "Theoretical study of spiropyranmerocyanine thermal isomerization," *Chem. Phys. Lett.*, vol. 388, pp. 218–222, Apr. 2004.

[252] P. Uznanski, "From spontaneously formed aggregates to J-aggregates of photochromic spiropyran," *Synth. M.*, vol. 109, pp. 281–285, Mar. 2000.

[253] M. R. e. a. López, "ATR-FTIR Spectroscopy and their Applications in the Ring-Opening Reaction of Spiropyran Polymers," *Am. Ins. Phys.*, 2012.

[254] Y. Futami, M. L. S. Chin, S. Kudoh, M. Takayanagi, and M. Nakata, "Conformations of nitro-substituted spiropyran and merocyanine studied by low-temperature matrix-isolation infrared spectroscopy and density-functional-theory calculation," *Chem. Phys. Lett.*, vol. 370, pp. 460–468, Mar. 2003.

[255] M. Inouye, "Spiropyran Derivatives as Multifunctional Artificial Receptors for Biologically Important Species," *Mol. Crys. Liqu. Crys. Sci. Tech.. Sec. A. Mol.r Crys.d Liq. Crys.*, vol. 246, pp. 169–172, May 1994.

[256] O. Pieroni and A. Fissi, "New trends in photobiology: Synthetic photochromic polypeptides: possible models for photoregulation in biology," *J. Photochem. Photobio. B: Bio.*, vol. 12, pp. 125–140, 1992.

[257] G. Berkovic, V. Krongauz, and V. Weiss, "Spiropyrans and Spirooxazines for Memories and Switches.," *Chem. Rev.*, vol. 100, pp. 1741–1754, May 2000.

[258] M.-A. Suzuki, T. Hashida, J. Hibino, and Y. Kishimoto, "Multiple Optical Memory using Photochromic Spiropyran Aggregates," *Mol. Crys. Liqu. Crys. Sci. Tech.. Sec. A. Mol.r Crys.d Liq. Crys.*, vol. 246, pp. 389–396, May 1994.

[259] S. Tans, A. Verschueren, and C. Dekker, "Room-temperature transistor based on a single carbon nanotube," *Nature*, vol. 672, no. 1989, pp. 669–672, 1998.

[260] D. Parthenopoulos and P. Rentzepis, "Three-dimensional optical storage memory," *Science*, pp. 843–845, 1989.

[261] T. Niazov, B. Shlyahovsky, and I. Willner, "Photoswitchable electrocatalysis and catalyzed chemiluminescence using photoisomerizable monolayer-functionalized surfaces and pt nanoparticles.," *J. Am. Chem. Soc.*, vol. 129, pp. 6374–5, May 2007.

[262] M. Riskin and I. Willner, "Coupled electrochemical/photochemical patterning and erasure of Ag(0) nanoclusters on Au surfaces.," *Langmuir : ACS J. Surf. Coll.*, vol. 25, pp. 13900–5, Dec. 2009.

[263] M. Karcher, C. Rudt, C. Elsaß er, and P. Fumagalli, "Switching of nonfunctionalized spiropyran thin films on single crystalline MgO(100)," *J. Appl. Phys.*, vol. 102, no. 8, p. 084904, 2007.

[264] G. Schulze, K. J. Franke, and J. I. Pascual, "Induction of a Photostationary Ring-OpeningRing-Closing State of Spiropyran Monolayers on the Semimetallic Bi(110) Surface," *Phys. Rev. Lett.*, vol. 109, p. 026102, July 2012.

[265] P. Hofmann, "The surfaces of bismuth: Structural and electronic properties," *Progr. Surf. Sci.*, vol. 81, pp. 191–245, Jan. 2006.

[266] R. Delgado-Macuil, M. Rojas-López, V. Gayou, a. Orduña Díaz, and J. Díaz-Reyes, "ATR spectroscopy applied to photochromic polymer analysis," *Mat. Charac.*, vol. 58, pp. 771–775, Aug. 2007.

[267] G. Cottone, R. Noto, G. L. Manna, and S. Fornili, "Ab initio study on the photoisomers of a nitro-substituted spiropyran," *Chem. Phys. Lett.*, no. March, pp. 51–59, 2000.

[268] G. A. C. Schiele, "Zur struktur der photochromen form des spiro-6-nitro-[2H-1-benzopyran-2,2-1,3,3-trimethylindolins]," *Tetra. Lett.*, no. 13, pp. 1191–1195, 1967.

[269] J. D. Laposa, "Vibrational spectra of nitrobenzene-d5," *Spectrchim. Acta*, vol. 35 A, no. August 1977, 1979.

[270] J. Clarkson and W. Ewen Smith, "A DFT analysis of the vibrational spectra of nitrobenzene," *J. Mol.r Struc.*, vol. 655, pp. 413–422, Aug. 2003.

[271] A. Navarro, J. González, and A. Fernández, "Structural and vibrational study of isochroman," *Chem. Phys.*, vol. 313, pp. 279–291, June 2005.

[272] R. Klajn, "Spiropyran-based dynamic materials.," *Chem. Soc. Rev.*, vol. 43, pp. 148–84, Jan. 2014.

List of Publications

Publications within this thesis

Aligning the Band Gap of Graphene Nanoribbons by Monomer Doping Christopher Bronner, Stephan Stremlau, Marie Gille, Felix Braue, Anton Haase, Stefan Hecht, and Petra Tegeder *Angew. Chem. Int. Ed.*, **52** (2013) 4422-4425. DOI:10.1002/anie.201209735 *Angew. Chem.*, **125** (2013) 4518-4521. DOI: 10.1002/ange.201209735

Coverage-dependent adsorption geometry of octithiophene on Au(111) Erwan Varene, Lea Bogner, Stephan Meyer, Yan Pennec, and Petra Tegeder *Phys. Chem. Chem. Phys.*, **14** (2012) 691-696. DOI: 10.1039/C1CP22875G

Other Publications

Electronic structure of a sub-nanometer wide bottom-up fabricated graphene nanoribbon: end states, band gap and dispersion C. Bronner, F. Leyssner, S. Stremlau, M. Utecht, P. Saalfrank, T. Klamroth, P. Tegeder *Phys. Rev. B*, **86** (2012) 085444. DOI:10.1103/PhysRevB.86.085444

Imine derivatives on Au(111): Evidence for inverted thermal isomerization Johannes Mielke, Felix Leyssner, Matthias Koch, Stephan Meyer, Ying Luo, Sofia Selvanathan, Rainer Haag, Petra Tegeder, and Leonhard Grill *ACS Nano*, **5** (2011) 2090-2097. doi/abs/10.1021/nn103297e

Acknowledgement

At first I would like to thank my supervisor Prof. Dr. Petra Tegeder for her continuous support and fruitful discussions over the past years. I also want to thank Prof. Katharina J. Franke for being the second referee of my thesis and for her interest in my work.

For the very interesting discussions and the helpful atmosphere in our labs i would of course like to thank all of my co-workers which became friends over the years, first in Berlin then in Heidelberg; Lea Bogner, Christopher Bronner, Alexander Broska, David Gerbert, Marc Hänsel, Felix Leyssner, Friedrich Maaß, Michael Meyer, Laurenz Rettig, Michael Schulze and Erwan Varene.

Especially, I would like to thank Friedrich Maaß who I enjoyed working with during his master thesis and who became the next experienced user of the HREEL setup.

Thank you Felix for introducing me to the demanding but also very great experimental setup and for all your help.

To all the groups and their group-members who our group collaborated with during my work. You have always been very supportive which i am very grateful for: Prof. Katharina Franke, Prof. Lutz Gade, Prof. Stefan Hecht, Prof. Wolfgang Kuch, Prof. Karsten Reuter, Prof. Karola Rück-Braun, Prof. Saalfrank and Prof. Martin Weinelt.

Finally i have to say thank you to my entire family, which supported me throughout the years and during the different routes i took so far. I especially want to thank my wife Marisa and our son Lennart for standing by my side through all we experienced in the last years and for making my life complete.

Curriculum vitae

The curriculum vitae is omitted in this version for reasons of data privacy.